

https://dspace.org/

Effect of miRNA-7 on the tumorigenesis of EGFR-overexpressing CD133+ and CD133- non-small cell lung cancer cells

Kruger, Natasia J

2016
http://hdl.handle.net/10539/22269

Downloaded from a DSpace repository. https://dspace.org/



Effect of miRNA-7 on the tumorigenesis of EGFR-overexpressing $CD133^{+}$ and $CD133^{-}$ non-small cell lung cancer cells

Natasia J. Kruger

A thesis submitted by the Faculty of Health Sciences, University of the Witwatersrand, in fulfilment of the requirements for the degree of Master of Science

Johannesburg, 2016

Declaration

I, Natasia Kruger, declare that this dissertation is my own work. It is being submitted for the degree of Master of Science at the University of the Witwatersrand, Johannesburg. It has not been submitted before for any degree or examination at this or any other University.

Natasia J. Kruger

Signed this _____ day of _____ 20 _____

Abstract

Currently, non-small cell lung cancer (NSCLC) accounts for 80% of lung cancer diagnoses. Even with chemotherapy treatment options, the five year survival rate of patients with NSCLC is only 15%. Cancer stem cells (CSC) are a subpopulation of tumour cells that have the capacity to self-renew and are thought to be responsible for the chemoresistance seen in cancers such as NSCLC. Also associated with chemoresistance is the epidermal growth factor receptor (EGFR), that is overexpressed in some 39% of NSCLC adenocarcinomas. In this study, the role of EGFR in an *in vitro* model of NSCLC cancer stem cell chemoresistance is evaluated. A549 NSCLC cells were separated into CSCs and non-CSCs, based on differential expression of the cell surface marker CD133; CSCs being designated as $CD133^{+}$ and non-CSCs as $CD133^{-}$. The CD133 surface expression was verified in the putative CSC population by immunofluorescence microscopy. The stem cell properties of the CD133 positive cell population were affirmed by their ability to form 3D spheroids in cell culture, relative to the adherent monolayers of the negative cell population. Moreover, some 99% of the $CD133^{+}$ cells, as shown by FACS analysis, possessed the ability to efflux Hoechst 33342 via the ATP-binding cassette (ABCG2) transporters, this being a distinctive feature of stem cells. Using cell scratch assays, the migration rate of the CSCs was determined to be 1.92 fold lower as compared to non-CSCs. Furthermore, CSCs were significantly more chemoresistant than non-CSCs to a 48 hour 20nM treatment of Paclitaxel (IC_{50}), a conventional chemotherapeutic agent, with viabilities of 71.3% and 47.0%, respectively ($P<0.05$). With regard to EGFR expression, EGFR mRNA levels were approximately 16 fold higher in CSCs, compared with non-CSCs, when normalised against 4 reference genes ($P< 0.01$). Analysis of protein expression by confocal microscopy similarly showed elevated EGFR expression, of approximately 1.7-fold relative to non-CSCs ($P<0.0001$), with a

4-fold increased mean expression of CD133 in the CSCs (P<0.0001). To further investigate the role of EGFR in CSCs and non-CSCs, knockdown studies were performed, targeting miRNA-7, a known down-regulator of EGFR expression. Stable lentiviral transduction of U1-pri-miR-7-1 in pHIV-7-GFP was validated in non-CSCs with flow cytometry, which indicated a 97.9% transduction efficiency. Western blotting revealed no visible knockdown in non-CSCs; and this may relate to a point mutation found near the 3' end of the pri-miR-7 sequence, as demonstrated by sequencing analysis. Confocal microscopy of the miR-7 transduced non-CSCs showed a differential localisation of EGFR in the nucleus, not present in the miR-107 control. It is plausible here that the miR-7 mutant causes nuclear localisation of EGFR in the absence of a knockdown effect. This finding may be of relevance, since nuclear EGFR is associated with a poorer prognosis in many tumour types and has been shown to be responsible for resistance to tyrosine kinase inhibitor therapies. In summary, the raised expression of EGFR together with CD133, compared to the non-CSCs may be consistent with the maintenance of this NSCLC stem cell population, mediating chemoresistance through increased ABCG2 cell surface expression. Moreover, the identification of regulatory mechanisms in such chemoresistant lung CSCs may ultimately help to develop novel, effective therapies to alleviate tumour burden.

Keywords: Non-small cell lung cancer, CD133, EGFR, Cancer Stem Cells, A549, chemoresistance, Paclitaxel, microRNA-7

Dedication

To my mother, Kim Heller,

Thank you for showing me what it means to be a good human being.

Through your actions, I have seen that strength and kindness can co-exist and be a powerful force in changing the lives of those less fortunate.

Acknowledgements

I acknowledge my supervisor, Dr Clement Penny, for his assistance, patience and guidance throughout this research process, Dr Marco Weinberg for his input on cloning techniques and Therese Dix-Peek for her invaluable advice and constant encouragement.

The financial assistance of the National Research Foundation (NRF) towards this research is hereby acknowledged. Opinions expressed and conclusions arrived at, are those of the author and are not necessarily to be attributed to the NRF. Further acknowledgement goes to the Canon Collins Trust and The University of the Witwatersrand who also provided financially towards this degree.

Over the past few years, my colleagues have become my friends. Thanks goes to Ezio Fok, Thandiwe Msibi and Kiashanee Moodley who helped me further my research output through their friendship, care and motivation. Thandiwe passed away tragically on 23 February 2016. She was an incredible person, scientist and friend. Thandiwe will be missed by so many. Her passion for scientific research was never-ending and will be carried forward through the many she influenced.

Thanks, too, goes to my parents, grandparents and friends for their encouragement for the duration of my Masters. A special thanks goes to my partner, Bradley Marques, for his unwavering support since I began this journey.

Contents

List of Abbreviations **xviii**

1 Background and rationale **1**

1.1 Introduction 1

1.2 Personalised treatment of NSCLC subtypes 2

1.3 The role of EGFR in non-small cell lung cancer 5

1.4 NSCLC stem cell population 5

1.5 miRNA-7 as a novel therapeutic for NSCLC 6

1.6 Aim 7

1.7 Objectives 7

2 A549 CD133$^+$ CSC isolation and characterisation **8**

2.1 Introduction 8

2.2 Materials and Methods 10

2.2.1 Human cell lines 10

2.2.2 Culture conditions 10

2.2.3 Stem cell separation 11

2.2.4 Growth pattern of NSCLC CD133$^+$ and CD133$^-$ cells 11

2.2.5 CD133 expression of CD133$^+$ and CD133$^-$ A549 cells by confocal microscopy 12

2.2.6 Confirmation of CD133 $^+$ stem cell properties with flow cytometry . . 13

2.3 Results 15

2.3.1 CD133 expression of CD133$^+$ and CD133$^-$ A549 cells detected by immunofluorescence . . . 16
2.3.2 Growth pattern of NSCLC CD133$^+$ and CD133$^-$ cells . . . 17
2.3.3 Flow cytometry evaluation of CD133$^+$ and CD133$^-$ cells' efflux pump properties . . . 18
2.4 Discussion . . . 20
2.4.1 CD133 expression of CD133$^+$ and CD133$^-$ A549 cells by confocal microscopy . . . 20
2.4.2 Morphological confirmation of cell separation . . . 21
2.4.3 CD133$^+$ and CD133$^-$ cells efflux pump properties by flow cytometry . 21
2.4.4 CD133 as a stem cell marker . . . 21
2.5 Conclusion . . . 23

3 Migration and chemoresistance of CSCs 24
3.1 Introduction . . . 24
3.1.1 Chemoresistance of CSCs . . . 24
3.2 Materials and Methods . . . 28
3.2.1 Scratch assay . . . 28
3.2.2 Chemosensitivity assay . . . 28
3.3 Results . . . 30
3.3.1 Scratch assay results . . . 31
3.3.2 Chemosensitivity assay results . . . 33
3.4 Discussion . . . 34
3.5 Conclusion . . . 37

4 EGFR expression in CSCs compared to non-CSCs 38
4.1 Introduction . . . 38
4.1.1 EGFR . . . 38
4.1.2 Role of EGFR in CSCs . . . 40
4.2 Materials and Methods . . . 44
4.2.1 qRT-PCR EGFR mRNA expression in A549 CSC and non-CSCs . . . 44
4.2.2 qRT-PCR equations used to calculate NRQs . . . 45
4.2.3 Confocal microscopy assessment of EGFR expression in CSC *vs* non-CSCs 46
4.3 Results . . . 48

4.3.1 qRT-PCR EGFR mRNA expression in A549 CSCs and non-CSCs. . . 49
4.3.2 Confocal microscopy assessment of EGFR expression in CSCs *vs* non-CSCs 50
4.4 Discussion . . . 51
4.4.1 Role of EGFR in maintenance of CSC state . . . 51
4.4.2 Role of EGFR in chemoresistance of CSCs . . . 52
4.4.3 EGFR as a potential therapeutic target . . . 53
4.5 Conclusion . . . 54

5 EGFR knockdown mediated by miR-7 transduction 55
5.1 Introduction . . . 55
5.1.1 microRNA biology . . . 55
5.1.2 microRNA-7 in regulation of EGFR expression . . . 56
5.1.3 Stable transduction of miR-7 in A549 non-CSCs . . . 57
5.2 Materials and Methods . . . 60
5.2.1 PCR amplification of hsa-pri-miR-7 from A549 genomic DNA . . . 60
5.2.2 Construction of pU1-neo plasmid with hsa-pri-miR-7 insert . . . 62
5.2.3 Construction of pHIV-7-GFP plasmid containing U1-hsa-pri-miR-7 and U1-pri-miR107 . . . 63
5.2.4 Verification of successful pHIV-7-GFP-U1-hsa-pri-miR-7 clone . . . 66
5.2.5 Lentivirus synthesis . . . 66
5.2.6 NSCLC lentivirus transduction . . . 66
5.2.7 Quantification of transduction efficiency using flow cytometry . . . 67
5.2.8 Growth kinetics comparison between A549 WT and A549 miR-107 transduced control . . . 67
5.2.9 Western blotting . . . 68
5.2.10 Confocal microscopy based comparison of EGFR fluorescence in miR-7 and miR-107 transduced cells . . . 70
5.3 Results . . . 71
5.3.1 Verification of pHIV-7-GFP plasmid containing U1-hsa-pri-miR-7 insert 73
5.3.2 Transduction efficiency of A549 non-CSCs . . . 75
5.3.3 Growth kinetics of A549 WT *vs* A549 miR-107 control . . . 77
5.3.4 Western blot Analysis . . . 79
5.3.5 Sequencing analysis . . . 80

5.3.6 IF based comparison of EGFR fluorescence in miR-7 and miR-107 transduced cells . . . 81
5.4 Discussion . . . 82
5.4.1 Verification of pHIV-7-GFP plasmid containing U1-hsa-pri-miR-7 insert 82
5.4.2 Transduction efficiency . . . 82
5.4.3 Growth kinetics . . . 82
5.4.4 Knockdown efficiency . . . 83
5.4.5 Differential localisation of EGFR in miR-7 transduced cells . . . 87
5.5 Conclusion . . . 89

6 Final conclusion and future work **90**
6.1 Future work . . . 92

References **94**

A Solutions **105**
A.1 Cell culture . . . 105
A.1.1 Phosphate buffered saline . . . 105
A.1.2 CD133 $^{-}$ CCM . . . 105
A.1.3 CD133^{+} Stempro CCM . . . 105
A.2 CD133^{+} cell isolation and characterisation . . . 105
A.2.1 0.5% BSA PBS . . . 105
A.2.2 HBSS+ . . . 106
A.3 Lentivirus synthesis and NSCLC transduction . . . 106
A.3.1 Transformation buffer . . . 106
A.3.2 1000× Ampicillin stock . . . 106
A.3.3 Ampicillin agar broth . . . 106
A.3.4 0.5M EDTA pH 8.0 . . . 107
A.3.5 TAE buffer . . . 107
A.3.6 1% TAE agarose gel . . . 107
A.4 miR-7 EGFR knockdown efficiency . . . 107
A.4.1 3% formaldehyde PBS solution . . . 107
A.4.2 RIPA buffer . . . 108
A.4.3 20% Ammonium persulfate (AP) . . . 108

A.4.4 40% Acrylamide/Bis . . . 108
A.4.5 8% Resolving gel . . . 108
A.4.6 8× Resolving buffer . . . 109
A.4.7 Stacking gel . . . 109
A.4.8 4× Stacking buffer . . . 109
A.4.9 1× Tank buffer . . . 109
A.4.10 1× Transfer buffer . . . 109
A.4.11 Blocking buffer . . . 110
A.4.12 Wash buffer . . . 110

B Protocols **111**

B.1 Lentivirus synthesis and NSCLC transduction . . . 111
B.1.1 Competent bacteria . . . 111
B.1.2 Ampicillin agar bacterial plates . . . 112
B.1.3 Ligation . . . 112

C Supplementary data **113**

C.1 Lentivirus synthesis and NSCLC transduction . . . 113
C.1.1 Molecular cloning . . . 113
C.1.2 Sequencing results . . . 116
C.1.3 hsa-pri-miR-7 sequence and the U1 promoter . . . 116

List of Figures

1.1 Molecular targets for personalised treatment of NSCLC, adapted from Kerr et al., (2014). EGFR, ALK and HER2 amongst others act as oncogenes, increasing downstream activation of key signalling pathways, incuding the RAS-RAF-MEK and PI3K-Akt-mTOR pathways. As depicted here, these promote cell growth, enhance invasion and metastasis and stimulate angiogenesis 2

1.2 Percentage 5 year survival (dotted line) of patients with Stage I to IV NSCLC. Adapted from Rami-Porta et al., (2014) 4

2.1 **(A)** Immunofluorescence images depicting the expression of CD133 (green) on the surface of A549 cells. $CD133^-$ (middle panel) and $CD133^+$ (right panel) separated using magnetic cell separation. The primary anti-CD133 antibody and secondary anti-mouse Alexa Fluor 488 antibody were at 1:500 and 1:100 dilutions respectively, N, nucleus. **(B)** Bar graph of the average green fluorescence per pixel for triplicate samples of both $CD133^-$ and $CD133^+$ fractions; P=0.0001. Data are presented as the mean±SD ($^*P$<0.001). . . . 16

2.2 Growth pattern of A549 $CD133^-$ **(A)** and $CD133^+$ **(B)** cells obtained through CD133 selective magnetic cell separation (100× magnification). $CD133^-$ cells grow as an adherent monolayer (A) while $CD133^+$ cells grow in suspension as 3-dimensional spheroids (B) 17

2.3 Dot plot of Forward Scatter Area (FSC-A) *versus* Side Scatter Area (SSC-A) for Hoechst 33342 unstained (left) and stained (right) A549 cells, separated into $CD133^-$ (top) and $CD133^+$ (bottom) populations through magnetic cell separation, with P1 showing the singlet cell population selected for subsequent Flow Cytometry experiments 18

2.4 Dot plot of Forward Scatter Height (FSC-H) *versus* Hoechst-Blue fluorescence intensity for unstained (left) and stained (right) A549 cells separated into $CD133^-$ (top) and $CD133^+$ (bottom) populations through magnetic cell separation, with P2 showing the Hoechst positive cell population 19

3.1 Comparison of migration (in μm) of CSC and non-CSC at 4 time intervals (2 hours, 4 hours, 26 hours and 28 hours), following a scratch in 80% confluent cells with a sterilised P200 pipette tip; P= 0.05, 0.33, 0.0005 and 0.0004, respectively. Data are presented as the mean±SD, $^*P<0.05$ 31

3.2 Comparison of migration (μm) and relative migration rates of non-CSC WT and CSC WT. **(A)** Photomicrographs of non-CSC WT and CSC at time 0 and at 24 hours (100x magnification). **(B)** Relative migration rate of non-CSC WT and CSC. As is evident, the relative migration rate of non-CSCs exceeds that of the CSCs by almost 2-fold 32

3.3 Percentage viability of CSC and non-CSC after a 48 hour treatment with 20 nM Paclitaxel. There is a significant difference in cell viability between non-CSCs and CSCs at 20 nM Paclitaxel (P=0.0006). Data are presented as the mean±SD ($^*P<0.01$) 33

4.1 Outline of EGFR pathway. Adapted from Nyati *et al.* (2006) 40

4.2 qRT-PCR normalised relative Cq (NRQ) of EGFR mRNA expression in A549 CSCs and A549 non-CSCs showing the increased NRQ in CSCs (16.68) compared with the non-CSCs (1.00); P=0.0084 ($^*P < 0.01$) 49

4.3 Comparison of EGFR expression in CSCs and non-CSCs through confocal microscopy and ImageJ analysis. **(A)** Immunofluorescence images captured with Zen 2012 Software viewed on a Zeiss LSM 780 confocal microscope depicting the expression of CD133 (green), EGFR (red) A549 CSCs (top panel) and non-CSCs (bottom panel) and the nuclei stained with DAPI (blue). The primary anti-CD133 antibody and secondary anti-mouse Alexa Fluor 488 antibody were at 1:500 and 1:100 dilutions, respectively. The primary Rb anti-EGFR antibody (ab2430) and secondary anti-rabbit Alexa Fluor 594 antibody were utilised at 1:500 and 1:200 dilutions, respectively. Co-localisation is shown as yellow, being a merge of the green and red fluorescence **(B)** Bar graphs of A549 CSCs and non-CSCs showing average red fluorescence per pixel indicating EGFR expression; P=1.04 $\times 10^{-}5$ (left); and green fluorescence per pixel indicating CD133 expression P=4.78$\times 10^{-8}$ (right). Data represent measurements from biological triplicates and are presented as the mean ±SD ($^{*}P$<0.0001). 50

5.1 Stem loop structure of hsa-pri-miR-7, with miR-7 sequence detailed in red. Image adapted from Landgraf et al., (2003) 57

5.2 Diagram of the strategy used to obtain hsa-pri-miR-7 downstream of the U1 promoter in pU1-neo. Forward and reverse primers were designed to contain BsmBI recognition sites. These allowed for digestion of the pri-miR-7 sequence and subsequent ligation downstream of the U1 promoter in the pU1-neo plasmid. More details in Section 5.2 61

5.3 Summary of cloning strategy employed to create A549 CSC and non-CSC with constitutive expression of miR-7 and miR-107 using lentiviral transduction techniques. miR-7 was amplified through PCR with BsmB1 sites both upstream and downstream of the pri-miR-7 sequence. pri-miR-7 sequence was then cleaved at the BsmBI sites and ligated into the pU1-neo plasmid following which the U1-pri-miR-7 construct was cleaved with NotI and XbaI and ligated into pHIV-7. HEK293T cells were transduced with pMDG2, psPAX and pHIV-7-GFP. The lentiviral products were collected and used to transduce A549 non-CSCs. 65

5.4 Gel electrophoresis to confirm successful cloning of U1-hsa-pri-miR-7 into pHIV backbone. Lanes A, B and C representing each of clones A, B and C, respectively, were digested with BamHI. In clones A and B, this generated an 8500 bp fragment (pHIV-7) and a 420 bp fragment (the pri-miR-7 insert). Previous round cloning of hsa-pri-miR-7 in the pU1-neo backbone (4500 bp) digested with NotI served as the control (Ctrl). 74

5.5 Gel electrophoresis to confirm successful cloning of U1-miR-107 into pHIV backbone. Lanes A and B representing each of clones A and B respectively, were digested with BamHI. In clones A and B, this generated an 8500 bp fragment (pHIV-7) and a 440 bp fragment (the pri-miR-107 insert). Previous round cloning of hsa-pri-miR-107 in the pU1 backbone digested with NotI served as the control (Ctrl). 74

5.6 Dot plot of Forward Scatter Height (FSC-H) *versus* SSC-A (left) and GFP fluorescence (right) for A549 non-CSC WT, miR-7 and miR-107. 100 000 events were measured and gating was done to exclude doublets and GFP autofluorescence. 75

5.7 Dot plot of event count *versus* GFP fluorescence (left) and the corresponding BF images (middle) and GFP images at 100x magnification (right) for the WT (top) miR-7 (middle) and miR-107 (bottom) A549 non-CSCs. 100 000 events were measured and gating was done to exclude doublets and GFP autofluorescence. 76

5.8 Proliferation (µm) of A549 non-CSC WT and non-CSC miR-107 control at 2 hours, 4 hours, 26 hours and 28 hours after scoring with a sterilised P200 pipette tip; P= 0.69, 0.43, 0.02 and 0.035, respectively. Images were captured using the Olympus IX71 inverted microscope with 40x magnification. Data are presented as the mean ±SD (*P<0.05). 77

5.9 Comparison of growth rates of non-CSC WT and non-CSC transduced with miR-107. **(A)** Photomicrographs of non-CSC WT and non-CSC miR-107 at the time of the score with a P200 pipette (0 hour) and 24 hours afterwards (100 × magnification). **(B)** Relative growth rate of non-CSC WT and non-CSC miR-107 transduced cells. The non-CSC WT cells proliferated approximately 1.7 fold more than the non-CSC miR-107 cells. 78

5.10 Western blotting results showing EGFR expression of non-CSCs WT, non-CSC miR-7 and non-CSC miR-107 transduced cells, with BA as a loading control. **(A)** Membrane exposed for 1.194 seconds in the Biorad Geldoc™after an overnight transfer and a 1:1000 primary EGFR (top) and 1:1000 primary BA antibody (bottom) incubated for 1 hour, respectively. Secondary antibody staining was performed with the Invitrogen WesternDot® 625 Western Blot Kit **(B)** EGFR intensity relative to BA control for non-CSC WT, non-CSC miR-7 and non-CSC miR-107 transduced control. The relative EGFR expression in non-CSC miR-7 was similar to the non-CSC WT and non-CSC miR-107 population. 79

5.11 Electropherograms representing the sequencing results for pHIV-7-pri-miR-7 illustrating the U1 promoter sequence (green), the pri-miR-7 sequence (blue), as well as the U1' termination sequence (red) (performed by Inqaba Biotechnologies). 80

5.12 Immunofluorescence based comparison of EGFR expression in miR-107 and miR-7 transduced non-CSCs **(A)** Immunofluorescence staining depicting EGFR expression (red) in miR107 transduced non-CSCs (top panel) serving as the negative control for miR-7 transduced non-CSCs (bottom panel). miR-7 and miR-107 transduced cells show GFP fluorescence (green) (100x magnification) **(B)** Comparison of EGFR fluorescence in A549 miR7 and miR107 transduced cells following ImageJ analysis; P=0.00616. The miR-107 cells have a 1.7 fold increase in red fluorescence (EGFR), as compared to the miR-7 cells. Data represent measurements from biological triplicates and are presented as the mean ±SD (*P<0.01). 81

5.13 Comparison of hsa-pri-miR-7 and hsa-pri-miR-7 mutant predicted stem-loop structures using Quikfold. Structures shown include the miRNA sequence (red) and the Dicer (red arrows) and Drosha (blue arrows) cleavage sites. Mutant miR-7 will have additional Dicer cleavage sites indicated by the small red arrows. 86

6.1 Summary of findings of the present study and the relationship of these to previous studies, including selected Hallmarks of Cancer. 91

C.1 Gel electrophoresis to confirm successful PCR amplification of hsa-pri-miR-7 and hsa-pri-miR-107 from the A549 genome. hsa-pri-miR-7 and hsa-pri-miR-107 products with flanking BsmBI restriction sites are 480bp and 500bp, respectively 113

C.2 pHIV-7-GFP vector map 114

C.3 Vector maps of pHIV-7-pri-miR-7 (top) and pHIV-7-pri-miR-107 control (bottom). Vector maps were constructed on SnapGene, based on the pHIV-7 sequence kindly donated by Marc Weinberg. 115

List of Tables

3.1 Calculated rate of migration (μmh^{-}1) of WT CSC and WT non-CSCs using the exponential trendlines obtained in Fig.3.1 31

4.1 qRT-PCR forward (F) and reverse (R) primer sequences for EGFR and reference gene controls. 45

5.1 Calculated rate of proliferation (μm.h^{-}1) of WT CSC and WT non-CSCs using the exponential trendlines obtained in Fig.3.1 77

List of Abbreviations

Akt	Protein kinase B
BA	Beta actin
BCA	bicinchoninic acid assay
Bcl-2	B-cell lymphoma 2
BF	Bright field
bp	Base pairs
CCM	Cell culture medium
Ctrl	Control
CSC	Cancer stem cell
DNA	Deoxyribose nucleic acid
DMSO	Dimethyl sulfoxide
EGFR	Epidermal growth factor receptor
ELISA	Enzyme-linked immunosorbent assay
EMT	Epithelial-mesenchymal transition
ERbB1	Epidermal growth factor receptor
F	Forward
GAPDH	*Homo sapiens* glyceraldehyde-3-phosphate dehydrogenase
GFP	Green fluorescence protein
GOI	Gene of interest
HIF-1	Hypoxia Inducible Factor-1
HER1	Epidermal growth factor receptor
HMBS	*Homo sapiens* hydroxymethylbilane synthase
IAP	Inhibitor of Apoptosis Proteins
IF	Immunofluorescence

MCS	Multiple cloning site
MDR1	Multi-drug resistance gene
miR-7	microRNA-7
miR-107	microRNA-107
NF	Normalisation factor
Non-CSC	Non-cancer stem cell
NRQ	Normalised relative quantity
NSCLC	Non-small cell lung cancer
PAI	Plasminogen activator inhibitor
PCR	Polymerase chain reaction
PEI	Polyethylenimine
PI3K/Akt	Phosphoinositide-3-kinase
R	Reverse
RAS	Rat sarcoma oncogene
RCT	Randomised control trial
ROS	Reactive Oxygen Species
RPM	Revolutions per minute
RPMI	Roswell Park Memorial Institute medium
RQ	Relative quantity
RT	Room temperature
RTK	Receptor tyrosine kinase
SCLC	Small cell lung cancer
SD	Standard deviation
SNPs	Single Nucleotide Polymorphisms
TNM	Tumour node metastasis
UBC	*Homo sapiens* ubiquitin C
Vs	*Versus*
3D	3 dimensional

CHAPTER 1

Background and rationale

1.1 Introduction

Lung cancer has the highest mortality rate of all cancers, with approximately 160,000 deaths reported annually in the United States of America alone (Siegel et al., 2015). Lung cancer, or bronchogenic carcinoma, is defined as a tumour which affects the parenchyma or airways of the lung. These cancers are divided into small cell lung cancer (SCLC) or non-small cell lung cancer (NSCLC), depending on a tissue diagnosis (Kerr et al., 2014) . Histologically, NSCLC are adenocarcinomas or squamous cell carcinomas. SCLC is derived from neuroendocrine cells and has a better response to chemotherapy than NSCLC (Früh et al., 2013; Barash et al., 2012). Currently, NSCLC accounts for 80% of lung cancer diagnoses (Jemal et al., 2009). Even with chemotherapy treatment options, the five year survival rate of patients with NSCLC is only 15% (Miller, 2005). Treatment options are limited for NSCLC, with chemoresistance and radioresistance being common occurrences. New advances based on the molecular basis of NSCLC will aid in improving long term survival of patients with NSCLC.

The treatment for NSCLC is dependent on the tumour node metastasis (TNM) stage. Treatment options include radiation therapy, surgery and chemotherapy, and treatment choice is dependent on the tumour stage and functionality status of the patient (Silvestri et al., 2003; Buccheri et al., 1996). For resectable NSCLC (Stage I or Stage II disease) in a patient with a good performance status, surgical treatment remains the treatment of choice. In patients

with metastatic disease, chemotherapy is the treatment offered. More recently, chemotherapy treatment options have been based on the molecular characteristics of the tumour, where patients with specific driver mutations can be presented with more targeted therapies that improve overall survival (Kerr et al., 2014).

1.2 Personalised treatment of NSCLC subtypes

Previously, all patients with metastatic NSCLC would receive cytotoxic chemotherapy. However, this generalised treatment does not ensure enhanced survival in all patients with the disease (Kerr et al., 2014). These chemotherapeutic agents are toxic to all rapidly dividing cells, resulting in unwanted effects on normal cells, increasing patient morbidity (Langer et al., 2015). NSCLC is known to be the result of a heterogeneous group of mutations and molecular research has now identified subsets of NSCLC which express biomarkers that can guide targeted therapy, outlined in Fig.1.1 (Kerr et al., 2014).

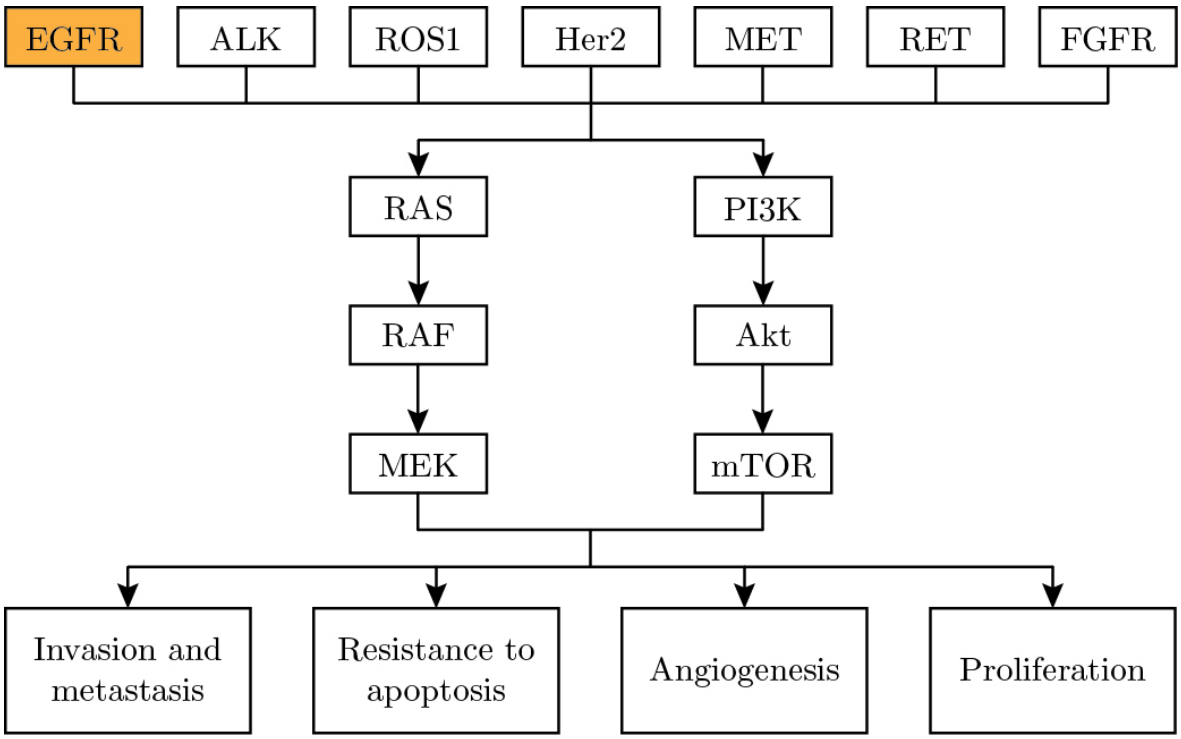


Figure 1.1: Molecular targets for personalised treatment of NSCLC, adapted from Kerr et al., (2014). EGFR, ALK and HER2 amongst others act as oncogenes, increasing downstream activation of key signalling pathways, incuding the RAS-RAF-MEK and PI3K-Akt-mTOR pathways. As depicted here, these promote cell growth, enhance invasion and metastasis and stimulate angiogenesis

During the evolution of normal lung parenchyma to malignant cells, mutations are acquired which confer a survival advantage to the malignant cells. These mutations are known as 'driver mutations' and aid in the transformation of non-malignant to malignant cells (Alamgeer et al., 2013a). Mutations or overexpression of EGFR, ALK, HER2, and other proteins as outlined in Fig.1.1 act as oncogenes. These oncogenes will increase downstream activation of pathways including RAS, RAF, PI3K and Akt. These will then increase NSCLC's ability to proliferate, resist apoptosis while increasing angiogenesis and the invasive ability of the tumour cells.

The two most important proteins mutated or overexpressed in NSCLC are KRAS and EGFR. KRAS is discussed here, with EGFR discussed below. KRAS mutations are reported in approximately 20% of NSCLC cases and are associated with decreased survival (Johnson et al., 2013). KRAS is a membrane-bound GTPase that mediates the expression of mitogen-activated protein kinase (MAPK) as well as increasing the activation of phosphoinisitide 3-kinase (PI3K). Acting through these pathways, apoptosis is decreased, enhancing cellular proliferation and tumour expansion. KRAS mutations confer resistance to chemotherapeutic agents such as erlotinib, a tyrosine kinase inhibitor, often successful in treating EGFR mutation positive NSCLC (O'Byrne et al., 2011).

Targeted therapies essentially function to downregulate the effect of these driver mutations to reverse the survival advantage these cells have over the normal lung parenchyma (Pao and Girard, 2011). This approach to treatment has improved patient prognosis, whilst decreasing toxicity to non-malignant cells wherein these driver mutations are absent. The 5-year survival rate of patients with NSCLC is shown in Fig.1.2 (Rami-Porta et al., 2015). A randomised control trial (RCT) of NSCLC patients with driver mutations showed the median survival for those receiving targeted therapies to be 3.5 years compared with the 2.4 years in patients receiving conventional cytotoxic chemotherapy (Kris et al., 2014).

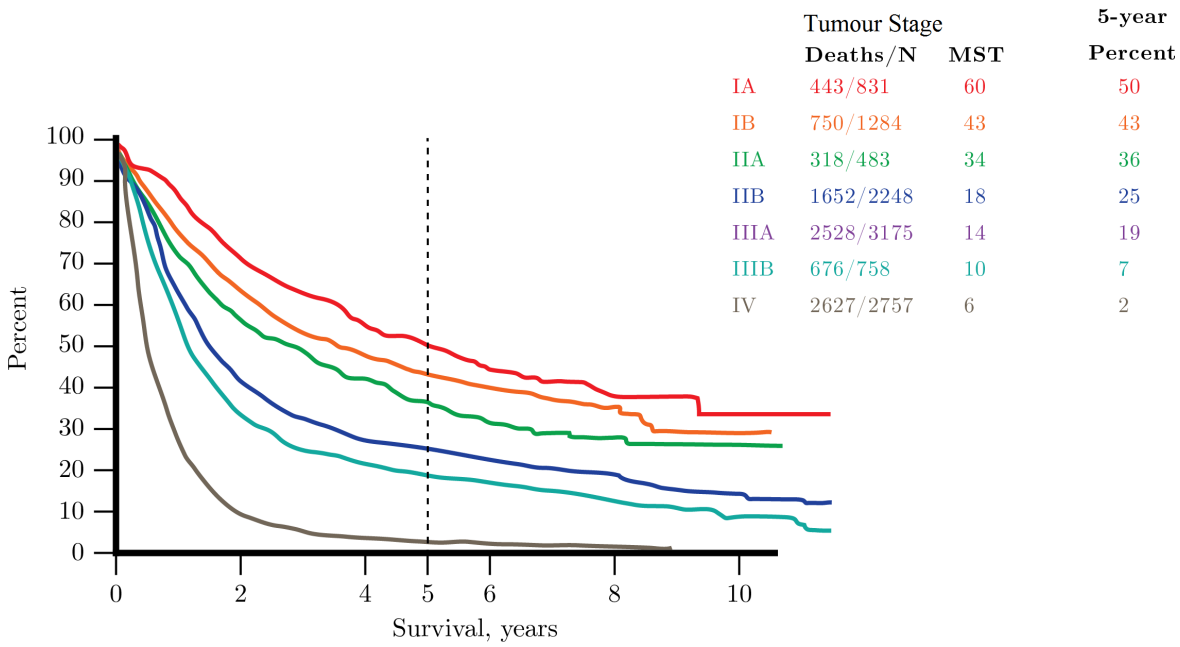


Figure 1.2: Percentage 5 year survival (dotted line) of patients with Stage I to IV NSCLC. Adapted from Rami-Porta et al., (2014)

Unchecked EGFR activity drives NSCLC through increased proliferation, decreased apoptosis and increased chemoresistance (Su et al., 2014). One of the driver mutations for which there is a definitive therapy is an EGFR tyrosine kinase mutation. EGFR driver mutations are present in 15% of diagnosed NSCLC adenocarcinomas and are treated with EGFR tyrosine kinase inhibitors such as erlotinib (Shi et al., 2014). Driver mutations are not the only genetically determined factors that play a role in treatment and prognosis. In some NSCLCs, overexpression of genes relevant to cell proliferation and survival are important. Notably, however, in many cases of NSCLC, EGFR is not mutated but overexpressed, giving the tumour the ability to outgrow normal lung tissue with the higher proliferative rate also increasing the statistical chance for the accumulation of mutations (Gaber et al., 2014). Targeting EGFR overexpressing tumours with novel therapies has been shown to improve patient outcomes significantly (Singh et al., 2012). Even with these targeted therapies for EGFR overexpressing NSCLC, the 5-year survival rate is low (Lee et al., 2011). Since EGFR overexpression is found in KRAS mutation positive NSCLC and up to 80% of NSCLCs (Hirsch et al., 2009), EGFR overexpression in this population will be the particular focus of the present study.

1.3 The role of EGFR in non-small cell lung cancer

EGFR binds extracellular ligands, such as the epidermal growth factor (Oda et al., 2005). Once a ligand is bound, the EGFR transitions into an active homodimer. This, in turn, activates protein-tyrosine kinases within the cell, such as RAS, PI3K and Akt (Downward et al., 1984). This results in a cascade of signals that transduce the extracellular signal into the nucleus activating genes to increase cellular growth, proliferation and differentiation (Nakada et al., 2013). Aberrant expression of EGFR within cells results in an increase in the activation of these pathways causing a higher rate of cellular growth, proliferation, invasion and metastasis, all associated with the progression of cancer (Johnston et al., 2006; Gaber et al., 2014). EGFR overexpression confers resistance to chemotherapy through mechanisms such as decreased Bcl-2 expression, an antiapoptotic protein; and increased expression of efflux pumps, such as MDR1, that prevent the accumulation of cytotoxic drugs within cancer cells (Gaber et al., 2014). Moreover, EGFR overexpression is thought to drive dedifferentiation of cancer cells to form cancer stem cells (CSCs) that display more resistance to chemotherapy than non-CSCs and are thought to be responsible for tumour relapse (Singh et al., 2012).

1.4 NSCLC stem cell population

Within a NSCLC tumour, there exist different cell types (Alamgeer et al., 2013b). A small proportion of cells within the mass are cancer stem cells (CSCs) which share some properties with somatic stem cells (Shimono et al., 2015). CSCs have three main characteristics: their ability to differentiate, proliferate and renew themselves. These characterists are often referred to as their 'stemness' (Alamgeer et al., 2013b). These stem cells are hypothesised to have arisen from somatic cells undergoing dedifferentiation. In order to positively identify a cancer stem cell, xenotransplantation is often utilised, wherein the subsequent induction of a tumour from the transplanted cell indicates that the cell is indeed a cancer stem cell (Wicha et al., 2006). The CSCs possess traits which facilitate tumour survival, such as the ability to increase blood vessel formation via EGFR-induced VEGF expression and cell migration capabilities, through the process of epithelial to mesenchymal transition. These positively identified CSCs express high levels of the cell surface marker CD133/prominin-1, a glycoprotein which specifically localises to membrane protrusions. Currently, its exact function and contribution to the properties of CSCs remains to be determined (Miqueli et al., 2009). CD133 expressing cells, CSC, notably have an increased chemoresistance and radioresistance compared with non-CSCs

(Singh et al., 2012). CSCs exposed to conventional chemotherapy display an increased ability to repair DNA damage and decreased apoptosis when compared with non-CSC. Some pathways thought to contribute to the resistance of these cells to therapy are the Notch, EGFR and sonic hedgehog pathways (Banerji et al., 2015). Moreover, EGFR mediated signalling specifically has been found responsible for dedifferentiation of non-CSCs to CSCs and maintenance of CSCs states (Yang et al., 2013). Further details can be found in Chapter 4. Consequently, the resistance of these CSCs to chemotherapy, coupled with their ability to initiate and maintain tumour formation deems them key targets for new therapeutics (Banerji et al., 2015).

1.5 miRNA-7 as a novel therapeutic for NSCLC

Poor chemotherapy response is evident in NSCLC patients who have an overexpression of EGFR (Singh et al., 2012). The ever increasing knowledge of cancer genomics, understanding of genes and gene regulators involved in cancer development and proliferation, allows for the formulation of novel therapeutics, potentially to target both cancer cells and their stem cell side population (Chin et al., 2011). Cancer genomics has yielded insights into miRNAs, gene regulators implicated in either cancer progression or reduction. These miRNAs are small, single stranded non-coding RNAs, approximately 22 nucleotides in length and are known negative regulators of gene expression (Garzon et al., 2010). These miRNAs mediate post-transcriptional gene silencing, preventing translation of their target genes. The ability for a miRNA to silence a gene is determined by its seed region's complementarity to an mRNA sequence. Since the seed regions are often only six nucleotides in length, the probability of their complementarity to mRNA sequences is relatively high; as a result, miRNAs are shown to bind to and silence not just one gene, but numerous genes (Lai, 2015). Consequently, one miRNA may have the ability to affect gene expression in a number of pathways. Studies indicate that pathways affected include oncogenic and developmental pathways, suggesting that miRNAs could be potential therapeutic agents in targeting cancers, including NSCLC (Feng et al., 2015). In this regard, Barger and Nana-Sinkam (2015) recently reported that inducing high intracellular expression levels of miRNA-7 decreases the synthesis of EGFR and increases the susceptibility of NSCLC to chemotherapy. The role of miR-7 in mediating post-transcriptional silencing of EGFR is discussed further in Chapter 5.

In the present study, the chemosensitivity of NSCLC CSCs to chemotherapy is evaluated and compared to non-CSCs. Since EGFR is also correlated to chemoresistance, the expression of

EGFR in CSCs and non-CSCs is assessed as a potential mechanism for the chemoresistance of CSCs. Moreover, in view of the potential role of miR-7 as a mediator of cellular EGFR expression, transduction of miR-7, first in non-CSCs, was performed to determine the effect it has on both EGFR expression and its intracellular localisation in an *in vitro* cell culture model of NSCLC.

1.6 Aim

The potential role of EGFR in chemoresistance and maintenance of the CSC state in NSCLC is assessed. Moreover, in association with this, the likely regulatory effects of miR-7 on EGFR expression and its intracellular localisation in NSCLC is investigated.

1.7 Objectives

The objectives of this research are:

- to isolate A549 cells into $CD133^+$ (CSCs) and $CD133^-$ (non-CSCs);
- to compare NSCLC CSCs and non-CSCs proliferative ability and sensitivity to Paclitaxel;
- to determine EGFR expression in A549 derived CSCs compared to non-CSCs;
- to stably express hsa-pri-miR-7, initially within non-CSCs;
- and to determine the effect increased pri-miR-7 expression has on the EGFR expression and localisation in non-CSCs.

CHAPTER 2

A549 CD133$^+$ CSC isolation and characterisation

2.1 Introduction

Cancer stem cells (CSCs), a minor subpopulation of cells within a tumour, are thought to be responsible for its initiation and to play a role in increasing its metastatic and invasive ability (Nguyen et al., 2012). CSCs show an increased resistance to conventional cancer therapies, such as chemotherapy, compared with non-CSCs. CSCs show multidrug resistance because of their expression of multidrug transporters such as ABCG2 (Sarkadi et al., 2004; Zhou et al., 2001).

CSCs have different morphological characteristics to non-CSCs. Unique cell surface markers have been identified on CSCs that are absent in non-CSCs. CD133 is one such marker, which is highly expressed on the surface of NSCLC CSCs, but is downregulated as CSCs differentiate to form the non-CSCs (Peichev et al., 2000). While the exact function of CD133 is unknown, according to Qu et al. (2013), expression of CD133 on the surface of tumour cells, such as NSCLC, is associated with a poor prognosis for patients, with lymph node metastasis and a low 5 year patient survival rate.

Although CD133$^+$ cells display stem-like characteristics, the expression of such a marker on its own is insufficient to characterise cells as CSCs. CSCs are also distinguished by their 3D spheroid morphological growth pattern in culture, the presence of excess ATP-pumps allowing

for multiple drug resistance; and are ultimately distinguished as CSCs through their ability to self-renew and establish new tumours when xenotransplanted into nude mice (Singh et al., 2004; Beier et al., 2007; Zhou et al., 2001).

Much is still unknown about the characteristics of CD133$^+$ CSCs in many tumour subtypes, including NSCLC. The A549 cell line, a model for NSCLC adenocarcinoma, can be separated into CSC and non-CSC populations (see below). The chemosensitivity and relative EGFR expression of CD133$^+$ CSC and CD133$^-$ non-CSCs will be addressed in Chapters 3 and 4,respectively.

The objectives of this chapter are:

- to isolate CD133$^+$ and CD133$^-$ cell populations from the general A549 cell population;
- to compare the cell surface expression of CD133 in CD133$^+$ and CD133$^-$ separated A549 populations;
- to establish the stemness of CD133$^+$ A549 cells through their ability to form spheroids;
- and to assess the capacity of CD133$^+$ A549 cells to efflux Hoechst 33342.

2.2 Materials and Methods

2.2.1 Human cell lines

The human A549 non-small cell lung cancer (NSCLC) adenocarcinoma cell line was donated by S. Weiss at the University of the Witwatersrand, originally sourced from the American Type Culture Collection (ATCC). The A549 cell line was first isolated by Giard et al. (1973) from a 58 year old Caucasian male. This cell line has a known overexpression of EGFR and was used here as a model *in vitro* system for NSCLC.

2.2.2 Culture conditions

The A549 cell line was cultured in Thermo Scientific HyClone DME/F 12 1:1 1× medium supplemented with 10% heat inactivated Fetal Bovine Serum (FBS) (Lonza), 10 000 IU Penicillin and Streptomycin (Appendix A.1.2), at 37°C and 5% CO_2 in air. Cells were incubated in 25cm^3 culture flasks (Nest). Once 80% confluency was reached, cells were subcultured by removing media and then washing with 5 ml of sterile phosphate buffered saline (PBS), prepared using Protocol A.1.1. PBS was discarded and cells were then incubated in 1 ml Lonza Trypsin/EDTA at 37°C for 5 minutes. The cells were gently agitated and observed for detachment on a Carl Zeiss Axiovert 25 microscope at 400× magnification. Once cells were detached, Trypsin/EDTA was neutralised with an equal volume of CCM. This cell mixture was transferred to 15 cm^3 Nunc tubes and centrifuged at 800× RPM in the MSE Minor centrifuge for 3 minutes. The resulting pellet was resuspended in 10 ml CCM with 1 ml of the suspension being transferred into each of 10 75 cm^3 cell culture flasks (Falcon). 9 ml CCM was then added to each 75 cm^3 flask to reach a final volume of 10 ml. The 10 flasks were incubated until 80% confluency was achieved to produce an adequate number of cells for cell separation.

Post-separation and for the duration of this research, A549 CD133$^+$ CSCs were grown in stem cell medium in the absence of foetal bovine serum (FBS) (Appendix A.1.2). A549 CD133$^-$ non-CSCs were cultured in CCM, the same medium used for the unseparated A549 cell line. Cells were cultured in 25 cm^3 flasks and subcultured when cells reached a confluency of 80%.

2.2.3 Stem cell separation

After centrifugation of 1×10^8 A549 cells at 800× RPM for 10 minutes, supernatant was removed and cells resuspended in 300 µl PBS (Sigma Aldrich) containing 0.5% BSA (Sigma Aldrich). Next, 300 µl FcR Blocking Reagent (Miltenyi Biotec) followed by 300 µl CD133 MicroBeads (Miltenyi Biotec) were added to the suspension to a final volume of 900 µl; and the cells were then placed at 4°C for 30 minutes. Cells were gently agitated 15 minutes into incubation time. After incubation, cells were washed with a 2 ml 0.5% BSA-PBS solution. Centrifugation of cells at 800× RPM for 10 minutes was performed, followed by aspiration of the supernatant. Cells were resuspended in 1 ml of 0.5% BSA-PBS.

A MACS MS Column (Miltenyi Biotec) was placed into the magnetic MACS stand. The column was rinsed with 500 µl 0.5% BSA-PBS buffer. The cell suspension was applied to the column in 200 µl volumes at spaced intervals to prevent the column from clogging. After this, the column was washed three times with 500 µl 0.5% BSA-PBS. Next, the column was removed from the MACS magnet and was placed over a sterile 15 ml collection tube. 1 ml of 0.5% BSA-PBS was aspirated into the column and the supplied plunger applied, effecting the release of the CD133 positive cell fraction into the collection tube. Purity of the CD133 population was increased by applying the CD133$^+$ collected cells into a new MACS MS column. The flow through from this second column was collected. This CD133$^-$ population served as the non-stem cell NSCLC population, for subsequent experiments. The CD133 enriched population from the second separation was utilized as the NSCLC stem cell population. The stem and non-stem cells were expanded in StemPro medium (ThermoFisher Scientific) and DMEM:F12 10% FBS (Lonza), respectively.

2.2.4 Growth pattern of NSCLC CD133$^+$ and CD133$^-$ cells

A particular characteristic of CSCs is a spontaneous ability to form three dimensional aggregates of cells in culture, termed spheroids. To assess the growth patterns of CD133$^+$ and CD133$^-$ cells, a total of 1×10^6 cells from each culture were seeded into separate sterile 10 cm bacterial cell culture dishes and grown until the CD133$^-$ cells were 80% confluent. Cells were viewed on an Olympus IX71 inverted microscope and field images were taken for each subpopulation at 100× magnification to record their growth patterns. Images were taken using the XLM colour camera and captured using the cellSens Imaging Solutions Software (Olympus).

2.2.5 CD133 expression of CD133$^+$ and CD133$^-$ A549 cells by confocal microscopy

Cell surface expression of CD133 is crucial to confirm successful separation into CD133$^+$ and CD133$^-$ populations. 10 000 A549 CD133$^+$ and CD133$^-$ cells were seeded in triplicate onto separate sterilized glass cover slips housed in 5cm^3 cell culture dishes. The cells were grown in appropriate media for 24 hours at 37°C in a sterilized incubator with 5% CO_2 in air. After 24 hours, the cells were washed twice with 2 ml sterile PBS, pre-warmed to 37°C. The cells were then fixed for 30 minutes in a 3% formaldehyde PBS solution (Appendix A.4.1). After fixation, cells were washed three times with pre-warmed PBS and stored at 4°C in a final volume of 3 ml 0.5% BSA-PBS solution.

Primary anti-CD133 solution was prepared at a concentration of 1 pg ml^{-1} by adding 1 µl of Mouse anti-CD133 (Abcam) to 499 µl 0.5% BSA PBS (Appendix A.2.1) and mixed by inverting. Each coverslip containing cells was removed from the dish and placed in a sterile dry dish of the same size. A total of 200 µl primary antibody solution was added carefully to the coverslip immediately to prevent it from drying. Each dish was carefully sealed with Parafilm (American Can Co.) and placed in a moist sealed container at 4°C for 12 hours.

Three wash steps with 1 ml of a fresh 0.5% BSA-PBS solution were performed prior to secondary antibody staining. The secondary antibody solution (1:100) was prepared by adding 2 µl of anti-mouse Alexa Fluor 488 antibody (Invitrogen) to 198 µl 0.5% BSA-PBS solution. The coverslips were gently and individually blotted dry with tissue paper. Each coverslip was then placed cell-side-up onto a labelled microscope slide, to which the total 200 µl secondary antibody was immediately added. All slides were incubated in a moist sealed container at RT, for 1 hour in the dark.

After secondary antibody incubation, each coverslip was placed in a separate well in a six well plate and each well washed 3 times with 0.5% BSA-PBS solution. After the third wash, each coverslip was removed from its well and placed on the appropriate microscopy slide after dabbing the side of the coverslip on tissue paper. 200 µl DAPI (Sigma Aldrich) solution (1:10000 dilution) was then immediately added to the coverslip and then incubated for 5 minutes in the dark at RT.

After DAPI staining, each coverslip was washed as outlined above for secondary staining. The coverslips were then ready to be mounted onto slides. Each slide was carefully cleaned with dH_2O and the coverslip dabbed onto tissue paper to remove residual 0.5% BSA-PBS solution. A drop of Fluoromount (Sigma Aldrich) was applied to each slide and each coverslip was slowly lowered, to prevent the formation of bubbles, cell-side-down, onto the appropriately labelled slide. The Fluoromount was dried for 4 hours in the dark at RT before slides were viewed on a Zeiss LSM 780 confocal microscope. Images were captured using Zen 2012 software.

Every experiment was performed in triplicate and fluorescence was analysed using ImageJ software. To quantitatively compare the results, the fluorescence intensity was calculated as a factor of green fluorescence per pixel area for each cell in the triplicate sample. Statistical analysis was performed using a Student's t-test.

2.2.6 Confirmation of CD133 $^+$ stem cell properties with flow cytometry

CD133$^+$ and CD133$^-$ A549 cells were grown to 80% confluency in StemPro medium (ThermoFisher Scientific) and CCM respectively. Cells were washed with 2 ml PBS and incubated with Trypsin/EDTA for 3 minutes. Once resuspended, the Trypsin/EDTA was neutralised with an equal volume of CCM. Cells were pelleted by centrifugation for 5 minutes at 800× RPM. The supernatant was decanted and the cell pellet was resuspended in CCM pre-warmed to 37°C. Four tubes of 1x10^6 cells were prepared for both the CD133$^+$ and CD133$^-$ populations. In each of three such suspensions, Hoechst 33342 (Thermo Fisher Scientific) was added to a final concentration of 5 µg µl^{-1}. The cells within each of these 15 ml tubes were transferred to a 50 ml sterile tube and these were placed in a shaking incubator at 37°C for 2 hours at 200× RPM.

After incubation, the vials were centrifuged at 800× RPM for 6 minutes. The supernatant was discarded and cells were resuspended in 50 µl 4°C PBS. The mixture was left to incubate for 30 minutes in the dark at 4°C. After incubation, 450 µl ice cold HBSS+ (Appendix A.2.2) was added to each sample. Unstained controls were prepared in the absence of Hoechst 33342.

Flow cytometry was performed using the LSR Fortessa BD Pharmingen. The unstained A549 cell line was used to plot the forward scatter area (FSC-A) *versus* Forward Scatter Height (FSC-H) graph, from which gating was performed to analyse single viable cells. The LSR Fortessa is set at 450/20 BP filter to determine Hoechst staining, this to obtain data regarding

the purity of the isolated stem and non-stem cell populations. Graphic representation and analysis of results were performed using FACSDiva software, version 6.2.

2.3 Results

A549 cells were separated into CD133$^+$ and CD133$^-$ cells through magnetic cell separation. The success of the separation itself was confirmed by assessing CD133 cell surface expression of the CD133$^+$ and CD133$^-$ fractions, seen in Fig.2.1. The green fluorescence of the CD133$^+$ fraction indicates CD133 cell surface expression and is 14-fold higher than that of the CD133$^-$ fraction. The CD133$^-$ cells had fluorescence levels equal to the negative control. From this, the marked cell surface expression of CD133 in the CD133$^+$ fraction shows successful cell separation.

Although CD133 has been described as a good CSC marker for NSCLC, the characteristics of the CD133$^+$ fractions determines whether the population can be regarded as CSCs. CSC and non-CSC have distinct growth patterns in culture. In this regard, after a period of 3 days of culture, the CD133$^+$ cells developed the spheroid morphology growing as 3D cultures typical of CSCs, while the CD133$^-$ fraction remained as an adherent monolayer of cells (see Fig.2.2).

A particular and accepted characteristic of CSCs is their expression of ABCG2 efflux pumps that prevent the entry of substances into the cells. This principle can be tested through Hoechst staining, which was measured using flow cytometry as represented in Fig2.3 and Fig.2.4.

In Fig.2.3, the gating for singlets using FSC-A *versus* SSC-A was kept consistent for all flow cytometry samples, as indicated by P1. The percentage of total singlet events gated were 67.3% for Hoechst unstained CD133 $^-$ cells, 85.8% for the Hoechst stained CD133 $^-$ cells, 53.6% for the Hoechst unstained CD133 $^+$ fraction and 47.3% for the Hoechst stained CD133 $^+$ cell fraction.

P2 in Fig.2.4 indicates the percentage population positive for Hoechst 33342 staining, compared with the unstained control. For the CD133 $^-$ fraction of cells, 99.8% are positive for Hoechst staining, relative to 0.3% for the unstained control. For the CD133$^+$ cell fraction, only 0.9% of the population were positive for Hoechst staining, compared to 0.4% for the unstained control.

2.3.1 CD133 expression of CD133+ and CD133− A549 cells detected by immunofluorescence

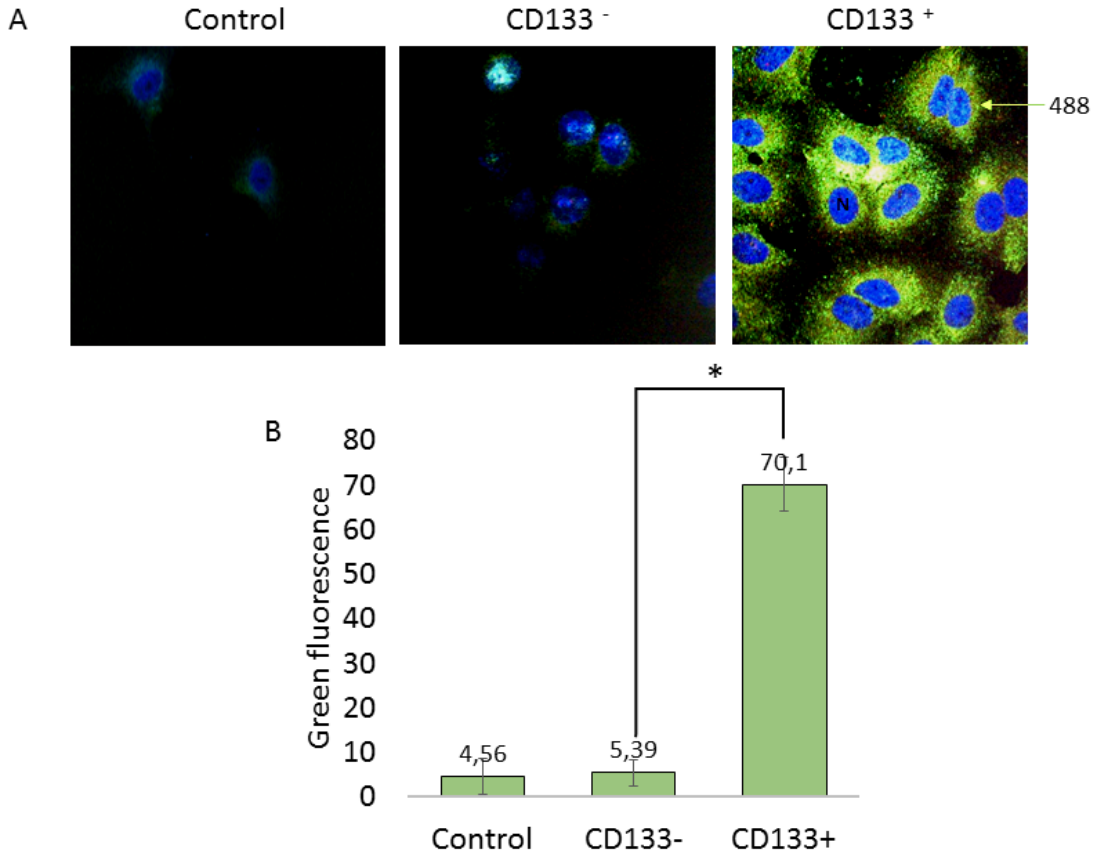


Figure 2.1: **(A)** Immunofluorescence images depicting the expression of CD133 (green) on the surface of A549 cells. CD133− (middle panel) and CD133+ (right panel) separated using magnetic cell separation. The primary anti-CD133 antibody and secondary anti-mouse Alexa Fluor 488 antibody were at 1:500 and 1:100 dilutions respectively, N, nucleus. **(B)** Bar graph of the average green fluorescence per pixel for triplicate samples of both CD133− and CD133+ fractions; P=0.0001. Data are presented as the mean±SD (*P<0.001).

2.3.2 Growth pattern of NSCLC CD133+ and CD133− cells

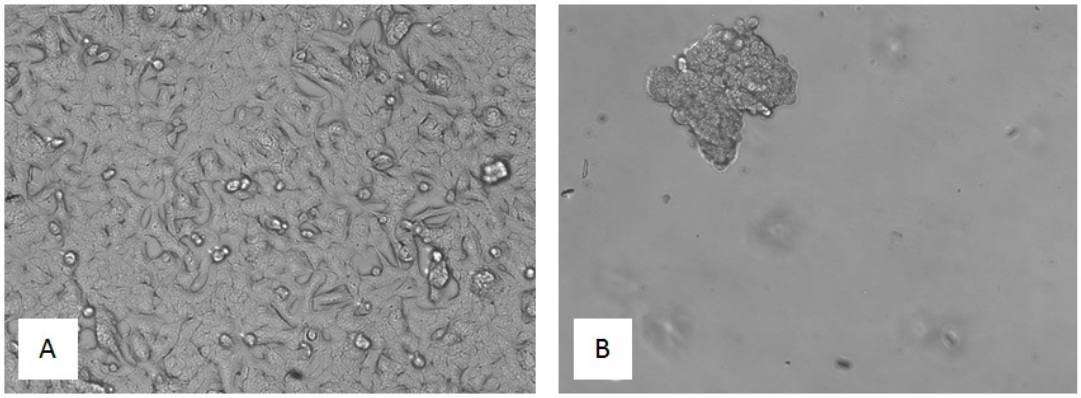


Figure 2.2: Growth pattern of A549 CD133− **(A)** and CD133+ **(B)** cells obtained through CD133 selective magnetic cell separation (100× magnification). CD133− cells grow as an adherent monolayer (A) while CD133+ cells grow in suspension as 3-dimensional spheroids (B)

2.3.3 Flow cytometry evaluation of CD133+ and CD133− cells' efflux pump properties

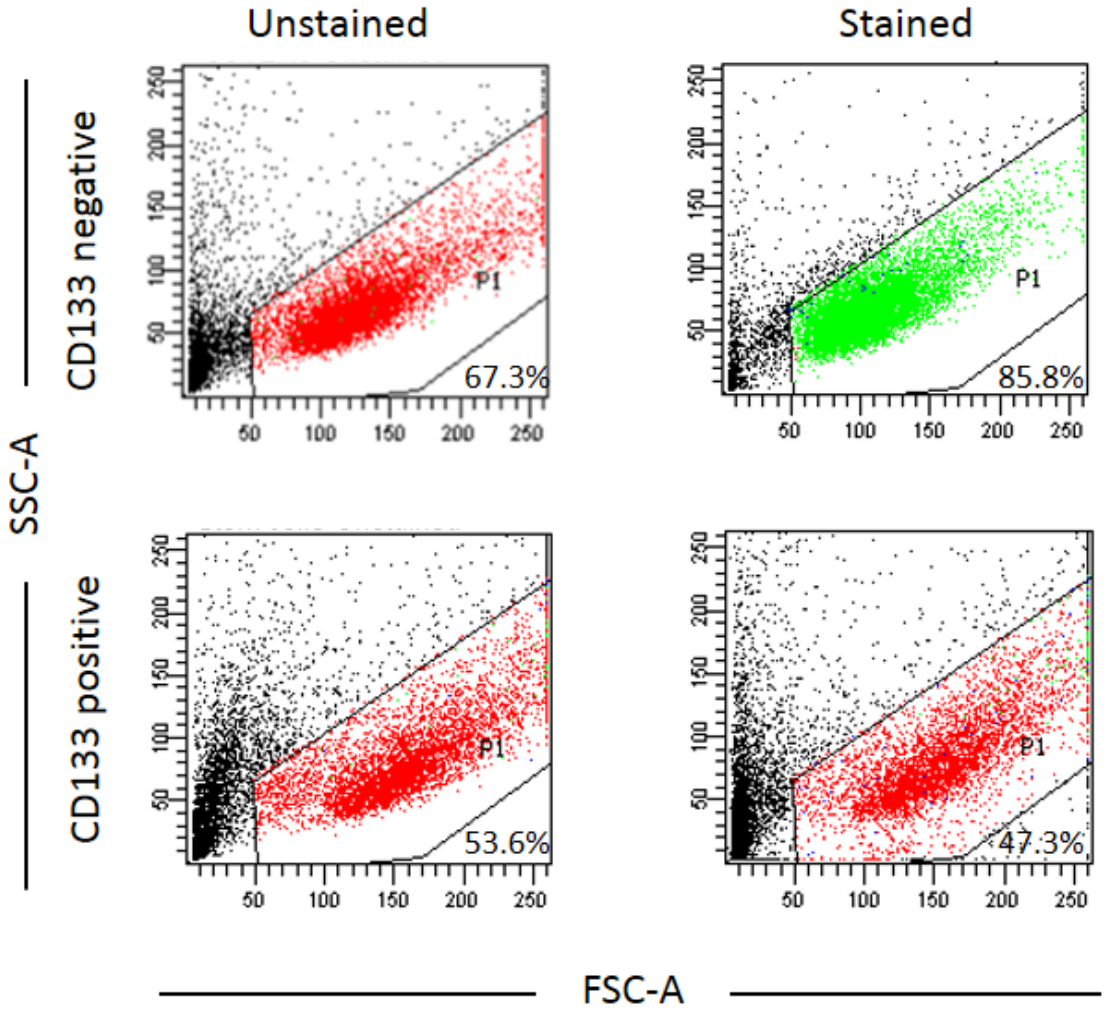


Figure 2.3: Dot plot of Forward Scatter Area (FSC-A) *versus* Side Scatter Area (SSC-A) for Hoechst 33342 unstained (left) and stained (right) A549 cells, separated into CD133− (top) and CD133+ (bottom) populations through magnetic cell separation, with P1 showing the singlet cell population selected for subsequent Flow Cytometry experiments

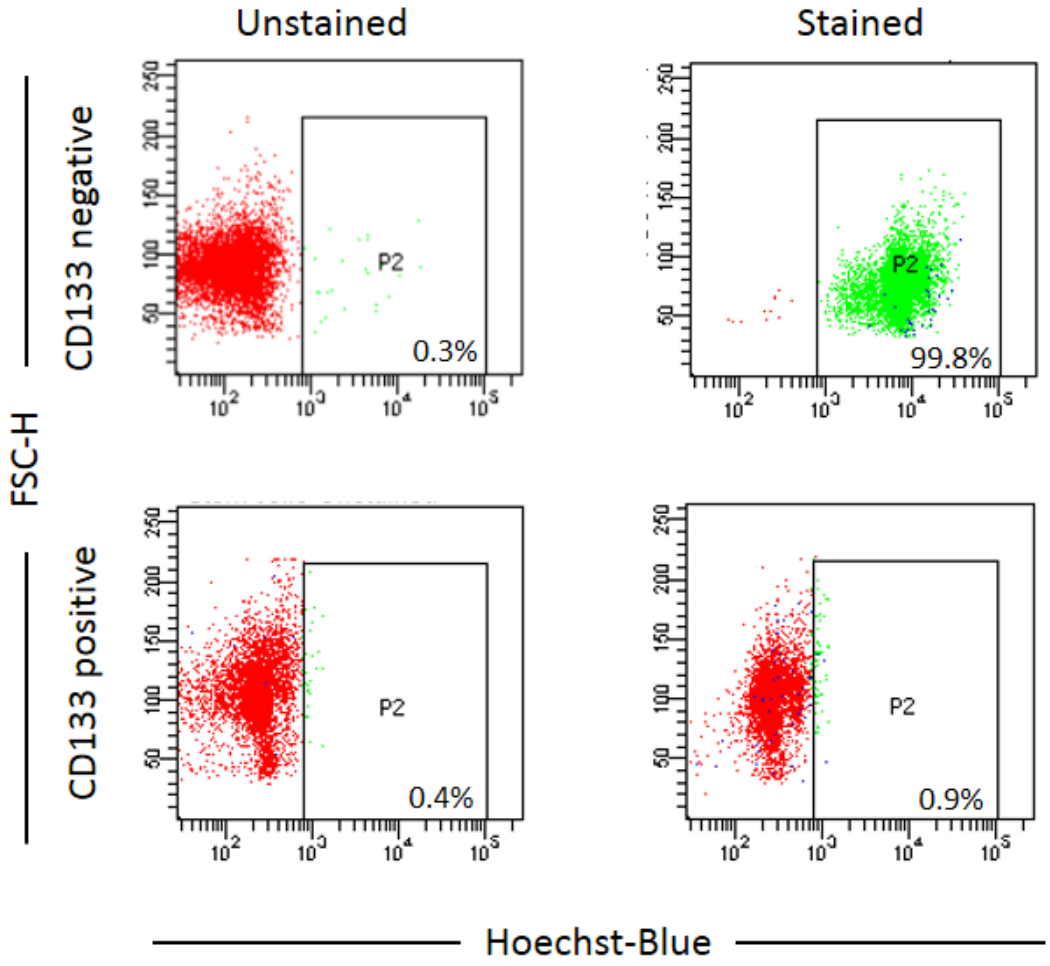


Figure 2.4: Dot plot of Forward Scatter Height (FSC-H) *versus* Hoechst-Blue fluorescence intensity for unstained (left) and stained (right) A549 cells separated into $CD133^-$ (top) and $CD133^+$ (bottom) populations through magnetic cell separation, with P2 showing the Hoechst positive cell population

2.4 Discussion

Cancer stem cells have particular morphological and phenotypic characteristics, including CD133 cell surface expression, a spheroid morphological growth pattern and the expression of the ABCG2 multidrug transporter channel, indicated through the ability of the CSCs to efflux Hoechst dye. To ascertain whether the A549 cell line was successfully separated into CD133$^+$ CSCs and CD133$^-$ non-CSCs, a number of experiments were performed.

Flow cytometry was used to confirm the efficiency of cell separation by determining the percentage of the two cell fractions which had CD133 cell surface expression. Although CD133 is a strong marker for CSCs, further tests were performed to ensure that the CD133$^+$ fraction displayed the morphologic and phenotypic characteristics of stem cells by assessing the growth of the cells in culture and their ability to efflux Hoechst 33342.

2.4.1 CD133 expression of CD133$^+$ and CD133$^-$ A549 cells by confocal microscopy

Miltenyi MicroBeads were used to separate A549 CD133$^+$ and CD133$^-$ cells (Richardson et al., 2004). Validation of this separation was performed by confocal microscopy and flow cytometry.

With confocal microscopy, the observed fluorescence of CD133 was qualitatively higher in the CD133$^+$ than the CD133$^-$ fraction (Fig.2.1A). In order to objectively validate this difference, fluorescence pixel intensity was measured and graphed to compare the density of green pixels per cell image. For the CD133$^+$ fraction, there was a significant difference in fluorescence intensity compared with the negative control (P=0.0001). Furthermore, the green fluorescence observed in the CD133$^+$ fraction is exclusively due to antibody binding to CD133 on the cell surface, since during preparation of cells for confocal microscopy, the cells were not permeabilised (Steinmetz et al., 2011). The lack of CD133 expression seen in the negative population (Fig.2.1B) compared with the control indicates the absence of CSCs in this population. Since the CD133$^+$ cells showed marked fluorescence where the CD133$^-$ showed none compared with the control (P=0.804), it can be confirmed here that the cells were successfully separated based on CD133 cell surface expression.

Together, confocal microscopy and flow cytometry confirmed the separation of the cells into CD133$^+$ and CD133$^-$ populations. Since CD133 is a proven cell surface marker for NSCLC

stem cells, the separation of cells based on this marker from the NSCLC cell line provides for a stem cell-rich population (Salcido et al., 2010).

2.4.2 Morphological confirmation of cell separation

Since the A549 cells were successfully separated into $CD133^+$ and $CD133^-$ fractions, next their stem cell properties required verification. One method of characterising cancer stem cells is based on their morphological pattern of growth (Kim et al., 2012b). Figure 2.2 shows the growth patterns of both the $CD133^+$ and $CD133^-$ cell fractions. The $CD133^+$ fraction displays the spheroid growth pattern typical of CSCs cultured in serum free medium enriched with bFGF and EGF (Yang and Wu, 2008; Kim et al., 2012b). This spheroid pattern observed for the $CD133^+$ fraction is absent in the $CD133^-$ fraction, thus indicating the absence of CSC in this cell population (Beier et al., 2007). From a morphological perspective, as described by Horst et al. (2008), the presence of spheroids in the CD133 $^+$ confirms the CSC nature of these cells.

2.4.3 $CD133^+$ and $CD133^-$ cells efflux pump properties by flow cytometry

Further phenotypic characterisation using Hoechst 33342 was used to validate these $CD133^+$ cells as CSCs. The CSC population is defined as a cell side population that has a low Hoechst staining ability (Goodell et al., 1996). This is due to the phenotypic expression of ABCG2, a multidrug transporter present on the surface of CSCs (Zhou et al., 2001). As depicted in Fig.2.4, only 0.9% of the $CD133^+$ population stained positively for Hoechst 33342, indicating that some 99.1% of the cell population possessed the ABCG2 efflux pump, a key physiological feature that characterises these cells as CSCs (Zhou et al., 2001).

2.4.4 CD133 as a stem cell marker

CD133 cells are shown by Tirino et al. (2009) to display spheroid growth patterns and have the ability to initiate tumour formation. Another paper by Hilbe et al. (2004), reported that $CD133^+$ cells may play a role in tumour neovascularisation. Additional evidence by Salnikov et al. (2010) noted the chemoresistance potential of these cells, due to their ABCG2 transporter. Despite the evidence produced in support of CD133 as a marker for CSC, there is also evidence refuting this with one paper showing that both $CD133^+$ and $CD133^-$ populations contain stem cells (Meng et al., 2009).

Meng et al. (2009) classified their stem cells based on their ability to form colonies, to proliferate, as well as their resistance to chemotherapy. Although this group performed cell separation with an equivalent protocol used in Section 2.2.3, their findings with regards to chemoresistance and colony formation of their cells differs to the findings reported in the present study (see Section 2.3). Meng et al. (2009) reported spheroid formation in both of their CD133$^+$ and CD133$^-$ fractions, in contrast to the results discussed above (in Section 2.4.2). Additionally, Meng et al. (2009) noted a similar drug sensitivity amongst the CD133$^+$ and CD133$^-$ populations. The Hoechst efflux ability of the CD133$^+$ is hypothesised by Ho et al. (2007) to represent the presence of the ABCG2 multidrug efflux pump. As depicted in Fig.2.4 here, some 99.1% of the CD133$^+$ subpopulation were able to efflux Hoechst; and this same population is expected to have the ability to efflux drugs as a mechanism of resistance. Although from this, resistance is only inferred here, it will be further investigated in Chapter 3. The discrepancies between Meng et al. (2009) and the results obtained here as well as those presented by Tirino et al. (2009), Hilbe et al. (2004) and Salnikov et al. (2010) could well be as a consequence of the foetal bovine serum (FBS) supplemented medium used by Meng et al. (2009) to culture the stem cells; CD133$^+$ and CD133$^-$ cells were cultured in RPMI-1640 supplemented with 10% FBS. Notably, since FBS has been shown to drive the differentiation of CSCs in culture, this may well explain the presence of stem cells in their CD133$^-$ subpopulation. In the present study, stem cells were only cultured in a defined serum-free medium, to maintain their stem cell properties and to prevent differentiation.

2.5 Conclusion

With CD133 being the cell surface marker for CSC in NSCLC, as discussed in Section 2.4.4, separation of the NSCLC according to this marker was successful in dividing the A549 population into CSCs and non-CSCs. To further validate this separation, the CSCs proved to show sustained growth in a spheroid arrangement and to have Hoechst efflux ability, indicating the presence of the ABCG2 efflux pump. This was contrasted by the inability of the non-CSCs to efflux Hoechst as well as their monolayer growth pattern, both being features of non-CSC properties.

CSC have been shown to be resistant to conventional chemotherapy, resulting in tumour relapse. One mechanism of such resistance is the ABCG2 efflux pump discussed in Section 2.4.3. However, other mechanisms of resistance need to be explored.

CHAPTER 3

Migration and chemoresistance of CSCs

3.1 Introduction

As discussed in Chapter 2, NSCLC A549 cells were separated into CSCS and non-CSCS. Previous research into breast and glioma CSCs have revealed their resistance to conventional chemotherapeutic agents such as Paclitaxel (Diaz and Leon, 2011). The mechanism of this resistance is detailed below. Understanding and targeting pathways conferring this resistance may result in chemosensitisation of CSC populations and improved patient survival outcomes.

3.1.1 Chemoresistance of CSCs

CSCs are able to self-renew and differentiate to form the bulk of the tumour mass, the non-CSCs. It has thus been hypothesised that therapies targeting CSCs will allow for eradication of the entire tumour population (Diaz and Leon, 2011). Most conventional first line chemotherapies for NSCLC, such as Paclitaxel, have proved ineffective against CSCs. The mechanism of resistance of CSCs to therapy is not fully understood but many reasons have been suggested including slower progression through the cell cycle, resistance to oxidative damage, expression of anti-apoptotic proteins, improved cellular repair mechanisms, presence of enzymes that detoxify drugs and the cell surface expression of ATP-dependent efflux pumps (Diaz and Leon, 2011).

Efflux pumps present on CSCs confer resistance

The presence of membrane transporters ABCG2, ABCG5 and ABCB1 confers resistance to conventional chemotherapy by actively effluxing drugs from the CSCs. This makes current chemotherapy such as cisplatine ineffective (Diaz and Leon, 2011). As described previously, the presence of these ATP-dependent efflux pumps was demonstrated in the present study by the Hoechst efflux ability of the NSCLC CSC population (Fig.2.4). Therapies that target these transporters have proven more effective than conventional chemotherapy in treating melanoma (Diaz and Leon, 2011).

Reactive Oxygen Species in CSCs

CSCs have a low metabolic rate with an associated decreased Reactive Oxygen Species (ROS) level, thought to be mediated by increasing intracellular glutathione concentrations (Kobayashi and Suda, 2012). Non-CSCs in a tumour population have high ROS levels associated with their increased metabolism. Many conventional chemotherapy agents and radiation therapy work through inducing DNA damage mediated by the increased ROS in non-CSCs. However, the lower ROS level in CSCs protects them from these agents. Low ROS are associated with decreased apoptosis, further enhancing CSC resistance to chemotherapy mediated cell death (Ding et al., 2015).

CSC hypoxia mediates resistance

An increased tumour bulk will result in areas of hypoxia, due to inadequate oxygen supply. This induces expression of HIF-1, a transcription factor that increases neovascularisation and chemoresistance. CSCs show an increased expression of HIF-1, even in normopoxic conditions, conferring resistance to radiotherapy and chemotherapy. Interestingly, the increased expression of HIF-1 in normopoxic conditions is thought to be mediated by increased EGFR levels associated with CSCs (Diaz and Leon, 2011).

Migration, DNA repair and decreased apoptosis

CSCs show an increased expression of Akt, a protein that increases BCl-2 and Inhibitor of Apoptosis Proteins (IAPs), all decreasing apoptosis and enhancing cell survival. Downregulating IAPs and Bcl-2 in combination with chemotherapy has shown promise in treatment of

advanced carcinomas containing cells expressing the CD133 CSC surface marker (Bertrand et al., 2014).

Conventional chemotherapy is more effective against rapidly dividing cells, which represent the non-CSC subpopulation. CSCs have been reported to be quiescent, with a prolonged G_2 phase of the cell cycle. The increased time in G_2 allows increased DNA repair and reduced apoptosis of CSCs. Research into CSCs showed targeting the checkpoint proteins in this particular phase of the cell cycle, increased apoptosis of these cell (Harper et al., 2010). Additionally, when the CSCs are exposed to chemotherapeutic agents, asymmetrical division favours an increase in the percentage of CSCs within a tumour population (Gottschling et al., 2012). This quiescent population is regulated by pathways such as Akt1, Insulin-like growth factor-1 (IGF-1R), p53, protein kinase C (PKC), Notch, and phosphatase and tensin homolog (PTEN) deleted on chromosome 10. Akt specifically has been implicated in maintaining the slowed cell division present in CSCs. The alteration of the levels of the pathways listed above results in slow cell division, giving CSCs time to repair any DNA damage caused by cytotoxic agents (Gottschling et al., 2012).

Resistance of CSCs to Paclitaxel

Paclitaxel is one of the first line treatments for NSCLC. Paclitaxel is a Taxane; which functions to prevent microtubule breakdown in cells. With this mechanism of action, Paclitaxel is more effective against actively dividing cells, such as non-CSCs (Veldhoen et al., 2013). Paclitaxel also causes an increase in ROS in the non-CSCs and results in increased apoptosis. However, in CSCs, it is ineffective at reducing CSC viability. Paclitaxel is effluxed from CSCs through the ATP-dependent efflux pumps. ROS levels are low, resulting in decreased DNA damage. Should DNA damage occur, the prolonged G_2 phase will provide more time in CSCs than non-CSCs for DNA repair. Should repair not occur, the CSC will continue to survive due to reduced BCl-2 and PAI. Research shows an additional mechanism of resistance of NSCLC to Paclitaxel specifically, namely MDR1 (Gottschling et al., 2012). In a study performed by Kim et al. (2012a), expression of MDR1 by NSCLC can result in a 200-fold increase in Paclitaxel IC_{50} from its normal IC_{50} of 20 nM.

The previously isolated and characterised CSC population (discussed in Chapter 2) was

exposed to Paclitaxel, one of the first line therapies for NSCLC. It was hypothesised to cause less cell death in CSCs through the mechanisms discussed above. The migration rate of CSCs was also compared to non-CSCs to determine whether the rate of migration may contribute to chemoresistance, potentially due to the prolonged G_2 phase discussed above.

The objectives of this chapter are:

- to investigate migration of A549 CSCs compared to non-CSCs;
- and to establish whether there is a difference in chemoresistance of isolated A549 CSCs compared to non-CSCs.

3.2 Materials and Methods

3.2.1 Scratch assay

The migration ability of A549 CSCs and non-CSCs was determined and compared using a scratch assay. Cells of each stable cell line were seeded into 5 cm^3 sterile cell culture dishes in triplicate and grown in CCM (Appendix A.1.2) and CSC medium (A.1.3) for non-CSCs and CSCs, respectively. Once cells in each well reached 80% confluency, individual P200 sterilised pipette tips were used to score a straight line through the centre of the cell monolayer, to produce a cell-free area. The medium from each well was removed followed by three washes with PBS to rid the medium of the detached cells. 2 ml CCM, pre-warmed to 37°C, was then added to each well. For each well the width of the scratch was measured on the Zeiss LSM 780 confocal microscope at 0, 2, 4, 24 and 28 hours after the scratch was made. Three measurements of the width of each scratch was made, the average width being used for subsequent analysis. Data were captured on Microsoft Excel 2013, a line graph plotted and an exponential growth trend line was fitted to the CSC and non-CSCs line graphs. The significance ($P<0.05$) of the growth was compared using a two-sided Student's t-test.

The trend lines, expressing migration ability, were differentiated using the chain rule to produce general expressions for the migration rate of non-CSCs and CSCs. The migration rate of each cell line was then determined at 24 hours after the initial scratch. A bar graph depicting the relative rates of migration of the CSCs and non-CSCs at 24 hours was then plotted.

3.2.2 Chemosensitivity assay

Paclitaxel chemosensitivity was determined for A549 $CD133^+$ and $CD133^-$ cells using the Roche Cell Proliferation Reagent, WST-1. A total of 2×10^4 cells of each cell population were seeded into wells of a 96 well ELISA plate, with 3 sample repeats for each population. The $CD133^+$ cells were grown in 100 µl of stem cell medium (Appendix A.1.3) for 24 hours. The $CD133^-$ cells were incubated in 100 µl CCM (Appendix A.1.2) for 24 hours at 37°C and 5% CO_2. After 24 hours, the medium was removed from the CSCs and non-CSCs and replaced with 0 nM or 20 nM Paclitaxel (Thermo Fisher Scientific) in CSC and non-CSC medium respectively. A Paclitaxel 20 nM solutions was made from the 5 mg stock diluted in 5 ml DMSO and filter sterilised giving the initial solution a concentration of 0.012M. The drug

carrier control used was a filter sterilised 0 nM DMSO solution of CSC medium and non CSC medium for $CD133^+$ and $CD133^-$ respectively.

After the 48 hour drug treatment, 10 µl of WST-1 reagent was added to each well and incubated for 2 hours at 37°C and 5% CO_2. The absorbance for each well was measured at 480 nm against the relevant blanking control using the Biotex ELx800 Elisa plate reader. A blanking control was used in which the WST-1 was added to three wells of CSCs and non-CSCs growing in drug-free media. Median absorbance for the CSCs and non-CSCs were plotted using Microsoft Excel 2013. Statistical significance was determined using a two sided Student's t-test.

3.3 Results

Migration ability of CSCs and non-CSCs in Fig.3.1 shows that non-CSC are able to migrate faster, with a distance covered of 302.5 µm compared with the 153.55 µm covered by the CSCs in the same 28 hour time period. The migration ability of the non-CSCs was statistically significantly greater than CSCs at time points 2 hours, 26 hours and 28 hours after scoring, with P values for those time intervals being 0.05, 0.0005 and 0.0004, respectively. The migration rate for the WT non-CSCs and WT CSCs can be represented by exponential trendlines $f(x) = 24.034e^{0.093x}$ and $g(x) = 4.313e^{0.125x}$ respectively. The migration rate at 24 hours after the initial scratch shows that non-CSC has a greater rate, $20.827\,\mu m\,h^{-1}$, compared with the CSCs, $(10.826\,\mu m\,h^{-1})$, see Table 3.3.1 for details on differentiation calculations. Fig.3.2A contains photomicrographs depicting the visible difference in migration rates of CSCs and non-CSCs, with non-CSCs covering a greater distance in a 24 hour period compared with the non-CSCs. For the same time period, Fig.3.2B shows that the migration rate at 24 hours of non-CSCs is 1.92 times greater than that of the CSCs cells.

The results outlined above indicate that non-CSCs have a higher migration rate than non-CSCs and are expected to be more susceptible to chemotherapeutic agents such as Paclitaxel. In Fig.3.3, the viability of CSC and non-CSC treated with DMSO alone (0 nM Paclitaxel) for 48 hours was set to 100%. As predicted, the viability of the CSCs in 20 nM Paclitaxel treatment for 48 hours showed 71.3%, survival compared with the 47.0% survival of non-CSC in the same treatment. This finding was statistically significant (P=0.0006).

3.3.1 Scratch assay results

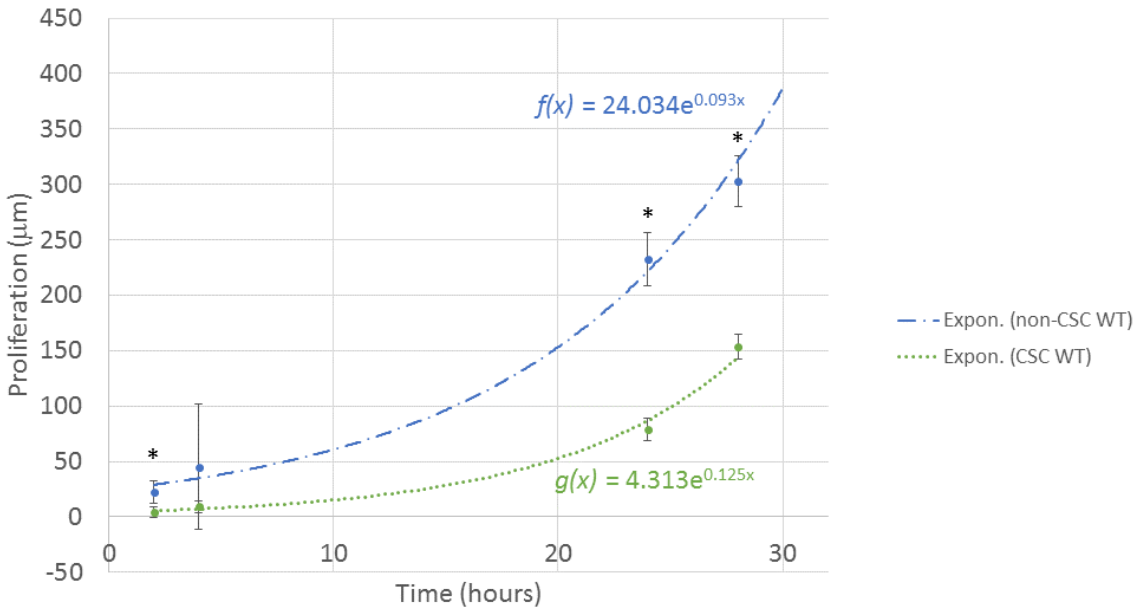


Figure 3.1: Comparison of migration (in µm) of CSC and non-CSC at 4 time intervals (2 hours, 4 hours, 26 hours and 28 hours), following a scratch in 80% confluent cells with a sterilised P200 pipette tip; P= 0.05, 0.33, 0.0005 and 0.0004, respectively. Data are presented as the mean±SD, $^*P<0.05$

Table 3.1: Calculated rate of migration (µmh$^-$1) of WT CSC and WT non-CSCs using the exponential trendlines obtained in Fig.3.1

	Migration distance (µm)	Migration rate (µmh$^-$1)	Migration rate at 24 hours (µm.h$^-$1)
non-CSC WT	$f(x) = 24.034e^{0.093x}$	$f'(x) = 2.235e^{0.093x}$	$f'(24) = 20.827$
CSC WT	$g(x) = 4.313e^{0.125x}$	$g'(x) = 0.539e^{0.125x}$	$g'(24) = 10.826$

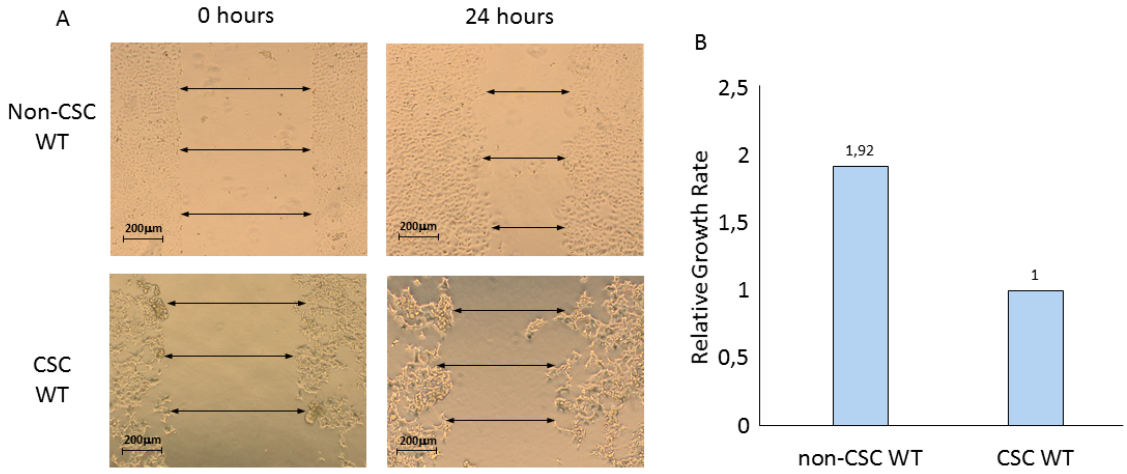


Figure 3.2: Comparison of migration (µm) and relative migration rates of non-CSC WT and CSC WT. **(A)** Photomicrographs of non-CSC WT and CSC at time 0 and at 24 hours (100x magnification). **(B)** Relative migration rate of non-CSC WT and CSC. As is evident, the relative migration rate of non-CSCs exceeds that of the CSCs by almost 2-fold

3.3.2 Chemosensitivity assay results

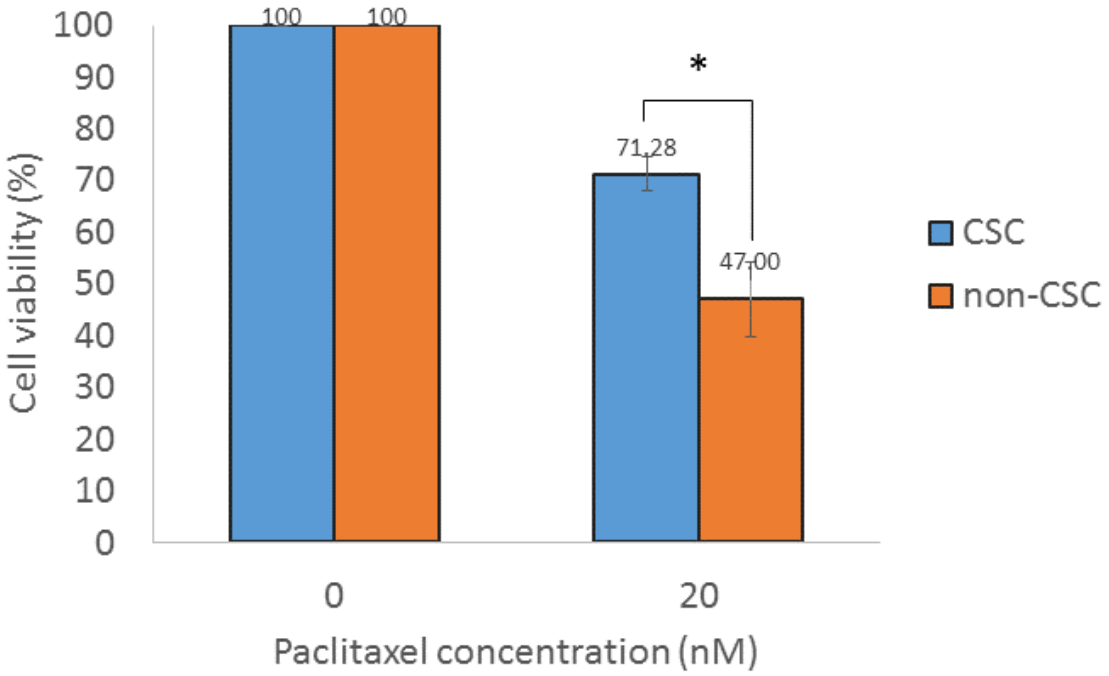


Figure 3.3: Percentage viability of CSC and non-CSC after a 48 hour treatment with 20 nM Paclitaxel. There is a significant difference in cell viability between non-CSCs and CSCs at 20 nM Paclitaxel (P=0.0006). Data are presented as the mean±SD (*P<0.01)

3.4 Discussion

According to the scratch assay (Fig.3.1), motility of non-CSCs at 26 and 28 hours was significantly greater than that of CSCs (P=0.0005 and P=0.0004, respectively). Consistent with this was the relative motility rate of non-CSC, which was calculated at 1.92-fold greater than that of the CSCs (Table.3.3.1 and Fig.3.2). These results are consistent with the results obtained by Pastò et al. (2012) that confirmed CSCs have a decreased motility compared to their non-CSC counterparts. The mechanism for this can be explained by the relative quiescence of CSCs described above in Section 3.1.1. In brief, as described in the literature, the CSCs have a prolonged G_2 phase, increasing the cell cycle length. Akt and other proteins have been implicated in maintaining the slow division of CSCs and the resulting decreased rate of motility compared with non-CSCs.

The chemosensitivity assay results show non-CSC being more sensitive to Paclitaxel, compared with CSCs at 20 nM, the IC_{50}, with viability after a 48 hour drug treatment being 47.0% and 71.3%, respectively (P=0.0006). The relative resistance of the CSCs can be explained through a combination of the mechanisms of resistance as previously described in this study (Section 3.1.1).

The first mechanism of resistance that the experiments show concordance with is the relationship between migration and chemoresistance. It is reported here that the CSCs have a decreased migration ability compared to non-CSCs (refer to Figs.3.1 and 3.2). This is consistent with the longer G_2 phase described in CSCs that influences chemosensitivity by increasing the time available for DNA repair. Furthermore, decreased ROS production results in less DNA damage and moreover anti-apoptotic proteins increase cell survival should DNA damage occur. All of these factors very likely contribute to the increased viability of CSCs compared with non-CSCs, as reported in the present study (see Fig.3.3).

Another mechanism of resistance of CSCs relates to the efflux of Hoechst 33342 by the CSC population (Chapter 2). As discussed above (Section 3.1.1), Hoechst efflux correlates to the expression of the ABCG2 multidrug transporter which effluxes Paclitaxel leading to chemoresistance by decreasing intracellular Paclitaxel concentration. As shown here, the CSCs had a survival rate of 71.3%, significantly higher than for the non-CSCs, after Paclitaxel treatment. The non-CSCs were more susceptible to Paclitaxel with a viability of 47% after

the same treatment. This can be explained by the lower level of Hoechst efflux demonstrated in this work by these cells (see Chapter 2). It follows that since the non-CSCs are unable to efflux Hoechst, they will be incapable of effluxing Paclitaxel, allowing the drug to exert its antimitotic effect on the cells, resulting in higher cell death than was evident for the CSCs.

Another proposed mechanism to explain chemoresistance lies with Hypoxia-inducible Factor-1 (HIF-1). The chemosensitivity assay was performed under normopoxic conditions indicating that HIF-1 expression, a proven contributor to chemoresistance would be mediated by EGFR rather than hypoxia. Diaz and Leon (2011) found that overexpression of EGFR induces HIF-1, which in turn decreases drug sensitivity. The A549 cell line is known to overexpress WT EGFR and as such, this mechanism of resistance is likely to exist in NSCLC. Although it is well-known that EGFR is overexpressed in the A549 population, the relative expression of EGFR in the CSC and the non-CSC subpopulations needs to be characterised. Should EGFR in NSCLC be increased compared with the non-CSCs, it could provide insight into a potential key driver of chemoresistance in CSCs. As described, a raised EGFR expression is linked to two of the mechanisms for CSC resistance as described above. EGFR activates Akt which is responsible for the quiescence seen in CSCs that allows for improved DNA repair. As previously mentioned, EGFR increases HIF-1 that also enhances chemoresistance. Further potential roles of EGFR in chemoresistance and maintenance of CSCs will be considered in detail in Chapter 4

Notably, despite the proposed increased levels of EGFR in CSCs, the migration rates in CSCs are reduced, compared to non-CSCs. This suggests that the high EGFR levels in CSCs are not directly controlling cell migration, but may possibly create a selective advantage for the survival of this population, by increasing quiescence together with the potential for DNA repair, as well as enhancing chemoresistance. Both knockdown and overexpression studies of EGFR may help to further understand its regulatory role in CSCs.

It has been reported by West et al. (2008) that some 80% of NSCLC overexpress WT EGFR and which is reflective of the A549 tumour cell population. EGFR expression has a role in chemoresistance of both the CSCs and non-CSCs through increased HIF-1 expression as detailed above. Additionally, EGFR expression increases Akt expression which, in turn, increases CSC quiescience and improves DNA repair and chemoresistance. Since EGFR overexpression and CSCs both confer resistance to chemotherapy, perhaps the chemoresistance

of CSCs is because of the increased expression of EGFR. In order to further validate this theory, EGFR expression in CSCs should be compared to non-CSCs.

3.5 Conclusion

The results presented in this Chapter showed a higher chemoresistance of CSCs than non-CSCs; this may be caused by the presence of ABCG2 efflux pumps and the EGFR mediated increased CSC quiescience and increased HIF-1 expression. NSCLC commonly shows EGFR overexpression. Such overexpression itself plays a role in the resistance of this tumour to chemotherapy agents such as Paclitaxel. With this in mind, determining the level of EGFR expression within the CSC populations may yield additional insight into its resistance mechanisms to chemotherapy. Thus, the relative EGFR expression in CSCs and non-CSCs will be evaluated in the subsequent Chapter.

CHAPTER 4

EGFR expression in CSCs compared to non-CSCs

4.1 Introduction

The establishment of A549 CSCs and non-CSCs in the present study provides an opportunity to compare differences in protein expression, in particular, relative EGFR expression within these subpopulations. CSCs are known for their ability to self-renew, and have been implicated in the resistance of NSCLC to chemotherapy and radiation therapy as well as tumour relapse. West et al. (2008) reported that 80% of NSCLC overexpress WT EGFR, as is documented in the A549 cell line, and moreover is associated with poorer radiotherapy outcomes (Khan and Ehtesham, 2015). Considering that EGFR and CSCs are associated with poorer prognoses and increased resistance to therapy, it is suggested that EGFR expression is modulated within the CSCs, potentiating their resistance to treatment. EGFR levels have thus far been reported increased in brain tumour CSCs and moreover has been shown to increase their ability to self-renew (Khan and Ehtesham, 2015). The relative expression levels (mRNA) of this receptor in the CSC and non-CSC subpopulations in NSCLC, and in the A549 cell line, has yet to be established (Singh et al., 2012).

4.1.1 EGFR

EGFR is one of four receptors within a family including ErbB1 or HER1 (more often termed EGFR), HER2, HER3 and HER4. ErbB1, or EGFR, is a receptor tyrosine kinase (West

et al., 2008). It has functions in cell survival, differentiation, migration, cellular proliferation and apoptosis. EGFR is present at the cell membrane as a monomer. EGFR has six ligands that cause its activation amongst them, EGF and TGF-α. Upon stimulation, cell membrane associated EGFR becomes dimerised resulting in phosphorylation of its cytoplasmic tyrosine kinase domain. EGFR can also be phosphorylated by protein kinase C (PKC), with this regulating distribution of EGFR in the cell membrane. The final fate of EGFR is degradation in endosomes, but until entry into these endosomes, EGFR maintains its signalling function in the cytoplasm (Nakada et al., 2013; West et al., 2008).

EGFR is often overexpressed in tumours, through abnormal stimulation or genetic mutation providing an advantage for excessive cell proliferation and ultimately cancer development. EGFR overexpression is a common occurrence in NSCLC and gliomas. The A549 NSCLC adenocarcinoma cell line used in this study displays EGFR WT overexpression (Singh et al., 2012). EGFR's downstream activation of the PI3K/Akt pathway results in increased cellular survival and inhibition of apoptosis while Ras/Raf/MEK/ERK and phospholipase C have roles in cellular proliferation. EGFR is thought to mediate cell migration, invasion and epithelial-mesenchymal transition (EMT) in cancer cells. Interestingly, EMT in NSCLC has been shown to be evident in the CSC subpopulation. This, and other EGFR-driven characteristics present in CSC have been strongly correlated to chemoresistance (Singh et al., 2012).

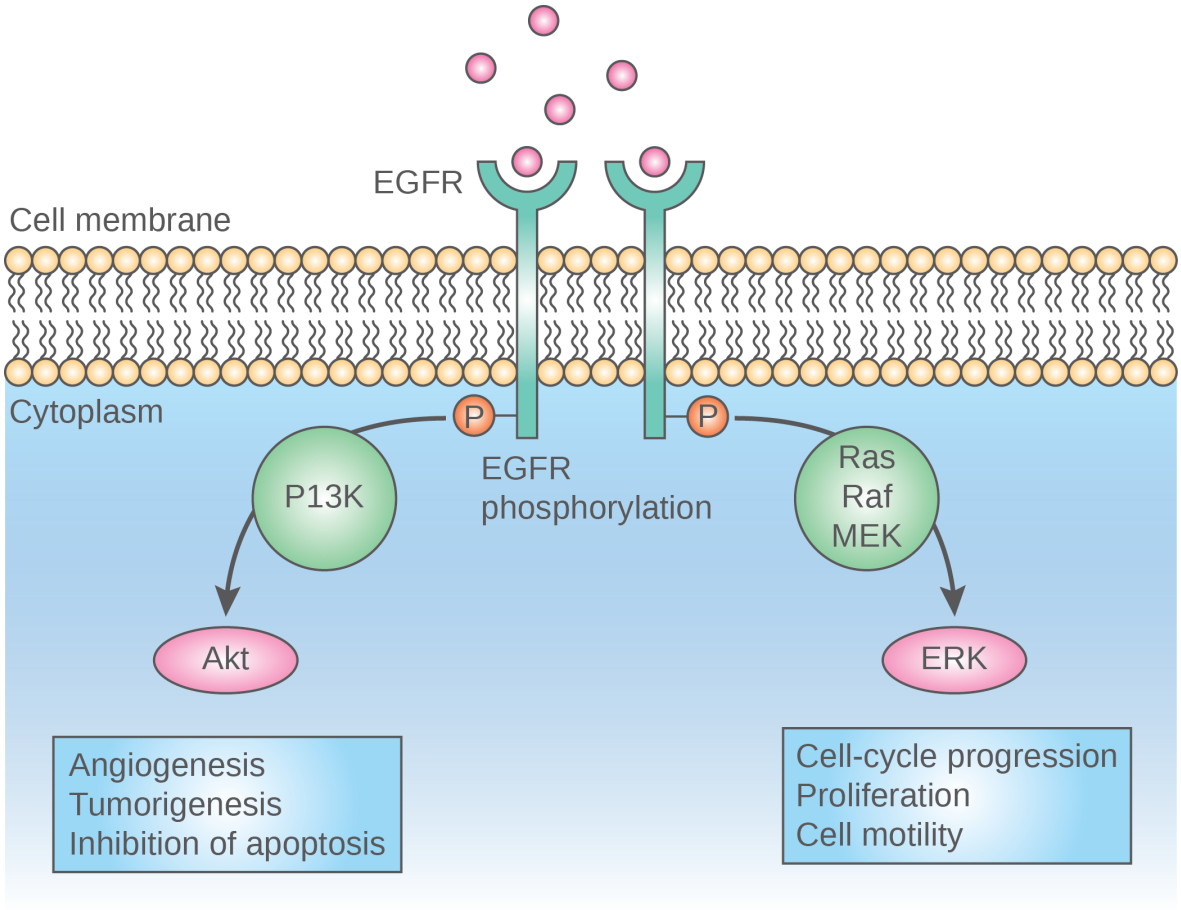


Figure 4.1: Outline of EGFR pathway. Adapted from Nyati *et al.* (2006)

4.1.2 Role of EGFR in CSCs

The role of EGFR in CSCs is highly topical since it has been described that NSCLC and glioma CSCs overexpress EGFR. Subsequent research implicates EGFR in the maintenance of CSC characteristics, many of which directly contribute to their chemoresistance. The potential role of EGFR in EMT is believed to be vital for tumour progression (Appert-Collin et al., 2015). Furthermore, EGFR overexpression in CSCs has shown to contribute to spheroid formation, expression of ABCG2 efflux pumps and the expression of HIF-1, all providing the CSC subpopulation with a survival advantage when exposed to chemotherapy and radiation therapy. In the present study, as NSCLC CSCs demonstrated Paclitaxel resistance and since A549 cells overexpress EGFR, it is proposed here that the resistance of these cells is possibly due in part to increased EGFR levels in the isolated CSCs. Thus, the EGFR levels associated with the CSCs are evaluated here, using real time reverse transcriptase PCR assays and IF.

EGFR and spheroid formation

As previously described, a particular characteristic of CSCs is their ability to grow in three dimensional spheres *in vitro* as opposed to the adherent monolayers of their non-CSCs counterparts (Fig.2.2). High levels of EGFR expression have been linked to driving spheroid formation in glioma CSCs (Liu et al., 2013). Of more relevance to the present study, blocking EGFR with inhibitors suppressed the formation of spheroids, in A549 CSCs, further indicating a dependency on the high expression of EGFR in these cells. Eyler et al. (2008) elucidated that it is the downstream activation of Akt by EGFR that is responsible for the sphere formation, since Akt inhibition prevented sphere formation, whilst also inducing apoptosis.

Hypoxic niches

As briefly mentioned in Chapter 3, as the tumour bulk increases in mass, hypoxic niches develop. Cells in these regions are forced to reach metabolic demands through anaerobic respiration and as a result produce more lactic acid. The lower pH induces the several transcription factors, including hypoxia-induced factor-1, or HIF-1. HIF-1 induces transcription of vascular endothelial growth factor (VEGF) to improve the supply of blood to the hypoxic niche. HIF-1 is also found to increase radioresistance in solid tumours (Morrison et al., 2010). Interestingly, HIF-1 levels in CSCs is increased despite normopoxia indicating another factor is responsible for its increase. Research by Morrison et al. (2010) shows the increased EGFR expression in CSCs is directly responsible for increased HIF-1 in the absence of hypoxia. The increased HIF-1 in this population is thought to contribute towards its resistance to conventional therapies. An increased expression of EGFR and HIF-1 as seen in NSCLC CSCs is associated with a poorer patient prognosis.

EGFR increases Bcl-2 expression

As previously discussed in Chapter 3, CSCs are thought to possess resistance to chemotherapy through their overexpression of Bcl-2, an antiapoptotic protein. Like HIF-1, the increased expression of Bcl-2 is noted when EGFR is overexpressed. EGFR activates downstream Akt, which in turns activates Bcl-2, preventing apoptosis. It has been reported that when Akt was

downregulated, so too was Bcl-2 (Diaz and Leon, 2011).

EGFR increases ABCG2 expression

EGFR has been shown by Yang et al. (2013) to increase expression of both Sox-2 and ABCG2. ABCG2 is an ATP-dependent membrane transporter that effluxes drugs from CSCs, providing resistance to chemotherapy. As described in the present study, some 99.1% of purified CSCs displayed ABCG2 expression as assayed through Hoechst efflux ability. Deductively, since ABCG2 expression is high, EGFR expression in this CSC population is expected to be elevated, relative to the non-CSCs. EGFR is thought to increase ABCG2 expression through increasing the expression of the pluripotent transcription factor, Sox-2 (Singh et al., 2012). Singh et al. (2012) demonstrated that inhibition of Sox-2 decreased ABCG2 expression by CSCs in culture.

EGFR increases Sox-2 expression

EGFR is further involved with pluripotency factors, acting to increase Sox2 expression by phosphorylating Stat3, which once phosphorylated is then responsible for downstream activation of Sox-2 (Singh et al., 2012). Furthermore, increasing EGF concentrations, with the activation of EGFR caused an increased percentage of CSCs within a tumour population. It would then seem that Sox-2, a mediator of stem cell maintenance, may be integral to the EGFR pathway and the self-renewal of the CSC state.

EGFR increases EMT

Another consequence of increased EGFR stimulation with EGF was the increased N-cadherin expression in place of E-cadherin. This phenotype represents dedifferentiation of cells and an increase in the CSC population. Notably, this increased concentration of N-cadherin is thought to be an important step in migration in the EMT model (Yang et al., 2013). An overexpression of EGFR and its ligand, EGF were shown in breast cancer to be linked to metastatic disease and a poorer prognosis. Recent research hypothesises that such EGFR overexpressing cells, being less differentiated and more chemoresistant, may well be CSC (Mallini et al., 2014). Metastatic disease is hypothesised to be a result of EMT which is characterised through the loss of E-cadherin expression and an increased expression of N-cadherin. The epithelial cells develop filopodia at the edge of migrating cells that adhere to the extracellular matrix (ECM). The mesenchymal cells are able to contract actinmyosin filaments to migrate.

Role of EGFR in CSCs

In this Chapter, EGFR mRNA expression is compared in the A549 CSCs and non-CSCs using qRT-PCR. Although qRT-PCR can identify changes in EGFR mRNA expression, these changes may not be directly proportional to EGFR expression and this is discussed further in Section 4.4.. Thus, subsequent qualitative studies using confocal microscopy were performed to produce more robust results of the comparative EGFR expression in the CSC and non-CSC populations.

The objectives for this chapter are:

- to perform qRT-PCR to compare EGFR mRNA in CSCs and non-CSCs;
- to use IF to assess qualitative patterns of EGFR expression in CSCs and non-CSCs;
- and to explore the link between CSCs EGFR expression and chemoresistance.

4.2 Materials and Methods

4.2.1 qRT-PCR EGFR mRNA expression in A549 CSC and non-CSCs

RNA extraction of $1x10^6$ cells from three biological repeats of A549 WT non-CSCs and A549 WT CSCs was performed using the RNA extraction kit (Qiagen) and RNA products were diluted to 200 ng µl^{-1} in RNase free water.

cDNA synthesis was performed using the TaqMan cDNA reverse transcription kit (Thermo Fisher Scientific). 3.8 µl of RNA at a concentration of 200 ng µl^{-1} from each biological replicate of A549 non-CSC and A549 CSC sample was added to a sterilised PCR tube containing 2 µl 25mM $MgCl_2$ with 1 µl 10X RT buffer, 1 µl random hexamers, 1 µl RNase inhibitor, 1 µl deoxyNTP mixture and 0.2 µl MultiScribe Reverse Transcriptase 50 U/µl to a final volume of 10 µl. Reverse transcription was performed in the Biorad MJ Mini with a hexamer incubation at 25°C for 10 minutes, reverse transcription at 37°C for 60 minutes and a reverse transcriptase inactivation step at 95°C for 5 minutes.

For each of the three A549 non-CSC and A549 CSC biological repeats, two replicates of 10 µl qRT-PCR reaction mixtures were made, containing 3 µl 50 ng µl^{-1} cDNA, 1 µl each of 25 pmol µl^{-1} forward (F) and reverse (R) primers for each of BA, GAPDH, HBMC, UBC or EGFR and 5 µl AB Applied Biosystems SYBR Green PCR master mix. Reference genes were provided by The Department of Internal Medicine, University of the Witwatersrand. EGFR primers were designed using the NCBI Primer Blast Software. qRT-PCR was performed on an Applied Biosystems 7500 Real Time PCR System with a 5 minute 50°C start for 2 minutes followed by 10 minutes at 95°C, then followed by 40 cycles of 95°C for 15 seconds, 60°C for 1 minute and a 30 second elongation step at 72°C, where data were collected for each step.

Table 4.1: qRT-PCR forward (F) and reverse (R) primer sequences for EGFR and reference gene controls.

	Primer sequence
EGFR F	5'-GCA CCT ACG GAT GCA CTG GGC-3'
EGFR R	5'-GCG TGC GCT TCC GAA CGA TG-3'
BA F	5'-CTG GAA CGG TGA AGG TGA CA-3'
BA R	5'-AAG GGA CTT CCT GTA ACA ATG CA-3'
GAPDH F	5'-TGC ACC ACC AAC TGC TTA GC-3'
GAPDH R	5'-GGC ATG GAC TGT GGT CAT GAG-3'
HMBS F	5'-GGC AAT GCG GCT GCA A-3'
HMBS R	5'-GGG TAC CCA CGC GAA TCA C-3'
UBC F	5'-ATT TGG GTC GCG GTT CTT G-3'
UBC R	5'-TGC CTT GAC ATT CTC GAT GGT-3'

Data analysis was performed with a modified $^{\Delta\Delta}$CT method, developed by Hellemans et al. (2007) which allows for reference gene normalisation for the four reference genes used in this experiment, namely BA, GAPDH, HBMS and UBC. The control chosen for these calculations was the A549 non-CSCs. The equations used to calculate normalised relative quantities (NRQs) were sourced from the Hellemans et al. (2007) paper on which the qBase software is dependent. The steps used for the relative quantification are described in the following section.

4.2.2 qRT-PCR equations used to calculate NRQs

Note: These equations are outlined in the paper published by Hellemans et al. (2007)
1) Convert Cq values into relative quantities:

$$\overline{Cq} = \frac{\sum_{i=1}^{n} Cq_n}{n} \tag{4.1}$$

$$SD = \sqrt{\frac{\Sigma(x - \overline{x})^2}{n-1}} \tag{4.2}$$

2) Calculate ΔCq for each sample

$$\Delta Cq = Cq_{control} - Cq_{sample} = Cq_{non-CSC} - Cq_{CSC} \tag{4.3}$$

$$SD(\Delta Cq) = \sqrt{(SD_{non-CSC})^2 + (SD_{CSC})^2} \tag{4.4}$$

3) Relative quantification (RQ) calculation:

$$RQ = E^{\Delta Cq} \tag{4.5}$$

$$SD(RQ) = \times \ln 2 \times SD(\Delta Cq) \tag{4.6}$$

4)Normalisation factor (NF) for the four reference genes:

$$NF =^4 \sqrt{RQ_{BA} \times RQ_{HMBS} \times RQ_{GAPDH} \times RQ_{UBC}} \tag{4.7}$$

$$SD = \sqrt{\left[\frac{SD(RQ_{BA})}{RQ_{BA}}\right]^2 + \left[\frac{SD(RQ_{HMBS})}{RQ_{HMBS}}\right]^2 + \left[\frac{SD(RQ_{GAPDH})}{RQ_{GAPDH}}\right]^2 + \left[\frac{SD(RQ_{UBC})}{RQ_{UBC}}\right]^2} \times \frac{NF}{4} \tag{4.8}$$

5) Normalised RQ (NRQ):

$$NRQ_{GOI} = \frac{RQ_{CSC}}{NF} \tag{4.9}$$

$$SD(NRQ) = \sqrt{\left[\frac{SD(RQ_{GOI})}{RQ_{GOI}}\right]^2 + \left[\frac{SD(NF)}{NF}\right]^2} \times NRQ \tag{4.10}$$

4.2.3 Confocal microscopy assessment of EGFR expression in CSC *vs* non-CSCs

To qualitatively, and quantitatively assess the cellular expression of EGFR in the CSC and non-CSCs, confocal microscopy was used. A549 CSCs and non-CSCs were seeded and stained in triplicate according the protocol detailed in Chapter 2, Section 2.2.5. Antibody changes were made to primary and secondary antibodies, these being, rabbit anti-EGFR (AbCam, ab2430) and secondary antibody, anti-rabbit Alexa Fluor 594 (Invitrogen) respectively. The primary antibody and secondary antibody dilutions were 1:500 and 1:200, respectively. The

remainder of the protocol was followed as stated in Section 2.2.5.

When using the confocal microscope, the gain was set and maintained at the same value whilst viewing all the samples, and scan speed was set to 4 with 4 lines/scan. The pinhole was set to 1AU and cells were viewed using the 63× glycerol objective. Images were captured using Zen 2012 software. After this, using ImageJ, the average red and green fluorescence per pixel was calculated for 6 cells per biological sample triplicate, to quantify EGFR and CD133, respectively. These values were compared using a two-sided Student's t-test.

4.3 Results

qRT-PCR was used to determine relative EGFR mRNA expression in the A549 CSC and non-CSC subpopulations. Bustin et al. (2009) released the Minimum Information for Publication of Quantitative Real-time PCR Experiments (MIQE), aiming to ensure consistency in the reporting of qRT-PCR data and to ensure reproducibility of data between laboratories. The qRT-PCR results in Fig.4.2 show a statistically significant increased NRQ for EGFR mRNA expression in A549 CSCs compared to the non-CSCs (P=0.0084). In order to achieve reproducible qRT-PCR results, EGFR mRNA expression was normalised against the four reference genes, GAPDH, HMBS, BA and UBC. The qBase relative quantification framework gave an NRQ for non-CSCs at 1, with a SD of 3.54, relative to the NRQ for CSCs at 16.68, with a SD of 4.49. These statistically significant results indicate that the EGFR mRNA expression in CSCs is higher than that of the non-CSCs.

The MIQE guidelines caution that the presence of mRNA does not necessarily translate to an increased protein expression. As a result, protein studies are a necessity when analysing alterations in EGFR levels within CSCs and non-CSCs. In an article published by Chen et al. (2002), mRNA and protein expression were found to be discordant in NSCLC. According to Mehra et al. (2003), proposed reasons for the discrepancies include competition for tRNA and the concentration of ribosomes within the cells. With this in mind, protein expression studies using confocal microscopy were also performed, as qRT-PCR does not validate a change in protein levels.

Results in Fig.4.3A give evidence that EGFR and CD133 appear to be distributed throughout the cytoplasm in both A549 subpopulations. The EGFR and CD133 staining in the CSCs is more intense than the non-CSCs. CSC images also show co-localisation of EGFR and CD133, indicated by yellow staining. Fig.4.3B shows a statistically significant difference in expression of EGFR and CD133, P=1.04 $\times 10^{-}5$ and P=4.78 $\times 10^{-}8$ respectively, with CSCs having a higher expression of both proteins.

4.3.1 qRT-PCR EGFR mRNA expression in A549 CSCs and non-CSCs.

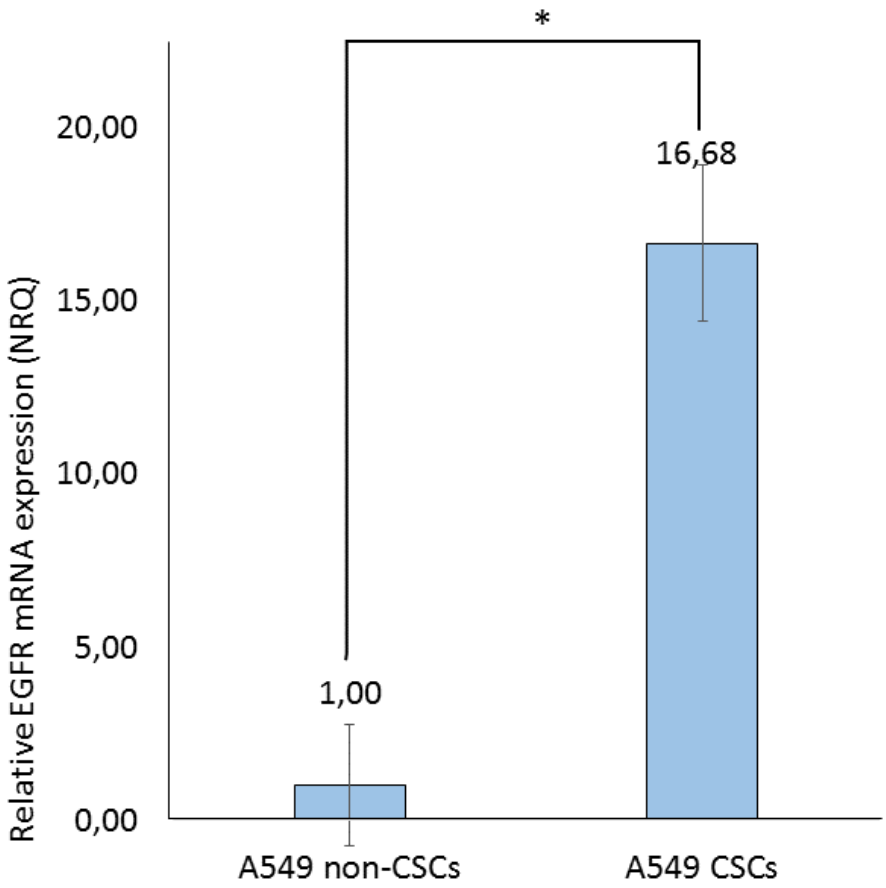


Figure 4.2: qRT-PCR normalised relative Cq (NRQ) of EGFR mRNA expression in A549 CSCs and A549 non-CSCs showing the increased NRQ in CSCs (16.68) compared with the non-CSCs (1.00); P=0.0084 ($^*P < 0.01$)

4.3.2 Confocal microscopy assessment of EGFR expression in CSCs *vs* non-CSCs

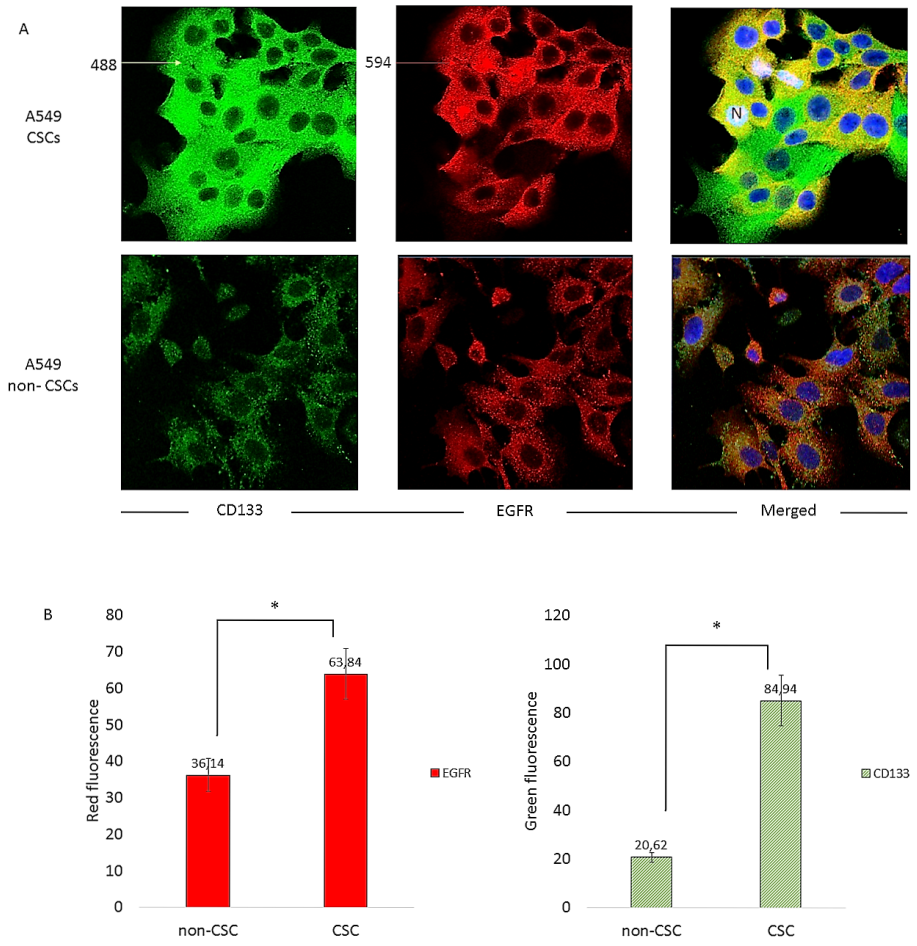


Figure 4.3: Comparison of EGFR expression in CSCs and non-CSCs through confocal microscopy and ImageJ analysis. **(A)** Immunofluorescence images captured with Zen 2012 Software viewed on a Zeiss LSM 780 confocal microscope depicting the expression of CD133 (green), EGFR (red) A549 CSCs (top panel) and non-CSCs (bottom panel) and the nuclei stained with DAPI (blue). The primary anti-CD133 antibody and secondary anti-mouse Alexa Fluor 488 antibody were at 1:500 and 1:100 dilutions, respectively. The primary Rb anti-EGFR antibody (ab2430) and secondary anti-rabbit Alexa Fluor 594 antibody were utilised at 1:500 and 1:200 dilutions, respectively. Co-localisation is shown as yellow, being a merge of the green and red fluorescence **(B)** Bar graphs of A549 CSCs and non-CSCs showing average red fluorescence per pixel indicating EGFR expression; P=1.04 $\times 10^{-}5$ (left); and green fluorescence per pixel indicating CD133 expression P=4.78$\times 10^{-8}$ (right). Data represent measurements from biological triplicates and are presented as the mean $\pm$SD ($^{*}P$<0.0001).

4.4 Discussion

The qRT-PCR (Fig.4.2) and IF results (Fig.4.3) obtained are concordant. It is shown that the CSCs have both increased EGFR mRNA and EGFR protein expression, relative to the non-CSC subpopulation. This increased EGFR expression in CSCs has been previously described by Soeda et al. (2008) in glioma stem cells, who suggest that EGFR plays a unique role in this subpopulation, being implicated in the activation and maintenance of CSC populations and in increasing resistance to conventional chemotherapy.

4.4.1 Role of EGFR in maintenance of CSC state

The IF images in Fig.4.3 show co-expression of CD133 and EGFR in CSCs, but not in non-CSCs. Both of these proteins are significantly higher in CSCs than in the non-CSC subpopulation. The co-expression of EGFR and CD133 is consistent with results found by Miqueli et al. (2009) in glioma CSCs, indicating a relationship between these proteins. One hypothesis is that EGFR (variant III, specifically) is co-expressed together with CD133, contributing to the stemness of CSCs (Liu et al., 2013).

In NSCLC and glioma CSCs, EGFR is thought to play a role in maintenance of CSC states, including spheroid formation in cell culture and regulation of CD133 and ABCG2 expression (Eyler et al., 2008). In the present study, both mRNA encoding for EGFR and associated protein expression levels are notably raised in NSCLC stem cells.

EGFR expression in NSCLC CSCs could be increased as a result of a constitutively active variant or a greater EGFR copy number, as reported in a study on glioma stem cells by Stoltz et al. (2015). Furthermore, it is thought that the constitutively active EGFR seen in CSCs activates Akt and is responsible for transforming non-CSCs to CSCs (Li et al., 2009).

As discussed previously, spheroid formation is a characteristic of CSCs. The NSCLC CSCs analysed here show high EGFR expression, as compared to the non-CSCs (Figs. 4.2 and 4.3). Consistent with Yang et al. (2013), the CSCs have a spheroid growth pattern (Fig.2.2B). The lower EGFR expression in non-CSCs, may correlate to the absence of spheroid growth in cell culture (Fig.2.2A). In support of this, it has previously been reported that A549 CSCs treated with the EGFR inhibitors, gefitinib and AG1478, displayed a decreased sphere formation *in*

vitro (Kim et al., 2012b). Further, downregulating EGFR inhibits spheroid growth in both NSCLC and breast CSC cultures (Singh et al., 2012; Yang et al., 2013).

4.4.2 Role of EGFR in chemoresistance of CSCs

CSCs have been reported to be more resistant to conventional chemotherapy than non-CSCs and in relation to the Paclitaxel resistance reported here, the elevated EGFR in the CSCs is proposed in the present study to contribute to this resistance. This may conceivably occur through increasing Akt, Sox-2, HIF-1 and ABCG2 expression.

The phosphoinositide-3-kinase (PI3K)/Akt/mTOR pathway is a commonly dysregulated signalling pathway in cancer. With regards to EGFR, increased expression activates downstream Akt. In turn, the Akt/phosphoinositide hydroxykinase pathway in these CSCs increases tumour survival, proliferation and invasion (Hu et al., 2014). Upon inhibition of Akt in CSCs, there was an increase in apoptosis and a decreased proliferation of these cells (Hu et al., 2014). Thus, should the A549 CSC population isolated here be subjected to EGFR or downstream Akt inhibition, they should show less resistance to Paclitaxel. Interestingly, NSCLC non-CSC population was found by Li et al. (2009) to be less dependent than CSCs on Akt for tumorigenesis. These results justify the use of therapies targeted at specific tumour subpopulations.

The expression of pluripotent factors are also associated with CSCs. In respect of this, Singh et al. (2012) found EGFR expression to be higher in CSCs and which subsequently increased Sox-2 protein levels, through the Src/Akt pathway. This is of some importance as Sox-2 is responsible for stem cell renewal. Conversely, with the inhibition of EGFR, Sox-2 protein expression was downregulated, together with self-renewal and stem cell expansion (Singh et al., 2012).

Other pathways are also implicated in the chemoresistance of CSCs to conventional chemotherapy. As stated, EGFR drives HIF-1 in CSC under normopoxic conditions. The Paclitaxel chemosensitivity assay in Chapter 3 was performed under such normopoxic conditions. This, in conjuction with increased EGFR expression, implies that HIF-1 will be preferentially expressed in CSCs conferring resistance. Furthermore, the confirmed increase in EGFR

expression will also increase BCl-2 expression and survival, as was seen in the chemosensitivity assay which displayed less cell death in the CSC population (Chapter 3). The increased EGFR expression in the CSCs also stimulates the progression of cells from an epithelial to mesenchymal phenotype. With this change, the cells display resistance to chemotherapy, consistent with results in Chapter 3. The relatively lower EGFR expression in the non-CSCs will render them less chemoresistant with a lower migratory and metastatic potential (Yang et al., 2013).

4.4.3 EGFR as a potential therapeutic target

It is clear from the above discussion that EGFR mediates chemoresistance in CSCs through multiple pathways. For example, Akt and Sox-2 downstream of EGFR are important for maintenance and tumorigenesis of CSCs specifically. Therapies targeting these pathways might yield better outcomes and prognoses for patients with NSCLC. NSCLC shows resistance to agents such as Paclitaxel. Mechanisms through which EGFR display resistance have been discussed in detail in this chapter and downregulation of EGFR could mitigate these mechanisms to increase susceptibility of CSCs to drugs.

In pre-clinical studies, antagonising EGFR with nimotuzumab in gliomas sensitised the CSCs to conventional chemotherapy (Templeton et al., 2014). Similarly, miRNA-7, a downregulator of EGFR has been shown by Liu et al. (2014) to increase chemosensitivity of NSCLC. Increasing miR-7 expression has been shown to decrease chemoresistance and EGFR expression in A549 cells, thus decreasing proliferation and potentially improving patient prognosis (Webster et al., 2009). Since EGFR is overexpressed in NSCLC, the role of miR-7 as a potential therapeutic for non-CSCs and CSCs should be explored.

4.5 Conclusion

Research on CSCs shows that EGFR is vital in maintaining the stem cell state of CSCs. When EGFR is silenced, the characteristic spheroid growth pattern of CSCs disappears and pluripotent stem cell markers are downregulated, resulting in decreased maintenance and growth of stem cells. Furthermore, increased expression of EGFR together with Akt have been shown to initiate the transition of non-CSCs to CSCs. Akt has also been shown to contribute to the tumorigenesis of CSCs. From such reports, Akt and EGFR stand out as targets for chemotherapy and radiation therapy for CSCs. Most of the aforementioned studies were performed on glioma cell lines.

In the following work, in Chapter 5, the role of EGFR in the maintenance and chemoresistance of NSCLC CSCs is further evaluated. Lentiviruses were synthesised, to assess the effect of constitutively active expression of miR-7 on cellular EGFR expression.

CHAPTER 5

EGFR knockdown mediated by miR-7 transduction

5.1 Introduction

As reported in the present study, EGFR is highly expressed in CSCs. Thus, further evaluate the role of EGFR in CSCs, a novel knockdown approach, targeting EGFR associated miRNA expression was undertaken and is presented here. Briefly, microRNAs are small, non-coding RNA molecules that display complementarity to particular mRNA sequences, targeting them for degradation, as negative regulators of protein expression. In particular, EGFR is regulated by miR-7 expression. By introducing lentivirus mediated stable expression of miR-7 into target cells, will allow for decreased EGFR expression and the role of EGFR in CSC maintenance and chemosensitivity to be further classified.

5.1.1 microRNA biology

In healthy cells, protein expression is tightly regulated. In cancers, such as NSCLC, overexpression of proteins is common, with increased oncogene expression and decreased tumour supressor gene expression driving tumour progression. While there are multiple ways in which protein expression is regulated within human cells, the particular focus here is through microRNAs. microRNAs (miRNAs) are non-coding RNA molecules approximately 22 nucleotides in length that regulate the expression of proteins within a cell (Lim et al., 2003). Over 1000 miRNA molecules and their targets have been identified. Most miRNAs function to downregulate the

expression of their target protein. Through this mechanism, they prevent the overexpression of proteins that would otherwise result in dysregulation of cellular processes and that could lead to uncontrolled proliferation and cancer (Croce, 2009). Lee et al. (1993) were first to correlate mutations, deletions and epigenetic silencing of miRNA with the development of cancer. Like other proteins in the cell, EGFR expression is regulated by miRNA, specifically miRNA-7. Consistent with Croce (2009), changes in miR-7 expression through various mechanisms, such as decreased expression or mutations, have been implicated in the development of EGFR overexpressing tumours.

miRNAs are transcribed by RNA polymerase II as pri-miRNAs, these consisting of between 60 and 100 nucleotides (nt) in length (Starega-Roslan et al., 2011a). Pri-miRNAs have unique hairpin structures that are different from other stem-loop structures present in the nucleus. This hairpin structure has a double stranded stem containing on average 30 bp, with flanking single stranded RNA segments. The pri-miRNA is cleaved by Drosha and DGCR8 in the nucleus to form a pre-miRNA that is transported out of the nucleus by Exportin-5. The miRNA is cleaved by Drosha 11 bp away from the ssRNA, dsRNA junction, resulting in a pre-miRNA that has a 3' overhang and typically has a 16 bp stem that is recognised by Exportin-5. The final miRNA is formed in the cytoplasm when RNaseIII Dicer acts on the pre-miRNA. Only the guide strand of the mature duplex miRNA becomes part of the RISC (RNA-induced silencing complex) (Ryan et al., 2010). The other strand, termed the passenger strand, is degraded. It is at this stage that the seed region of the miRNA binds to the target mRNA. The seed region of the miRNA is identified from position 2–7 of the miRNA sequence and is responsible for binding to the target mRNA at its 3' untranslated region (3' UTR) (Starega-Roslan et al., 2011a). The greater the degree of complementarity between the seed region and the 3' UTR, the greater the inhibition and degradation of the target mRNA (Ryan et al., 2010).

5.1.2 microRNA-7 in regulation of EGFR expression

miR-7 is an important regulator of EGFR expression (Landgraf et al., 2007). The most commonly found miR-7 in *Homo sapiens* is cleaved from hsa-pri-miR-7-1 (Fig.5.1), which is found on chromosome 9, in the intron of the HNRNPK gene (Lee et al., 2011). RNA Polymerase II is thought to be responsible for its transcription. After processing by Dicer and Drosha, the mature miR-7 is incorporation into RISC. The seed region of miR-7 which

is complementary to the 3'UTR of EGFR targets EGFR mRNA for degradation. miR-7 mediated EGFR downregulation causes physiological effects due to its decreased expression of EGFR. miR-7 overexpression is reported to decrease viability, proliferation and the metastatic potential of some tumour cell lines (Webster et al., 2009). miR-7 is not conserved across mammalian species having amplifications and mutations, such as deletions or rearrangements of miR-7, shown in numerous tumour cell lines (Webster et al., 2009).

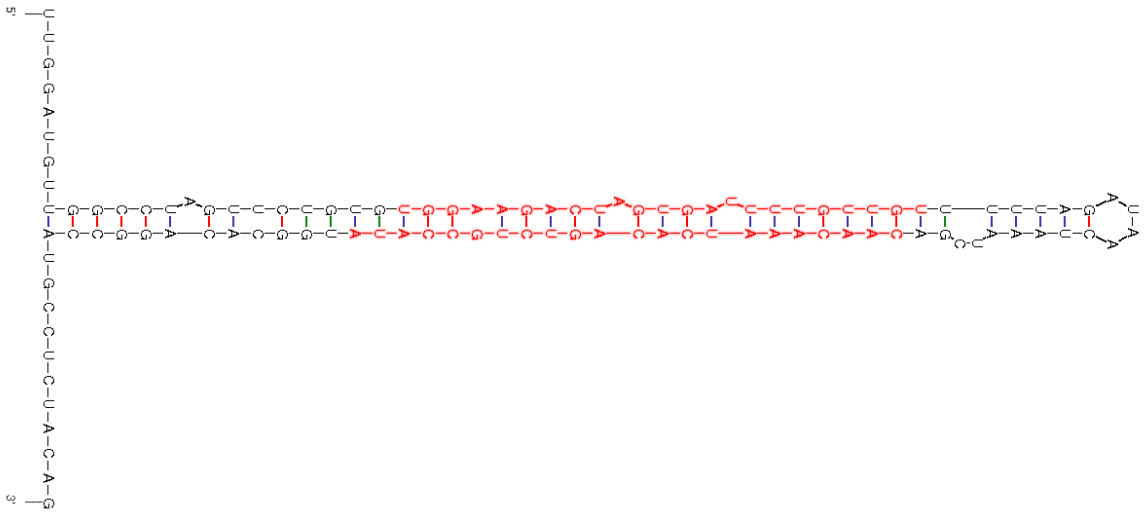


Figure 5.1: Stem loop structure of hsa-pri-miR-7, with miR-7 sequence detailed in red. Image adapted from Landgraf et al., (2003)

It may be hypothesised that a decreased miR-7 level, or a mutated miR-7, could be responsible for an increased EGFR expression in A549 CSCs, and non-CSCs which also overexpress EGFR, but to a lesser extent. Since miR-7 is an important endogenously controlled silencer of EGFR, it was chosen as the mechanism through which EGFR was silenced.

5.1.3 Stable transduction of miR-7 in A549 non-CSCs

miRNA studies require that miRNAs are overexpressed (or silenced) through transfection and transduction techniques to identify their role in cancer pathology. Transduction has the advantage over transfection, as it allows for stable expression of the desired miRNAs within the target genome. Transduction is most often performed with vectors derived from lentiviruses, adeno-associated viruses (AAV) and retroviruses. Some of these vectors have been engineered to allow integration without replication, decreasing biohazard associated risks (Yang, 2015).

Lentiviruses enable transduction of sequences up to 8 kilobases in length. The advantage of lentiviral transduction over the AAV and retroviruses is that it allows for the transduction of rapidly dividing and non-dividing cells (Yang, 2015). The efficiency of this transduction method was demonstrated by Lee et al. (2011), with miR-143 expression increasing some 2500 fold in epithelial cells transduced with lentiviruses containing the pre-miR-143 sequence. Bielewicz et al. (2013) showed that pri-miRNA transduction results in higher knockdown efficiency than both pre-miRNA and miRNA. Thus, in the present study, lentivirus transduction of pri-miR-7 was performed for stable expression of miR-7 in A549 CSCs and non-CSCs. The molecular cloning and lentiviral transduction techniques used in this research are described in Section 5.2. Lentivirus transduction efficiency can be assessed through GFR fluorescence, shown in Sections 5.2.7 and 5.3.2.

With verified cloning and sequencing (Section 5.3.1 and 5.3.5 respectively), it can be determined whether stable transduction of miR-7 was achieved. This stable transduction results in constitutively active expression of miR-7 and allowing for the role of this miRNA in chemoresistance and EGFR expression to be assessed in the isolated cell populations. The efficiency of the transduction is thoroughly discussed in Section 5.4.

Since lentivirus transduction itself may affect the growth rate of A549 cells, a negative control with miR-107 expression was also cloned. The methods for cloning and transduction and the result obtained for miR-107 are discussed alongside those for miR-7.

Note: This chapter deals with the transduction efficiency of A549 non-CSCs. Since the growth rate of non-CSCs is significantly higher than CSCs, transduction was first verified in this subpopulation. Testing of the knockdown efficiency was performed on non-CSCs before transduction was performed on the A549 CSCs.

The objectives of this chapter are:

- to clone hsa-pri-miR-7 and pri-miR-107 downstream of the U1 promoter in a lentiviral plasmid;
- to synthesise lentiviruses containing the U1-hsa-pri-miR-7 and U1-pri-miR-107 sequence;
- to achieve a transduction efficiency of greater than 80% for both hsa-pri-miR-7 and

pri-miR-107;

- to perform a Western Blot to ascertain EGFR knockdown efficiency of miR-7 transduced non-CSCs;
- and to use IF to determine EGFR expression changes resulting from miR-7 mediated knockdown.

5.2 Materials and Methods

5.2.1 PCR amplification of hsa-pri-miR-7 from A549 genomic DNA

HEK293 genomic DNA was used as a template for conventional PCR, from which hsa-pri-miR-7 was amplified. 1.3x10^6 A549 cells were washed twice with PBS after centrifugation for 5 minutes at 300×*g*. The supernatant was removed and PBS was added to a final volume of 200 µl. The *Qiagen DNA Minikit Blood and Body Fluid Spin* protocol was followed for DNA extraction. The 162 ng product was run on a 1% agarose 1% ethidium bromide gel at 100V for 1 hour to confirm extraction and visualised with a BioRad gel doc under UV transillumination to confirm extraction. Both forward and reverse primers were designed manually, with assistance from Marc Weinberg, to contain BSMB1 restriction sites (see Fig.5.2). The primers synthesised by the Department of Molecular and Cell Biology at UCT were used to amplify hsa-pri-miR-7 from HEK293 genomic DNA:

hsa-pri-miR-7 forward primer:
5'-GAT CCG TCT CGT CTC CTG CTT TCT TAC TAA AAA TGA AGA CAT TCA ATA CTA ATC TTG-3'

hsa-pri-miR-7 reverse primer:
5'-GAT CCG TCT CCA AGT GTG TCA AGA AAA ATG ATG AGT AGT AAA TCG GAC A-3'

1 µl (50 ng µl^{-1}) of A549 genomic DNA amplification was performed with a 10 minute PCR hot-start at 95°C, followed by 30 cycles with three steps: denaturation of DNA at 95°C for 30 seconds, annealing at 60°C for 30 seconds and elongation at 72°C for 60 seconds. Once cycling was complete, a final elongation at 72°C was performed. A negative control was run in the same reaction in which the template was omitted and replaced with nuclease-free water. The PCR was run in the Biorad MJ Mini.

5 µl of Gene-rule DNA ladder (Thermo Fisher Scientific) and the products from both PCR reactions were run on a 1% agarose 1% ethidium bromide gel at 100V in TAE buffer for 1 hour, to confirm successful amplification of hsa-pri-miR-7.

Figure 5.2: Diagram of the strategy used to obtain hsa-pri-miR-7 downstream of the U1 promoter in pU1-neo. Forward and reverse primers were designed to contain BsmBI recognition sites. These allowed for digestion of the pri-miR-7 sequence and subsequent ligation downstream of the U1 promoter in the pU1-neo plasmid. More details in Section 5.2

5.2.2 Construction of pU1-neo plasmid with hsa-pri-miR-7 insert

Marc Weinberg provided the pU1-neo plasmid that allowed for the insertion of the hsa-pri-miR-7 PCR product downstream of the PolII U1 promoter. The cloning strategy designed with assistance from Marc Weinberg is illustrated in Fig.5.2. pU1-neo-miR107 was provided for this project by Marc Weinberg to serve as the negative control.

2 µl (100 ng µl^{-1}) of pU1-neo plasmid was transformed with competent *E. coli* DH5-α. A negative control was also performed in which dH_2O was added to the competent bacteria in place of the plasmid DNA. DH5-α transformed with hsa-pri-miR-7 and the control were streaked using aseptic technique onto separate Ampicillin agar plates (prepared according to B.1.2) and were incubated overnight at 37°C. One colony was picked and inoculated into LB Ampicillin broth (prepared according to A.3.3 in Appendix A) for 16 hours. The plasmid was prepared with the QIAprep Spin Miniprep kit. The integrity of the plasmid was confirmed by digestion with NotI and the digested product was run on a 1% agarose 1% ethidium bromide gel at 100V to confirm isolation of pU1-neo plasmid.

PCR cleanup of A549 hsa-pri-miR-7 was performed using the Qiagen Mini DNA kit. 30 ng of hsa-pri-miR-7 cleaned PCR product and 100 ng pU1-neo were digested in separate reactions with 0.5 µl NEB BsmBI in 2 µl 2xNEB buffer 3.1 and made up with dH_2O to a final volume of 20 µl. Digestion proceeded for 1 hour at 55°C and enzyme heat inactivation was performed at 80°C for 20 minutes.

40 ng of BSmBI digested pU1-neo and 21ng digested hsa-pri-miR-7 products were ligated in a reaction containing 2 µl Thermoscientific ligation buffer and 1 µl T4 DNA ligase, made up to 20 µl with dH_2O. 1 µl Thermoscientific FastAP was added to the pU1-neo digestion reaction. A ligation control was performed to the same volume with dH_2O in place of the hsa-pri-miR-7 insert. After a 1 hour ligation at 22.5°C followed by a 20 minute 80°C heat kill step, 2 µl hsa-pri-miR-7 pU1-neo ligation product and the ligation control were transformed in two separate vials of 100 µl of competent DH5-α. Three colonies were selected from the hsa-pri-miR-7 pU1-neo bacterial Ampicillin agar plate and inoculated in separate sterile vials of 4ml Ampicillin LB broth (Appendix A.3.3) and grown overnight at 37°C. Plasmids from each sample were prepared with the QIAprep Spin Miniprep kit and 100ng of plasmid were digested with 1 µl NotI and 1 µl XbaI for 1 hour at 37°C. Products were run on a 1% agarose

1% ethidium bromide gel at 100V for 1 hour and visualized with a BioRad gel doc under UV transillumination. Digestion was used to verify the correct insert of 700bp, the size of hsa-pri-miR-7 downstream of the U1 promoter.

5.2.3 Construction of pHIV-7-GFP plasmid containing U1-hsa-pri-miR-7 and U1-pri-miR107

pHIV-7-GFP was donated by Bryan Welm and Zena Werb (Welm et al., 2008). pU1-neo-hsa-pri-miR-7, a positive clone was selected for insertion into the pHIV-7-GFP multiple cloning site (MCS) by simultaneous digestion of 100 ng pHIV-7-GFP and 100 ng pU1-neo-hsa-pri-miR-7 with 1 µl NotI and 1 µl XbaI in 2 µl Buffer O. Digestion products were run on a 1% agarose 1% ethidium bromide gel at 100V. The pHIV-7-GFP backbone and the hsa-pri-miR-7 clone A insert were gel extracted with Thermoscientific GeneJet Gel extraction kit. Ligation was performed at 22.5°C for 1 hour with 30 ng pHIV-7-GFP gel extracted vector and 20ng pU1-neo-pri-miR-7 insert using 2 µl Thermoscientific ligation buffer and 1 µl T4 DNA ligase in a 20 µl reaction, made up with dH_2O. Ligation was followed by a 20 minute enzyme denaturation at 80°C. A control ligation was simultaneously performed with dH_2O in place of the U1-hsa-pri-miR-7 insert. For transformation, a 100 µl vial of competent textitE. coli DH5-α was thawed after which 2 µl of reaction product was added to the *E. coli* DH5-α. The cells were heat shocked at 42°C for exactly 90 seconds. Post transformation, the competent bacteria containing the ligation product from the U1-hsa-pri-miR-7 and pHIV ligation and the control were spread using aseptic technique onto Ampicillin agar plates (Appendix B.1.2) and were incubated overnight at 37°C. Three colonies were picked and inoculated into three separate vials of Ampicillin agar broth (Appendix A.3.3) and grown overnight in a shaking incubator at 200 RPM and 37°C. Each vial was used in a plasmid preparation with the QIAprep Spin Miniprep kit.

50 ng of plasmid from each of the three broth cultures was digested with 1 µl Thermoscientific BamHI in 2 µl BamHI buffer in a total volume of 20 µl made up with dH_2O. 50 ng of the previous round pU1-neo-hsa-pri-miR-7 was digested with NotI and XbaI in 2 µl Buffer O and made up to 20 µl with dH_2O, to act as a control. Digestion products were run on a 1% agarose 1% ethidium bromide gel at 100V and viewed with a Biorad gel doc under UV light. Results of this cloning are shown in Fig.5.3

For the negative control, U1-pri-miR-107 clone A was selected for ligation into pHIV-7-GFP. 200 ng of pU1-neo-miR-107 DNA was used to transform competent *E. coli* DH5-α. Ampicillin agar plates (Appendix B.1.2) were warmed in the 37°C incubator. A 100 µl vial of competent *E. coli* DH5-α were thawed and 2 µl of plasmid DNA was added to the cells and placed on ice for 30 minutes. After this time, the cells were heat shocked for exactly 90 seconds at 42°C. After transformation, the bacteria were spread using aseptic technique onto an Ampicillin agar plate and incubated for 16 hours at 37°C. After the incubation period, three colonies were picked and inoculated into three separate vials of 5 ml LB Ampicillin broth and this was incubated for a further 16 hours in a 37°C shaking incubator. Plasmid preparation was done using the QIAprep Spin Miniprep kit (Qiagen, Germany). Following this, the same cloning procedure outlined for pHIV7-GFP-U1-hsa-pri-miR-7 was used to achieve pHIV7-GFP-U1-pri-miR-107. Confirmation of successful cloning was performed by digesting the pHIV-pri-miR-107 with BamHI (results are shown in Fig.5.5). Fig. 5.3 below outlines the above mentioned cloning strategy employed.

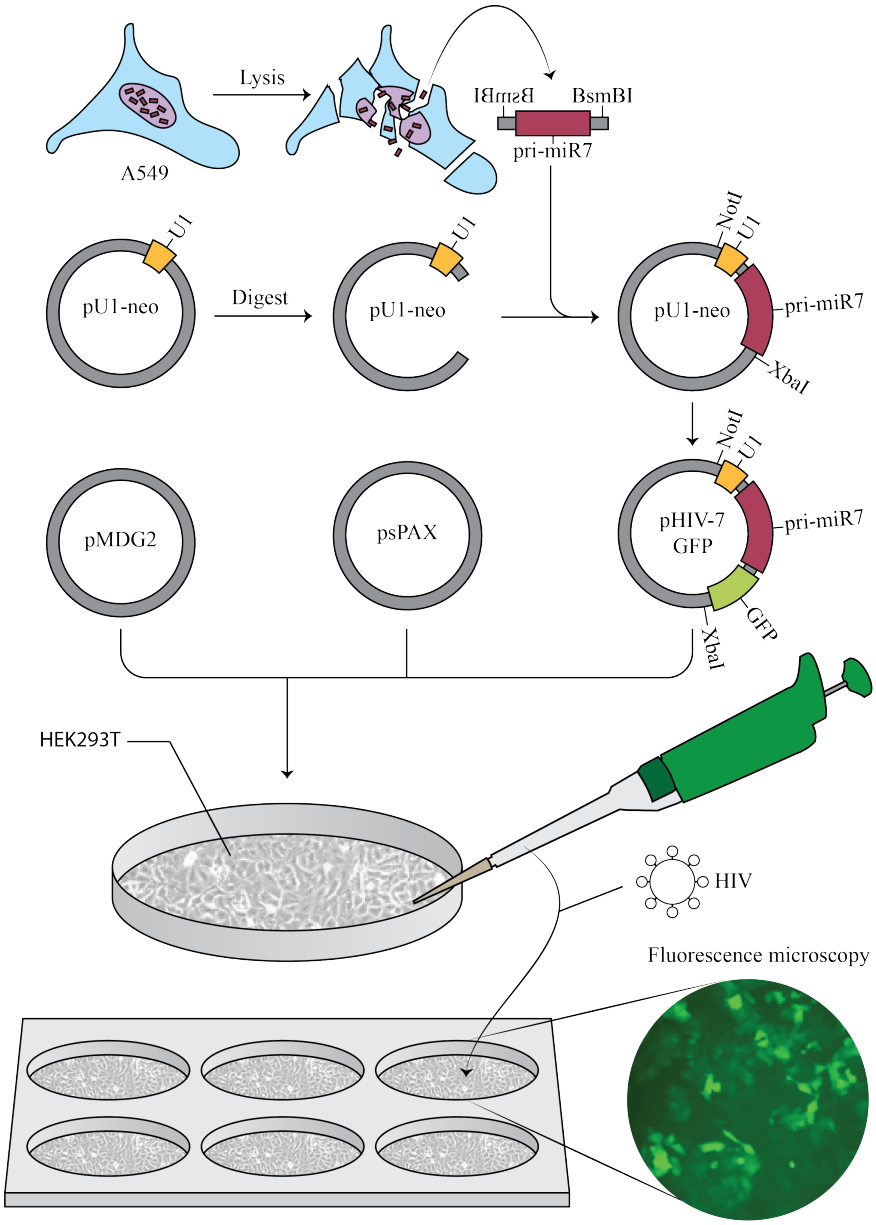


Figure 5.3: Summary of cloning strategy employed to create A549 CSC and non-CSC with constitutive expression of miR-7 and miR-107 using lentiviral transduction techniques. miR-7 was amplified through PCR with BsmB1 sites both upstream and downstream of the pri-miR-7 sequence. pri-miR-7 sequence was then cleaved at the BsmBI sites and ligated into the pU1-neo plasmid following which the U1-pri-miR-7 construct was cleaved with NotI and XbaI and ligated into pHIV-7. HEK293T cells were transduced with pMDG2, psPAX and pHIV-7-GFP. The lentiviral products were collected and used to transduce A549 non-CSCs.

5.2.4 Verification of successful pHIV-7-GFP-U1-hsa-pri-miR-7 clone

Sequencing of pHIV-7-GFP-hsa-pri-miR-7 clone A and pHIV-7-GFP-pri-miR-107 was performed by Inqaba Biotechnologies with the following primers:

pHIV-7-GFP forward:
5'-GTA GAC ATA ATA GCA ACA GAC ATA C-3'

pHIV-7-GFP reverse:
5'-GTA ATC AAT TAC GGG GTC ATT AGT TCA-3'

5.2.5 Lentivirus synthesis

QiaAmp Midiprep kit was used to prepare pHIV-7-GFP-hsa-pri-miR-7, psPAX and pMDG2 (for lentiviral packaging and envelope proteins) where 26.7 µg, 20 µg and 30 µg of plasmid was isolated respectively. PEI transfection with these three plasmids was performed on 80% confluent HEK293T cells in a 100mm x 20mm cell Nest cell culture dish. 26.7 µg pHIV-7 plasmid (containing miR-7 insert), 20 µg psPax and 30 µg pMDG2 plasmid DNA were added to incomplete DMEM-F12. 100 µl of 1000× dilution of Sigma Aldrich unbranched PEI was added to the above plasmid mixture and vortexed for 1 second 15 times. The mixture was incubated for 10 minutes at RT. 6ml of DMEM-F12 with 10%FBS was then added and mixed by inverting five times. The solution was gently aliquoted onto 80% confluent HEK293T cells in a drop-wise fashion, ensuring an even distribution of drops throughout the dish. The dish was swirled carefully so as not to detach the cells. After 3 hours of incubation at 37°C, 20 ml of DMEM-F12 with 10% FBS was poured into the dish using aseptic technique. After 24 hours, the medium was collected from the dish and placed into sterile 1.5 ml Eppendorf tubes, which were then stored at -20°C. 20 ml of cell culture medium was then added to the dish and incubated for a further 24 hours and the medium was again collected and stored in 1.5 ml Eppendorf tubes at -20°C.

5.2.6 NSCLC lentivirus transduction

Both A549 stem and non-stem cells were grown to 80% confluency in 6 well plates with cell culture medium (Appendix A.1.2) and Stem Pro medium (Appendix A.1.3) respectively. Virus titration was performed by adding 200 µl, 400 µl, 600 µl, 800 µl and 1000 µl of lentiviral

transfection mixture into separate wells and incubated for 24 hours in a total medium volume of 2000 µl per well. Stem cell transduction was performed in a similar manner, however, the lentiviral cell lysate was centrifuged at 15000 ×g at 4°C for 24 hours to rid the medium of FBS. After the medium was decanted, it was replaced with 1500 µl of StemPro medium and the same titration procedure was followed as with the non-stem cells, with each well filled to a total volume of 2000 µl. Wells of CSCs and non-CSCs were viewed under the fluorescence microscope and the GFP expression noted. The well with the highest transduction efficiency for both stem and non-stem cells was selected for further passages.

5.2.7 Quantification of transduction efficiency using flow cytometry

A 25cm^3 flask of each A549 WT, miR-7 transduced and miR-107 transduced cells were grown to 80% confluency. The medium was removed from each flask, and the cells were washed once with 5ml PBS. Each flask was then incubated with 1ml of Trysin-EDTA for three minutes to promote detachment. Once detached, the trypsin was neutralised by the addition of an equal volume of CCM. Cell suspensions were centrifuged at 800xg for 5 minutes. Cells were washed with 5ml PBS and the centrifugation repeated. Cells were resuspended in a final volume of 5ml 0.5% BSA PBS.

The LSRFortessa BD Pharmigen was used to determine the transduction efficiencies in the miR-7 and miR-107 tranduced A549 populations. Detection of cells containing GFP was performed using the FITC channel, as FITC and GFP share the same excitation and emission wavelengths. Compensation was not necessary for this experiment as only a single channel, namely FITC, was used. Gating of the population to normalise for autofluorescence was performed using the unstained A549 WT, which lacked expression of GFP. Gating was also performed using SSC-A and FSC-A to exclude doublets.

5.2.8 Growth kinetics comparison between A549 WT and A549 miR-107 transduced control

Since EGFR is known to have an impact on proliferation of cells, it is imperative to assess whether the A549 WT has the same growth rate as the miR-107 negative control. Should the growth rates differ, miR-107 will be used as the only negative control for the subsequent experiments performed in this research.

In order to assess relative proliferation rates, a scratch assay was performed. A549 non-CSCs WT and miR-107 transduced cells were seeded in triplicate onto separate 5cm^3 plates. The cells were incubated at 37°C and 5% CO_2 until 80% confluency was reached. A scratch was made with a sterile 200 µl pipette tip along the diameter of each plate. The size of the gap was measured on an Olympus IX71 microscope immediately and at 8 hours, and 24 hours after the scratch was made. A graph of µl proliferation *vs* time was plotted. An exponential trendline was fitted to the growth patterns of both WT and miR-107 transduced non-CSCs with the intercept set at 1.0. Error bars using standard deviation are plotted on the graph. A two-sided Student's t-test was performed to determine statistical significance of the proliferation at each time point.

Exponential trendline equations were differentiated using the chain rule to yield an equation for each of which was used to determine the rate of proliferation (µmh$^-$1) of the cell lines at 24 hours after the initial scratch was made. A bar graph depicting the relative proliferation rates (µmh$^-$1) of the two cell lines at 24 hours was then plotted.

5.2.9 Western blotting

Sample preparation

A549 non-CSC WT, cells transduced with miR-7 and miR-107 were seeded in 25cm^3 flasks. Once 80% confluent, they were subcultured in the same flasks in triplicate. The time from seeding to extraction was approximately 5 days. Cells within each flask were trypsinised in 1ml Trypsin EDTA. An equal volume of complete DMEM was added and suspended cells were centrifuged at 800× RPM for 5 minutes at 4°C and the supernatant discarded. 1×10^6 collected cells were resuspended in 2ml ice cold PBS (Appendix A.1.1) and centrifuged at 800× RPM for 5 minutes. This wash step was repeated once more, and again the supernatant was removed. To the cells, 200 µl RIPA buffer (Appendix A.4.2) and 2 µl protease inhibitor were added followed by vigorous pipetting of the mixture and a 5 minute incubation on ice. Post-incubation, five sonications of 1 minute each were performed on theUltraSonic Cleaner-Memory Quick (EUMAX) with 30 second incubations on ice in between each sonication. Samples were then centrifuged at 16 000 × RPM for 12 minutes at 4°C. 2 µl of each A549 non-CSC WT, miR-7 and miR-107 transduced sample were used for BCA protein quantification.

SDS-PAGE

The Biorad casting stand was used to cast a SDS-PAGE by lining up a short plate and a 1mm spacer plate. An 8% resolving buffer (Appendix A.4.5) was prepared in a sterile 15ml Nunc tube and mixed by inverting the tube 5 times and was then loaded in the space between the two glass plates to 1.5cm below the top of the plates. 2 µl 90% ethanol was gently added above the gel solution. The gel was then left to set. Once set, the ethanol was poured off and filter paper used to remove residual ethanol. A 10% stacking gel was pipetted gently over the top of the resolving gel (Appendix A.4.7), and into this a 10 lane comb was inserted, ensuring no bubbles were present between the gel and the comb. Once the stacking gel had set, the plates containing the gel were transferred to the Mini-PROTEAN® Tetra Cell, and tank buffer (Appendix A.4.9) was poured until it reached the required level for running one gel. 5 µg Spectra™(Thermo Fisher Scientific) multicolour broad range protein ladder, with bands of molecular weight 10kDa, 15kDa, 25kDa, 35kDa, 40kDa, 50kDa, 70kDa, 100kDa, 140, 260kDa, and 20 µg protein samples from WT, miR-7 and miR-107 transduced cells were loaded into the wells; and the gel was subsequently run at 80V until the 5kDA protein band was 1.5cm from the bottom of the gel.

Transfer

The gel was removed from the Mini-PROTEAN® Tetra Cell and placed on top of a pre-cut Sigma Aldrich nitrocellulose membrane. Transfer was performed in transfer buffer (Appendix A.4.10) in a 5°C cold room at 15V overnight. The membrane was cut at the 75kDa marker and placed into two separate petri dishes.

Antibody staining

Blocking was performed for 1 hour in blocking buffer (Appendix A.4.11) on a shaker at 30 revolutions per minute (RPM). After 1 hour, blocking buffer was discarded.

For EGFR detection and BA loading control, 1:1000 primary AbCam Rabbit anti-EGFR (ab2430) and 1:1000 primary AbCam Rabbit anti-BA (ab8227) respectively, were used. Both antibody dilutions were made in blocking buffer. For each petri dish, after a 1 hour primary antibody incubation at 30 RPM, the primary antibody solution was discarded and 3 5-minute washes in 10 ml wash buffer (Appendix A.4.12) were performed.

For each petri dish, secondary antibody staining was performed using the Invitrogen WesternDot™ Western Blot Kit by adding, 4 µl Biotin-XX-Goat anti-rabbit to 8 ml wash buffer and placing this on the membrane. Incubation in secondary antibody was for a duration of 60 minutes with shaking at 30RPM. This was followed by three 5 minute wash steps in 10 ml wash buffer.

After decanting the wash buffer, 4 µl Qdot® 625 streptavidin conjugate was added to 8 ml wash buffer and gently pipetted into each petri dish. Incubation was performed for 15 minutes. Three final 5 minute washes were performed in 10 ml wash buffer followed by a final wash in 10 ml ultra-pure water. All washes were performed on the shaker at 30RPM.

Image analysis

The membranes were carefully placed on the UV transillumination tray in the Geldoc™EZ. The membrane image was captured using SYPRO Ruby software with an exposure time of 1.194 seconds. Lanes and bands for non-CSC WT, miR-7 and miR-107 were manually marked and band density for each band was calculated using ImageJ. EGFR band densities were calculated relative to the BA loading control. A bar graph depicting EGFR expression relative to BA was plotted for non-CSC WT, miR-7 transduced and miR-107 transduced cells.

5.2.10 Confocal microscopy based comparison of EGFR fluorescence in miR-7 and miR-107 transduced cells

Confocal microscopy was carried out as outlined in Chapter 2.2.5, but with changes to the primary and secondary antibodies to Rb Ab Cam anti-EGFR (ab2430) (1:500 solution) and secondary antibody anti-rabbit Alexa Fluor 594 (1:100 solution), respectively. After capturing the images, ImageJ was used to analyse the intensity of red fluorescence in each cell. This was achieved by quantifying the number of red pixels in each cell. The cells were individually assessed by using the RBG analysis which gives a value for average number of red pixels per pixel, this way adjusting for cell size. 6 cells from each of the three biological repeats were analysed and a bar graph of the results drawn. Statistically, significance was tested using a Student's t-test, where $P<0.05$ was considered significant.

5.3 Results

hsa-pri-miR-7 amplification from A549 genomic DNA was confirmed by gel electrophoresis (Fig.C.1, in Appendix C). Gel electrophoresis was also used to confirm successful cloning of U1-hsa-pri-miR-7 into the pHIV backbone; Fig.5.3 shows clones A, B and C, digested with BamHI. Two bands are evident in each lane, one at approximately 9000 bp and the other at approximately 420 bp. The control lane, pU1-neo-pri-miR-7 digested with NotI reveals the U1-hsa-pri-miR-7 insert at approximately 400 bp and the pU1-neo backbone at approximately 6000 bp. With the size of the U1-hsa-pri-miR-7 construct also being 420bp, it shows that the U1-hsa-pri-miR-7 remained intact during the cloning process. To confirm that the backbone has indeed changed from pU1-neo to pHIV-7-GFP, the size of the upper band must be noted. The upper band in the control lane is at approximately 4500bp, the expected size of this plasmid digested with NotI.
Fig. 5.5 shows the successful cloning of miR-107 into the pHIV-7 backbone, with the pri-miR-107 band evident at approximately 400 bp. Once the sequence was confirmed, lentiviruses were synthesised in HEK293T cells by tranfecting the cells with pU1-neo-pri-miR-7, psPAX and pMDG2. Lentiviruses, HIV-7-pri-miR-7, were used to transduce and allow stable expression of hsa-pri-miR-7 in the non-CSCs. The same methodology was implemented in the synthesis of HIV-7-miR-107. Transduction efficiency was determined using flow cytometry. In Fig.5.6, P3 indicates the final gated population adjusted for both doublets and GFP autofluorescence of the A549 non-CSCs. In Fig.5.7, P4 in the HIV-7-miR-7 and HIV-7-miR107 transduced non-CSCs indicates the percentage of the gated population positive for GFP fluorescence. The GFP fluorescence was estimated at 97.9% and 95.8% for the HIV-7-miR-7 and HIV-7-miR-107 transduced non-CSC populations, respectively. The BF images obtained for A549 non-CSC WT, miR-7 and miR-107 show confluent cell growth. The corresponding fluorescence images for the same field show no fluorescence of the WT cells, but green fluorescence for both the miR-7 and miR-107 transduced populations.

U1-hsa-pri-miR-7 was successfully cloned into the pHIV-7-GFP, verified by both analysis of DNA fragments on an agarose gel and by sequencing of the pHIV-7-GFP MCS. Lentiviruses were produced by HEK293T cells and collected for transduction of A549 cells. The HIV-7-miR-7 and HIV-7-miR-107 transduced cells showed 97% and 95% transduction efficiency respectively, according to flow cytometry analysis (see Fig.5.7).

Since miR-7 will affect EGFR levels and, in turn, cell proliferation amd the effect that the lentivirus has on this must be determined using the miR-107 negative control. This will guide whether non-CSC WT will be able to be used as an additional control for miR-7 transduced non-CSCs. It is reported here that the non-CSCs WT showed an increased proliferation, compared with non-CSCs expressing miR-107 which was statistically significant ($P<0.05$) for time points 24 hours and 28 hours; and not significant at time points of 2 hours and 4 hours (see Fig.5.8). Exponential trendlines fitted to the non-CSC WT and non-CSC miR-107 graphs describe their proliferation pattern as $f(x) = 24.034e^{0.093x}$ and $h(x) = 26.584e^{0.075x}$ respectively. Table 5.1 gives calculations of $f'(24)$ and $g'(24)$, showing that the rate of proliferation of non-CSCs WT was greater than that of non-CSCs miR-107, with these rates being $20.827\,\mu m\,h^{-1}$ and $12.06\,\mu m\,h^{-1}$, respectively. As represented in Fig.5.10A, 24 hours after scoring non-CSCs WT and non-CSCs miR-107 with a P200 sterile pipette tip, the proliferation of non-CSC WT is visibly increased, compared with non-CSCs transduced with miR-107. Fig.5.10B gives relative rates of proliferation indicating that the rate of proliferation at 24 hours is 1.73 times greater than that of non-CSCs transduced with miR-107. Both Western blotting and confocal microscopy were used to determine knockdown efficiency of miR-7 transduced non-CSCs. The EGFR expression levels were compared to the negative control, miR-107 transduced non-CSCs as miR-107 has no known effect on EGFR expression.

Western blotting of 20 ng protein shows no visibly evident downregulation of EGFR in non-CSC miR-7 compared with the miR-107 control (Fig.5.10A). Densitometry shows EGFR intensity relative to BA for miR-7 and miR-107 were 4.48 and 5.28, respectively. Although this difference shows miR-7 EGFR expression to be marginally lower than the miR-107 transduced cells, Western blotting is not sensitive enough for this difference to be significant. As such, the EGFR levels seen in the Western blot are approximately equal, as shown by Fig.5.10B, suggesting knockdown was not achieved.

Since no knockdown was seen with Western blotting, the pHIV-7 containing the pri-miR-7 construct was sent for sequencing. Four sequencing reads were obtained. Sequencing results, shown in Fig.5.11, were analysed using SnapGene and verified by manual comparison between plasmid design sequence and sequencing results obtained from Inqaba Biotech. NSCLC has been shown to have mutations in miR-7, with this hypothesised to be one of the causes of EGFR overexpression. Interestingly, the sequencing results show an A→G point mutation

at position A20, from the 3' pre-miRNA terminus. This mutation was not in the miR-7 seed region or in miR-7 but was near the 3' end of the pri-miR-7. Since this sequence was isolated from HEK293 cells, there is a possibility that this mutation is one that may occur in cancer cells and may be responsible for pathogenesis. As such, confocal microscopy of cells transduced with this miR-7 was performed to assess the possible effect this miRNA has on EGFR expression in the cells.

Notably, confocal microscopy images in Fig.5.12A appears to show lower EGFR expression in A549 non-CSCs miR-7 transduced cells, as compared to the miR-107 transduced negative control. The EGFR expression in the miR-7 transduced non-CSCs shows differential localisation of EGFR in the nucleus with very little EGFR expression in the cytoplasm and on the cell membrane. The EGFR expression in the miR-107 cells was diffuse, present extensively in the cytoplasm and on the cell membrane, with much less EGFR expression in the nucleus compared with the miR-7 transduced cells. These expression patterns were observed for all samples collected and analysed.

ImageJ analysis of the confocal microscopy images in Fig.5.12B showed that the concentration of red fluorescence per cell, adjusted for cell size, indicates that mean red fluorescence in the miR107 transduced cells is 14.56 compared with 8.61 in the miR-7 transduced cells. These results were statistically significant with P=0.00616. This infers that the EGFR expression in miR-7 transduced cells is lower than in the miR-107 transduced cells.

5.3.1 Verification of pHIV-7-GFP plasmid containing U1-hsa-pri-miR-7 insert

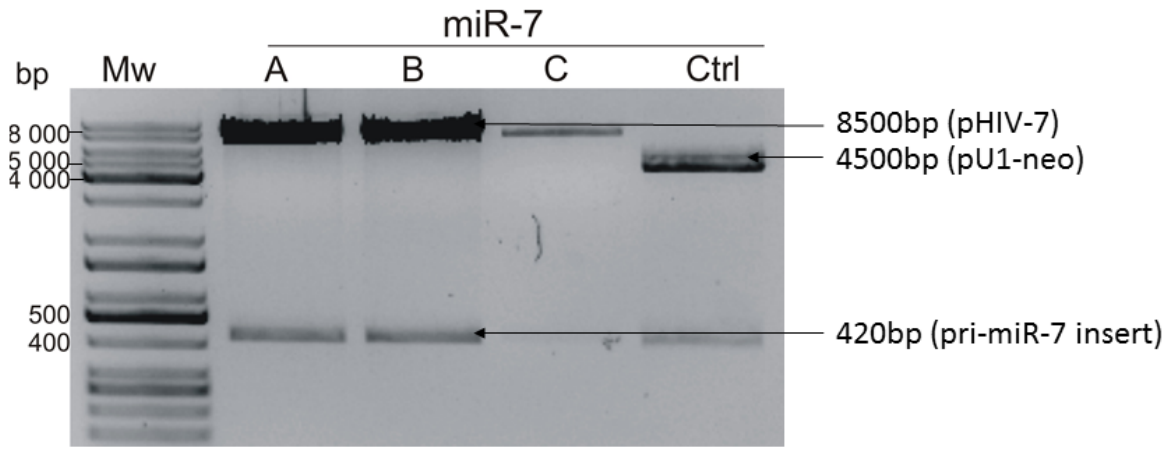


Figure 5.4: Gel electrophoresis to confirm successful cloning of U1-hsa-pri-miR-7 into pHIV backbone. Lanes A, B and C representing each of clones A, B and C, respectively, were digested with BamHI. In clones A and B, this generated an 8500 bp fragment (pHIV-7) and a 420 bp fragment (the pri-miR-7 insert). Previous round cloning of hsa-pri-miR-7 in the pU1-neo backbone (4500 bp) digested with NotI served as the control (Ctrl).

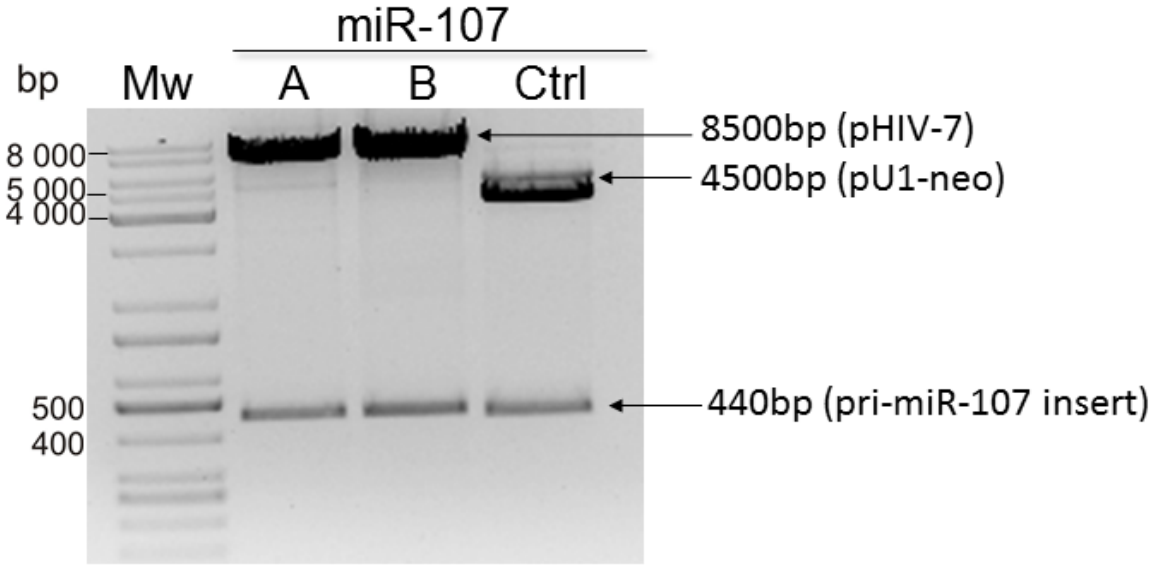


Figure 5.5: Gel electrophoresis to confirm successful cloning of U1-miR-107 into pHIV backbone. Lanes A and B representing each of clones A and B respectively, were digested with BamHI. In clones A and B, this generated an 8500 bp fragment (pHIV-7) and a 440 bp fragment (the pri-miR-107 insert). Previous round cloning of hsa-pri-miR-107 in the pU1 backbone digested with NotI served as the control (Ctrl).

5.3.2 Transduction efficiency of A549 non-CSCs

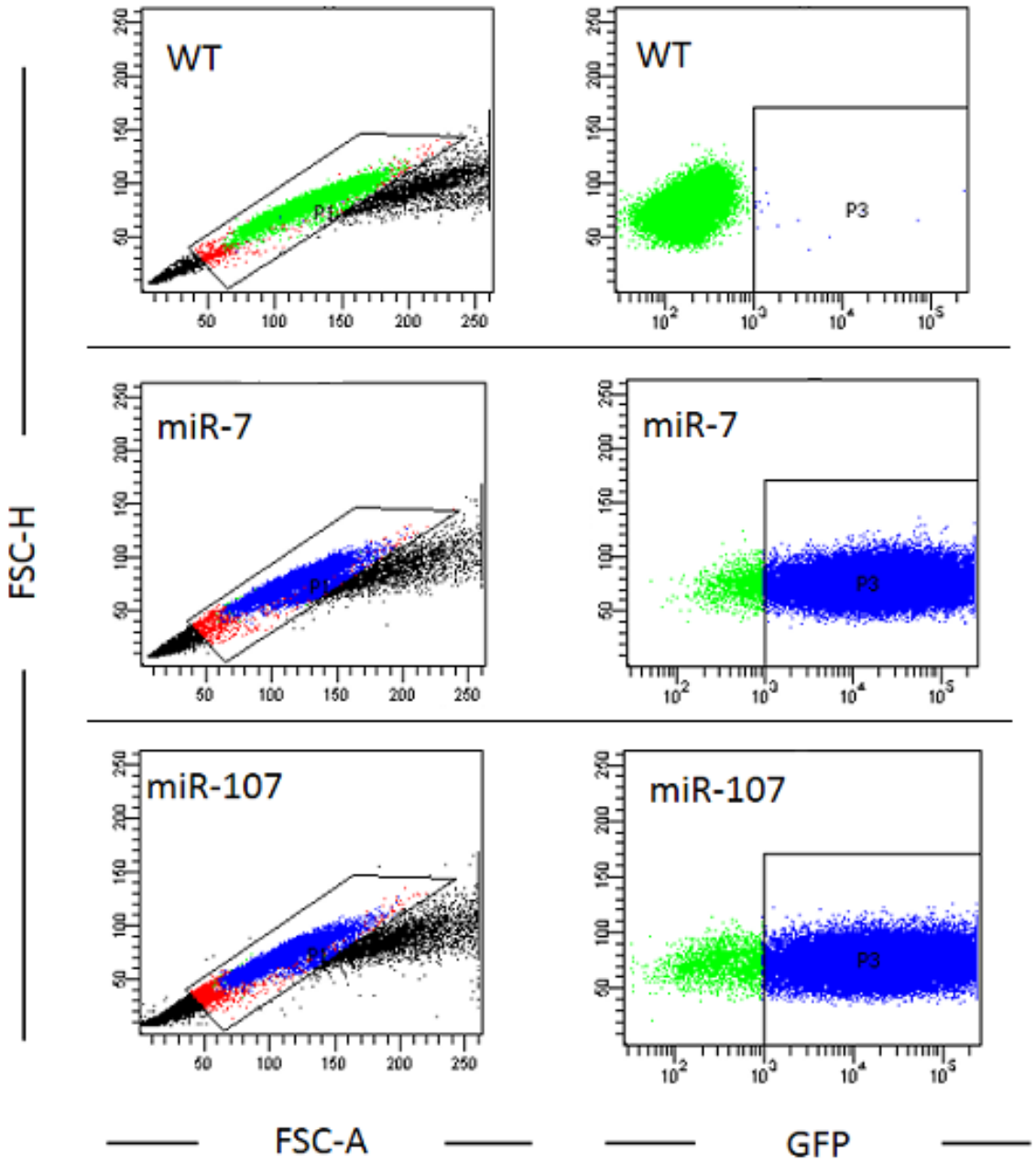


Figure 5.6: Dot plot of Forward Scatter Height (FSC-H) *versus* SSC-A (left) and GFP fluorescence (right) for A549 non-CSC WT, miR-7 and miR-107. 100 000 events were measured and gating was done to exclude doublets and GFP autofluorescence.

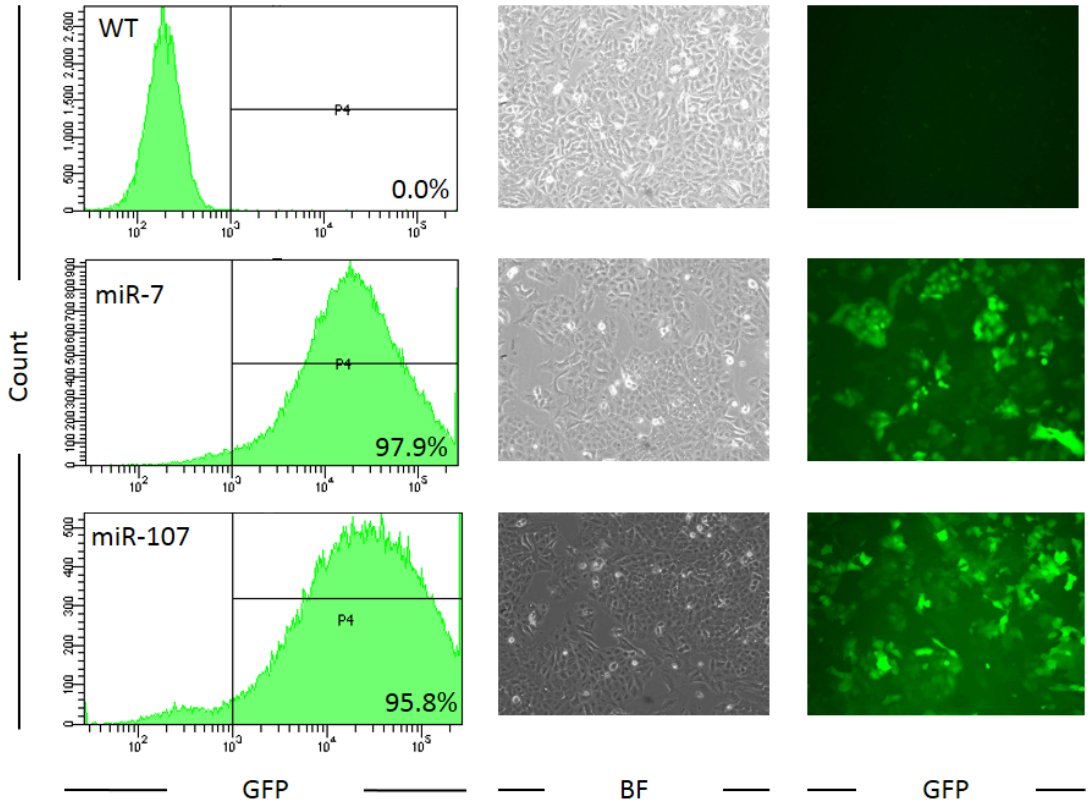


Figure 5.7: Dot plot of event count *versus* GFP fluorescence (left) and the corresponding BF images (middle) and GFP images at 100x magnification (right) for the WT (top) miR-7 (middle) and miR-107 (bottom) A549 non-CSCs. 100 000 events were measured and gating was done to exclude doublets and GFP autofluorescence.

5.3.3 Growth kinetics of A549 WT *vs* A549 miR-107 control

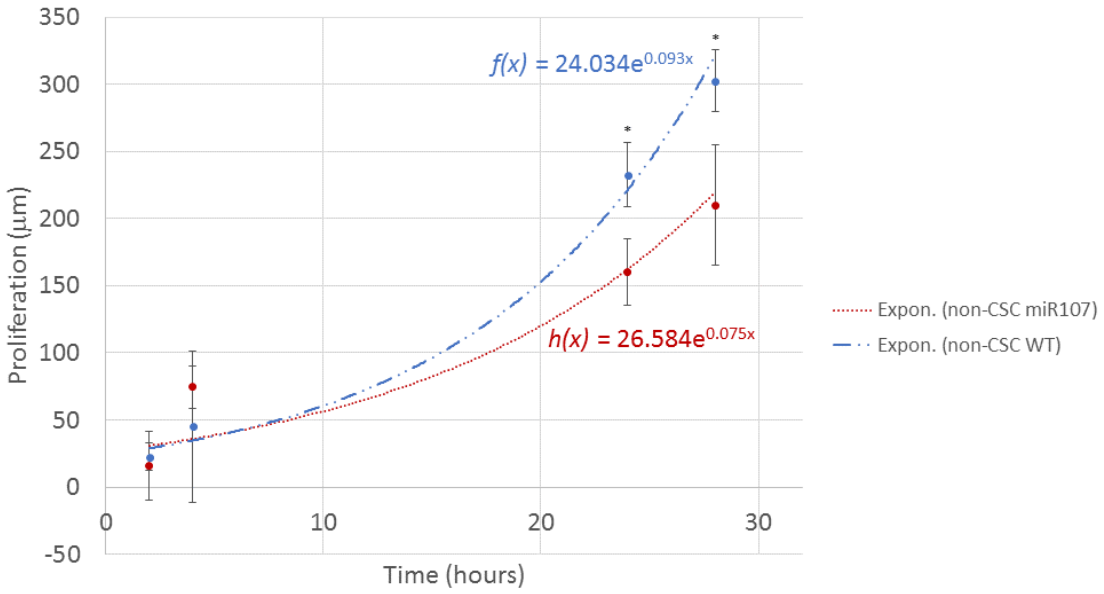


Figure 5.8: Proliferation (µm) of A549 non-CSC WT and non-CSC miR-107 control at 2 hours, 4 hours, 26 hours and 28 hours after scoring with a sterilised P200 pipette tip; P= 0.69, 0.43, 0.02 and 0.035, respectively. Images were captured using the Olympus IX71 inverted microscope with 40x magnification. Data are presented as the mean ±SD (*P<0.05).

Table 5.1: Calculated rate of proliferation (µm.h$^-$1) of WT CSC and WT non-CSCs using the exponential trendlines obtained in Fig.3.1

non-CSC	Proliferation (µm)	Growth rate (µm.h$^-$1)	Growth rate at 24 hours (µm.h$^-$1)
WT	$f(x) = 24.034e^{0.093x}$	$f'(x) = 2.235e^{0.093x}$	$f'(24) = 20.827$
miR-107	$h(x) = 26.584e^{0.075x}$	$h'(x) = 1.994e^{0.075x}$	$h'(24) = 12.06$

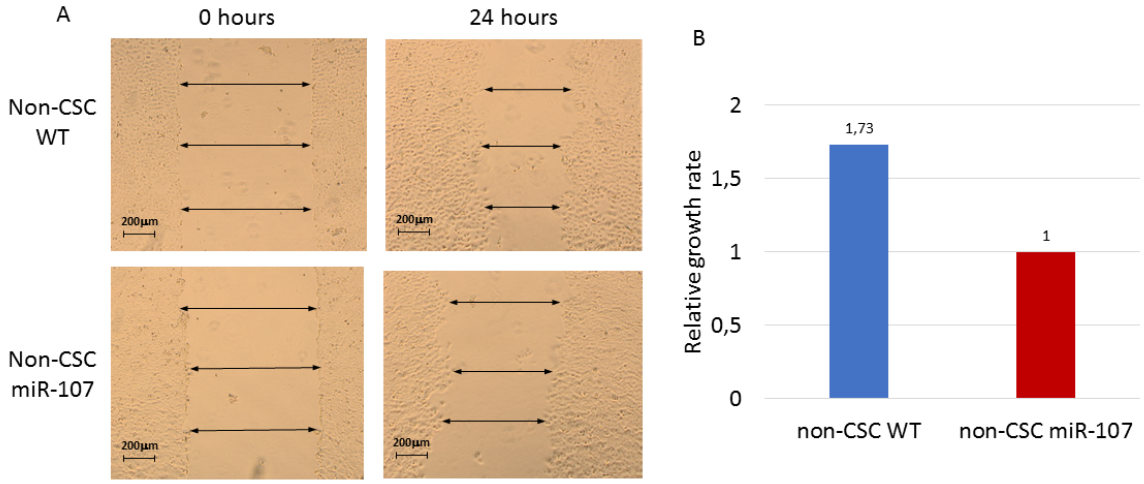


Figure 5.9: Comparison of growth rates of non-CSC WT and non-CSC transduced with miR-107. **(A)** Photomicrographs of non-CSC WT and non-CSC miR-107 at the time of the score with a P200 pipette (0 hour) and 24 hours afterwards (100 × magnification). **(B)** Relative growth rate of non-CSC WT and non-CSC miR-107 transduced cells. The non-CSC WT cells proliferated approximately 1.7 fold more than the non-CSC miR-107 cells.

5.3.4 Western blot Analysis

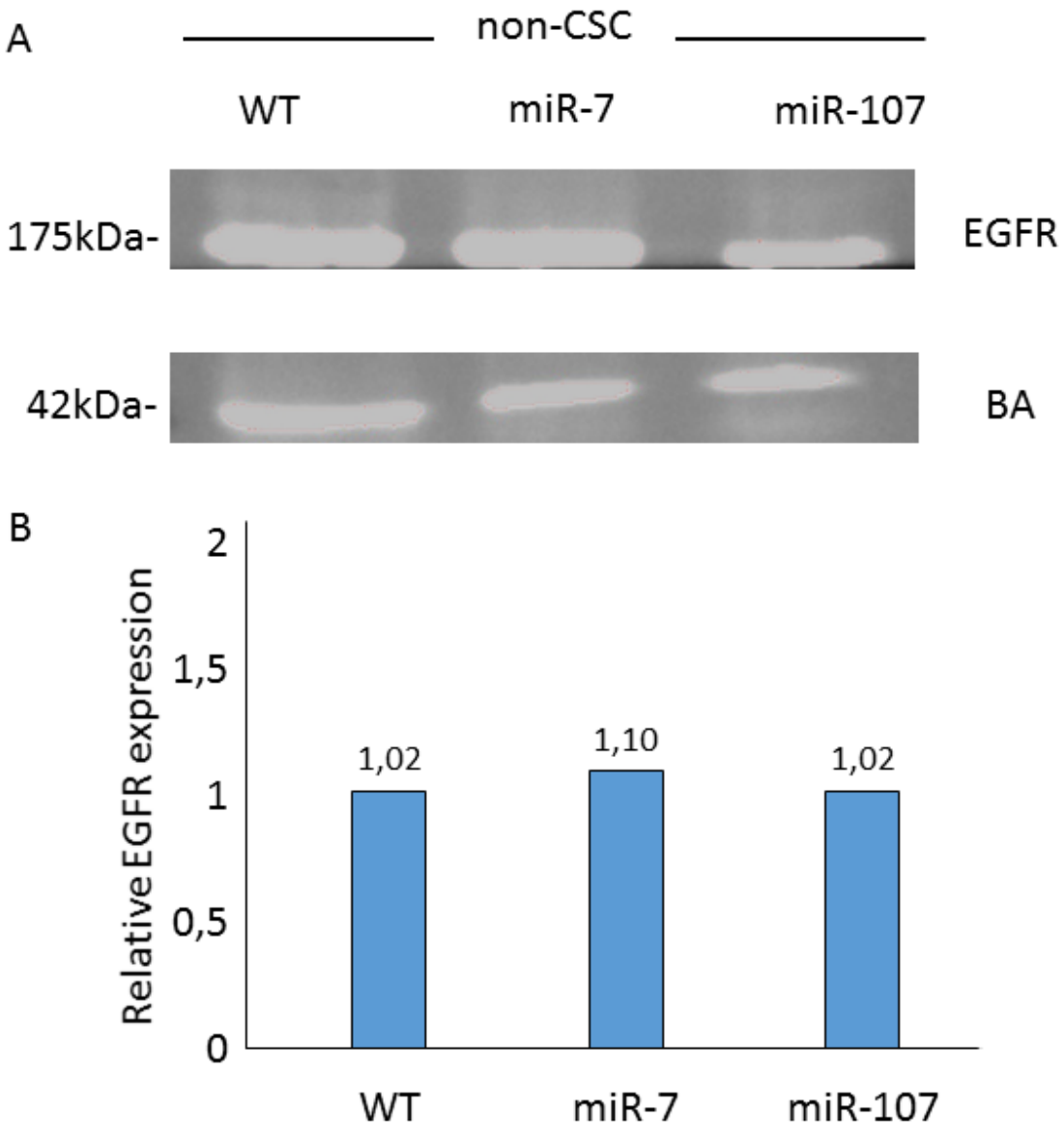


Figure 5.10: Western blotting results showing EGFR expression of non-CSCs WT, non-CSC miR-7 and non-CSC miR-107 transduced cells, with BA as a loading control. **(A)** Membrane exposed for 1.194 seconds in the Biorad Geldoc^{TM}after an overnight transfer and a 1:1000 primary EGFR (top) and 1:1000 primary BA antibody (bottom) incubated for 1 hour, respectively. Secondary antibody staining was performed with the Invitrogen WesternDot® 625 Western Blot Kit **(B)** EGFR intensity relative to BA control for non-CSC WT, non-CSC miR-7 and non-CSC miR-107 transduced control. The relative EGFR expression in non-CSC miR-7 was similar to the non-CSC WT and non-CSC miR-107 population.

5.3.5 Sequencing analysis

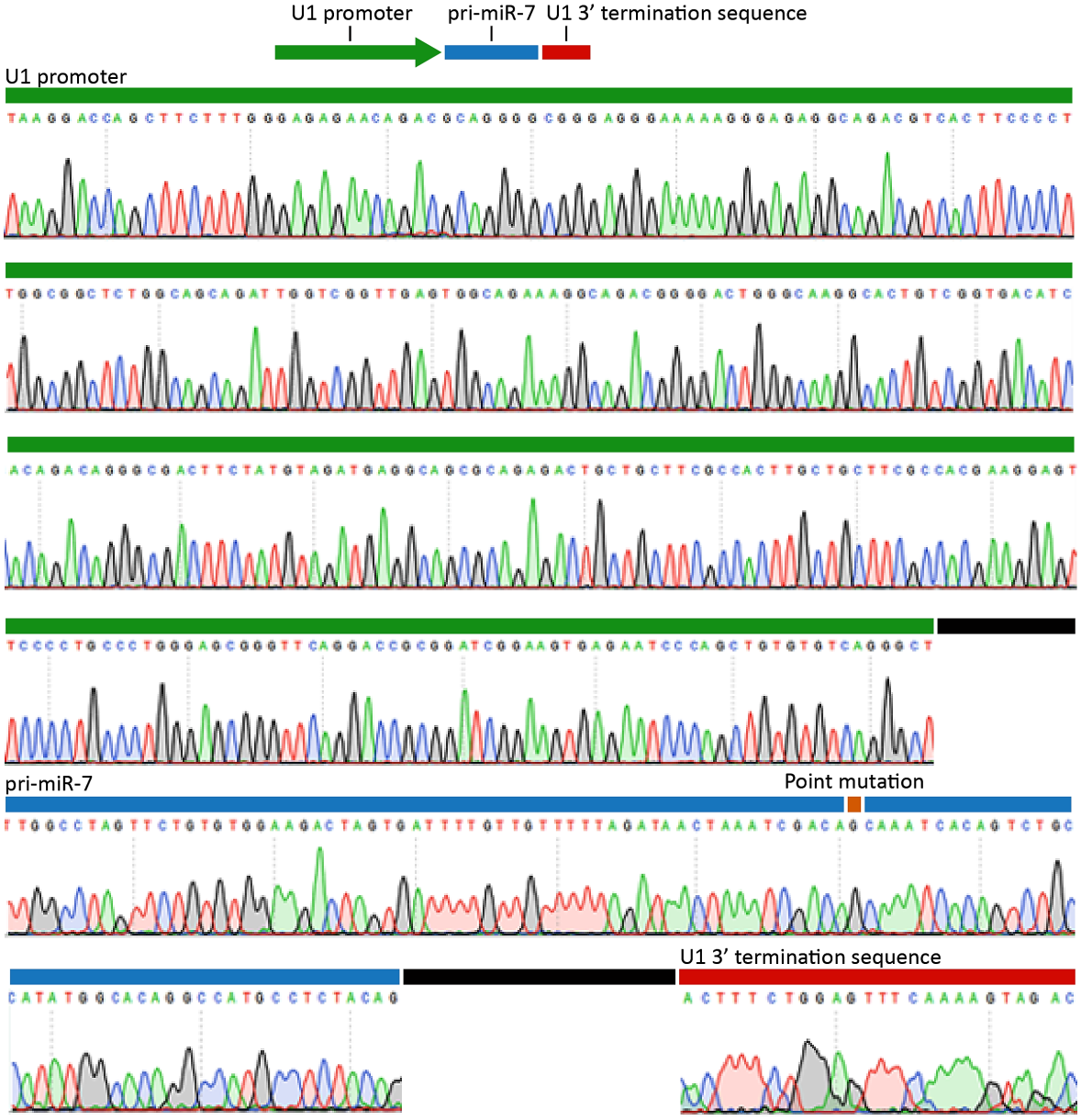


Figure 5.11: Electropherograms representing the sequencing results for pHIV-7-pri-miR-7 illustrating the U1 promoter sequence (green), the pri-miR-7 sequence (blue), as well as the U1' termination sequence (red) (performed by Inqaba Biotechnologies).

5.3.6 IF based comparison of EGFR fluorescence in miR-7 and miR-107 transduced cells

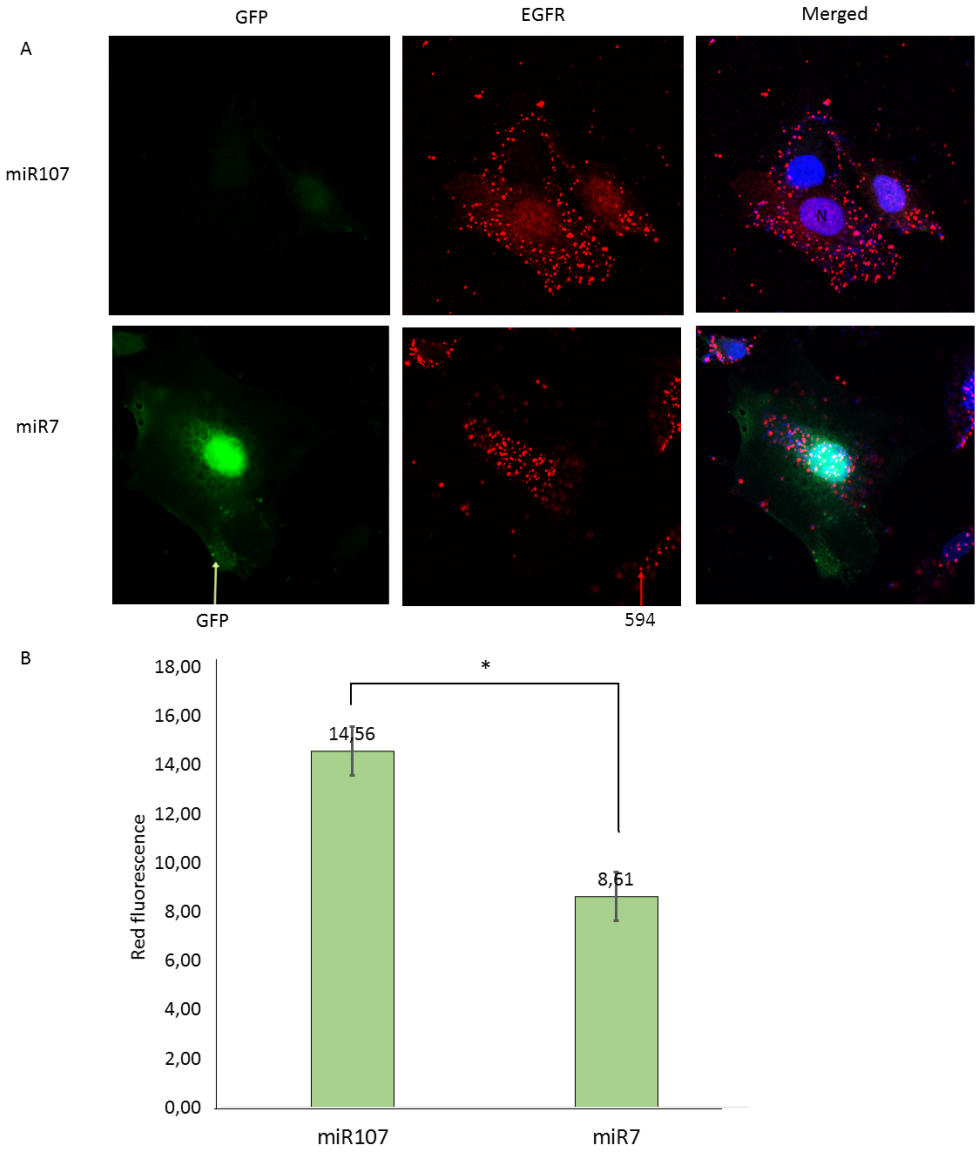


Figure 5.12: Immunofluorescence based comparison of EGFR expression in miR-107 and miR-7 transduced non-CSCs **(A)** Immunofluorescence staining depicting EGFR expression (red) in miR107 transduced non-CSCs (top panel) serving as the negative control for miR-7 transduced non-CSCs (bottom panel). miR-7 and miR-107 transduced cells show GFP fluorescence (green) (100x magnification) **(B)** Comparison of EGFR fluorescence in A549 miR7 and miR107 transduced cells following ImageJ analysis; P=0.00616. The miR-107 cells have a 1.7 fold increase in red fluorescence (EGFR), as compared to the miR-7 cells. Data represent measurements from biological triplicates and are presented as the mean ±SD (*P<0.01).

5.4 Discussion

5.4.1 Verification of pHIV-7-GFP plasmid containing U1-hsa-pri-miR-7 insert

The objective of the bacterial cloning was to ligate the hsa-pri-miR-7 construct downstream of the U1 promoter in pU1-neo. Second round cloning then involved ligating the U1-hsa-pri-miR-7 construct into the MCS of pHIV-7-GFP. The upper band of the second round clones A, B and C are approximately 7100bp, the size of pHIV-7-GFP when digested with BamHI. Thus, cloning was successful, as the U1-hsa-pri-miR-7 insert remains intact while being cloned into pHIV-7-GFP.

5.4.2 Transduction efficiency

Comparing the miR-7 and miR-107 transduced populations in Fig.5.6 to the untransduced control, the rightward shift indicates than the GFP fluorescence of the transduced populations was significantly higher than the untransduced control. By gating to include only the singlet population, the events counted represented single cells, wherein the transduction efficiency of the populations were 97% and 95% for the miR-7 and miR-107 transduced cells respectively, thus indicating successful transduction. The miR-7 transduced cell population had a wide range of fluorescence intensities compared with the control. This perhaps indicates that there is a varied production level of GFP within the population. This range could indicate that the copy number differs for the cells, and is not necessarily limited to one, the desired copy number. It can be deduced that there is varied expression of miR-7 within the transduced cells. Since the overall aim of the research is to investigate the effect of overexpression of miR-7 on A549 cells, having a higher copy number of miR-7 per cell still permits this to be determined.

5.4.3 Growth kinetics

Since the effect of miR-7 on proliferation is considered in Chapter 3, the effect of transduction on proliferation needs to be assessed to determine whether non-CSC WT can also serve as a negative control for proliferation, in addition to the miR-107 transduced non-CSC cells.

miR-107 transduced non-CSCs had a statistically significant lower proliferative ability com-

pared with the WT non-CSCs, at times 26 hours and 28 hours (P= 0.023 and 0.035, respectively) as seen in Fig.5.8. Through differentiation, and plotting of relative growth rate, it was found that the rate of growth of WT non-CSCs was 1.73 fold greater than that of the non-CSCs transduced with HIV-7-miR-107. These results make it clear that lentivirus transduction using HIV-7-miR-107 will have a significant effect on proliferation, even though miR-107 is not implicated to play a role in proliferation. As a result, any analysis of the effect of miR-7 transduction on proliferation will be compared to miR-107 transduced cells and not WT non-CSCs.

5.4.4 Knockdown efficiency

miR-7 mediated downregulation of EGFR was assessed through two techniques: Western Blotting and confocal microscopy. At a protein level, EGFR WB results also showed no difference between EGFR levels in the miR-7 transduced non-CSCs and the miR-107 transduced non-CSC negative control. Nevertheless, IF did show a difference in EGFR cellular localisation in the miR-7 transduced non-CSCs, compared to the miR-107 transduced control. ImageJ analysis of the IF images, showed EGFR expression to be lower in miR-7 cells compared with the miR-107 transduced negative control, Fig.5.12B (P=0.00616). The Western blotting and IF results found are discussed further below.

Results in Fig.5.10 show no qualitative, visible difference between EGFR expression in miR-7 transduced non-CSCs, when compared with the miR-107 transduced non-CSC negative control. IF shows a lower expression of EGFR in miR-7 transduced control compared with the negative control; however IF was analysed with ImageJ on a total of 18 cells per cell line. As this is not representative of the entire cell population the Western blotting results, performed on 1×10^6 cells per sample were used to confirm that no knockdown was achieved. Reasons for the lack of knockdown may be due to inefficient lentivirus miR-7 expression. It is possible that the expression of miR-7 failed to overcome negative feedback control to maintain EGFR expression.

The highly transduced population proved integration of GFP-U1-pri-miR-7 sequence into some 97.9% of the non-CSCs miR-7 population, (Fig.5.6, discussed in Section 5.4). The pHIV7-GFP-U1-pri-miR-7 plasmid is designed with the CMV promoter upstream of the GFP sequence and the U1 promoter upstream of the pri-miR-7 sequence. Although GFP fluorescence is observed in 97.9% of cells, the pri-miR-7 sequence is expressed from a different

promoter. Although GFP fluorescence confirms successful transduction, it cannot confirm successful expression of pri-miR-7. Confirmation of miR-7 expression could be done using Northern blotting. Explanations for the lack of efficient knockdown would need to consider the incubation time for the knockdown experiment, the promoter sequence, the miRNA form used and the miR-7 sequence. These factors are addressed below.

Incubation time for the knockdown experiment

It is important to take into account the half-life of EGFR itself, when analysing both the Western blotting and IF results. Sorkin and Duex (2010) found that the half-life of EGFR was approximately 8 to 24 hours through radiolabelling studies. Western blotting was performed approximately 5 days after seeding of transduced cells. During this time, the expression of miR-7 would allow for the downregulation of EGFR whilst EGFR expressed at the time of seeding would have been degraded. Since the half-life of EGFR was taken into account, it is unlikely that the incubation time is responsible for the lack of EGFR knockdown.

The U1 promoter

In the present study, a polymerase II dependent promoter was used for the expression of miR-7. Lee et al. (2004) reported that most miRNAs are expressed downstream of a polymerase II promoter, because many miRNAs have multiple consecutive Uracils which results in premature termination of transcription if dependent on polymerase III, as seen in hsa-pri-miR-7 (Appendix C.1.3). The efficiency of transcription for the CMV promoter was found to be the same as that for the UI promoter in a study by ter Brake et al. (2008). It can be deduced then that the efficiency of transcription in the non-CSCs transduced with hsa-pri-miR-7 should be the same as that from the CMV promoter, governing GFP expression in the constructs developed, at 97.9%.

U1 promoter expression can be unstable for a transcript without an open reading frame (Pinto et al., 2011). This may cause decreased intracellular miR-7 levels and could explain the lack of downregulation caused by miR-7 (seen in Fig.5.10). This said, many researchers have been able to downregulate EGFR with polymerase II dependent promoters in the NSCLC A549 cell line (Webster et al., 2009). The use of a TaqMan miRNA assay kit and a luciferase reporter assay would have been useful to determine whether miR-7 levels are increased in miR-7 transduced non-CSCs, to further understand the cause of the lack of EGFR knockdown.

Preferential cloning with pri-miR-7 over miR-7

NSCLC WT cells are able to cleave pri-miR-7 to form pre-miR-7 and subsequently miR-7, which then acts as a regulator of EGFR expression. The pri-miR-7 sequence was cloned downstream of the U1 in the pU1-neo plasmid, as pri-miRNA mediated gene silencing has proven far more effective than pre-miRNA or miRNA (Bielewicz et al., 2013). The hsa-pri-miR-7-1 sequence used was that identified by Landgraf et al. (2007) and is the most common form of miR-7 in mammalian studies. As the optimal form of miR-7 was used this is quite unlikely the cause for the lack of knockdown reported here.

U1-hsa-pri-miR-7 clone A sequence homology to hsa-pri-miR-7

The miR-7 sequence, and more specifically, the seed sequence showed 100% homology to the *Homo sapiens* miR-7-1 sequence. An A→G point mutation in the pri-miR-7 sequence was found, most likely obtained through PCR amplification of pri-miR-7 from the genome of HEK293 cells. That said, there is a possibility that the point mutation was present in the HEK293 genome itself. Mutations in miRNA sequences have been implicated in pathogenesis of cancer (Webster et al., 2009). Mutations in miR-7 can impact on its ability to downregulate EGFR. This may be responsible for the increased EGFR expression seen in some tumour types. Although the seed region is important for binding to 3'UTR of the target mRNA, transfection experiments with the miRNA sequence, or transduction with lentiviruses integrating the miR-7 sequence into the genome, have proven less effective than those that use pri-miRNAs. This indicates that the pri-miRNA and its sequence are important for the processing of miRNAs (Ryan et al., 2010).

miRNA studies using deep sequencing has shown that multiple variants of miRNAs can exist, some displaying variations in lengths, but others having point mutations. Research by Morin et al. (2008) demonstrated that the 5' end of pre-miRNAs, processed by Drosha, were far more conserved than 3' ends of pre-miRNA, cleaved by Dicer. The increased specificity of Drosha over Dicer has been hypothesised by Lewis et al. (2003) to be a result of the interaction between Drosha and DGCR8. Heterogeneity in the 5' sequences of miRNAs has been shown to affect the thermodynamic stability of miRNAs and determines which of the miRNA strands

will be incorporated into RISC. This can result in different mRNA targets. The 3' end of the pri-miRNA is thought to influence stability and localisation and may decrease the efficacy of mRNA targeting (Starega-Roslan et al., 2011b). The potential folding structure for hsa-pri-miR-7 mutant compared to hsa-pri-miR-7 WT is represented in Fig.5.13. The significance of the predicted structure is considered below.

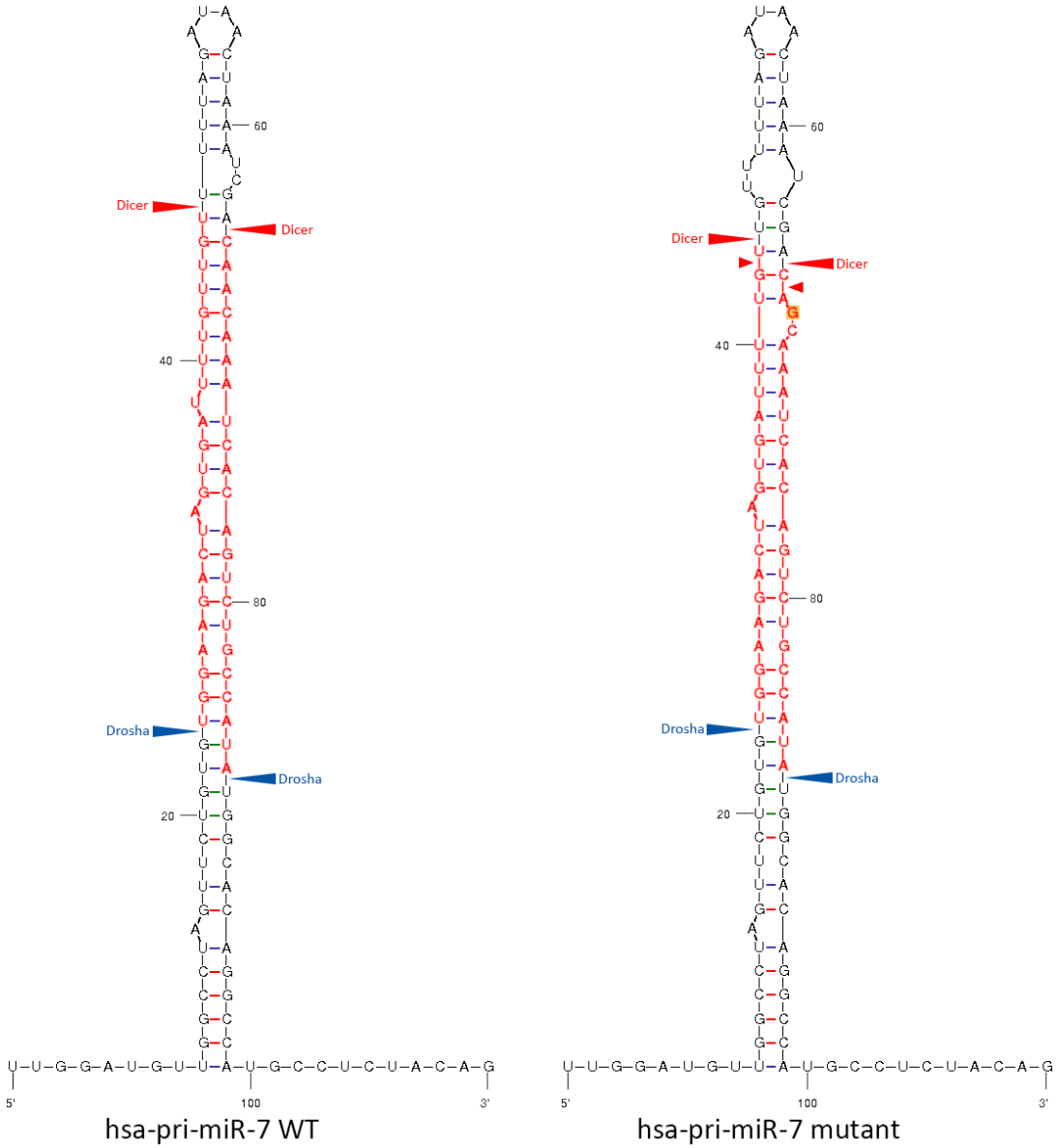


Figure 5.13: Comparison of hsa-pri-miR-7 and hsa-pri-miR-7 mutant predicted stem-loop structures using Quikfold. Structures shown include the miRNA sequence (red) and the Dicer (red arrows) and Drosha (blue arrows) cleavage sites. Mutant miR-7 will have additional Dicer cleavage sites indicated by the small red arrows.

Research by Zuker (2003) showed that mutations in the pre-miRNA affected the cleavage position of Dicer and resulted in longer miRNAs and the development of a 5' overhang rather than the usual 3' overhang. Only a few pre-miRNAs are shown to have perfectly paired stems and any unpaired nucleotides within the stem are hypothesised to bulge out of the helix and are not generally counted by Dicer when it determines its cleavage site, 22 nt from the 3' termini. This means that there is plasticity with the base sequence at the 3' end of the pre-miRNA (Starega-Roslan et al., 2011b). A seminal paper published by Starega-Roslan et al. (2015) further characterised Dicer cleavage. This research showed that in the absence of secondary structure (such as internal loops and bulges), Dicer produced miRNAs of various lengths. This finding showed that it is not only the distance from the 3' end that determines the cleavage site of Dicer. The bulges and internal loops are pre-miRNA structures important in cleavage of the miRNA. The sequence is integral to the formation of the secondary structures seen in miRNAs. Starega-Roslan et al. (2015) found that mutant miRNAs, with point mutations, contribute to the site at which Dicer cleaves the pre-miRNA. A change in the nucleotide sequence of Dicer resulted in a change in the final miRNA produced. This proves that Dicer cleavage is not solely dependent on distance from the 3' end. Further investigations showed that *G* residue in position A20 resulted in miRNA heterogeneity, with the generation of both 21 nt and 22 nt miRNA sequences, as indicated in Fig.5.13. The point mutation found in position A20 of the sequence (Fig.5.11), according to Starega-Roslan et al. (2015), would result in heterogeneity of the resulting miRNA product. Moreover, the different secondary structure of the mutant pri-miR-7 may also alter the heterogeneity of the miRNA product. Since no knockdown was observed in Fig.5.10, it can be hypothesised that heterogeneous miR-7 are produced with the miR-7 mutant transduced cells, which is not efficient enough to allow visible knockdown of EGFR to be observed.

5.4.5 Differential localisation of EGFR in miR-7 transduced cells

Starega-Roslan et al. (2015) showed that a *G* residue point mutation in position A20 resulted in some miRNA product heterogeneity. Some miRNA products were the normal 22 nt miRNA, whilst others were 21 nt in length and may have altered function in RISC. Applied to the mutant miRNA-7, it can be hypothesised that the production of some normal 22 nt miR-7 was however not enough to cause knockdown of EGFR. The differential localisation of EGFR to the nucleus when compared to the diffuse appearance of EGFR in the miR-107 transduced control,

indicates that the miR-7 mutant may affect nuclear-cytoplasmic shuttling of EGFR, but in the absence of a specific knockdown effect. This miR-7 mutant may be important since nuclear EGFR is associated with a poorer prognosis in many tumour types and has been shown to be responsible for resistance to Tyrosine Kinase Inhibitors, such as gefitinib (Wang and Hung, 2013).

The process through which EGFR is transported from the cell surface to the nucleus is poorly understood. What is known currently is that EGFR on the cell surface is internalised to the Golgi apparatus mediated by microtubules associated with dynein. EGFR is then transported to the endoplasmic reticulum (ER) through retrograde trafficking and from the ER, it localises to the inner nuclear membrane. The EGFR is then released from the internal nuclear membrane mediated by Sec61β after which EGFR can exert its functions in the nucleus (Wang and Hung, 2013). In tumour biology, increased internalisation of EGFR is seen, although the mechanism through which this occurs is yet to be understood.

Dysregulation of miRNAs was demonstrated by Croce (2009) to be a mechanism through which cancers develop. Wang and Hung (2013) subsequently showed that altered localisation of EGFR has been linked to the development of certain cancer types, such as oral cancers (Wang and Hung, 2013). Perhaps the nuclear localisation of EGFR as a result of the miR-7 mutant increase resistance of tumours to chemotherapy, through the transcriptional activation of genes such as DNA-dependent protein kinase (DDPK) and ABCG2. See details on ABCG2 in Chapters 2, 3 and 4. DNA repair is also thought to be mediated by nuclear EGFR's interaction with DDPK. It increases DDPK which repairs double strand breaks in DNA. Ryan et al. (2010) showed that many single nucleotide polymorphisms (SNPs) exist for known pri-miRNA sequences. Research by Webster et al. (2009) discovered that miRNAs are not conserved and deletions, mutations and rearrangements thereof are seen in tumour cells. Since miRNAs are heterogenous, it can then be hypothesised that the point mutation in this miR-7 may be present in some NSCLCs and thus could influence the increased nuclear EGFR expression. Raised nuclear EGFR mediates its effects as a transcription factor, to increase proteins such as ABCG2 so mediating chemoresistance (Wang and Hung, 2013).

5.5 Conclusion

Cloning, lentiviral transduction was successful in approximately 97.9% of the non-CSC population, indicated by the GFP fluorescence of cells. Western blotting showed no downregulation of EGFR expression mediated by the miR-7 insert, most likely due to the identified point mutation near the 3' end of the pri-miR-7 construct. The literature indicates that Dicer specificity at the 3' end is relatively low, and deep sequencing suggests that indicated miRNA sequences are highly heterogeneous. That said, a decreased efficiency of miRNA mediated knockdown has also been observed in miRNA mutants. Interestingly, the confocal microscopy image of miR-7 transduced cells shows differential nuclear localisation of EGFR in response to this mutant miR-7. Since Western blotting shows no downregulation of EGFR, it can be hypothesised that the mutant miR-7 did not effectively knockdown EGFR, but is responsible for the shuttling of EGFR to the nucleus. It is known that mutations of miRNAs are seen in tumour cells, and this particular miR-7 mutant may be responsible for nuclear localisation of EGFR, resulting in chemoresistance through mechanisms such as upregulating ABCG2.

CHAPTER 6

Final conclusion and future work

In summary, raised expression of the epidermal growth factor receptor (EGFR) would appear to be a central characteristic of the stem cells derived from the A549 NSCLC adenocarcinoma line. As elucidated in the present study, the stem cells expressed increased amounts of mRNA encoding for EGFR and this was reflected in raised amounts of EGFR detected subcellularly in these cells. Moreover, since the CSCs expressed elevated quantities of the ABCG2 drug transporter, this contributed to chemoresistance of these cells to Paclitaxel. The findings of the present study are diagrammatically summarised and integrated with relevant findings in the literature and the ''Hallmarks of Cancer' as described by Hanahan and Weinberg (2011).

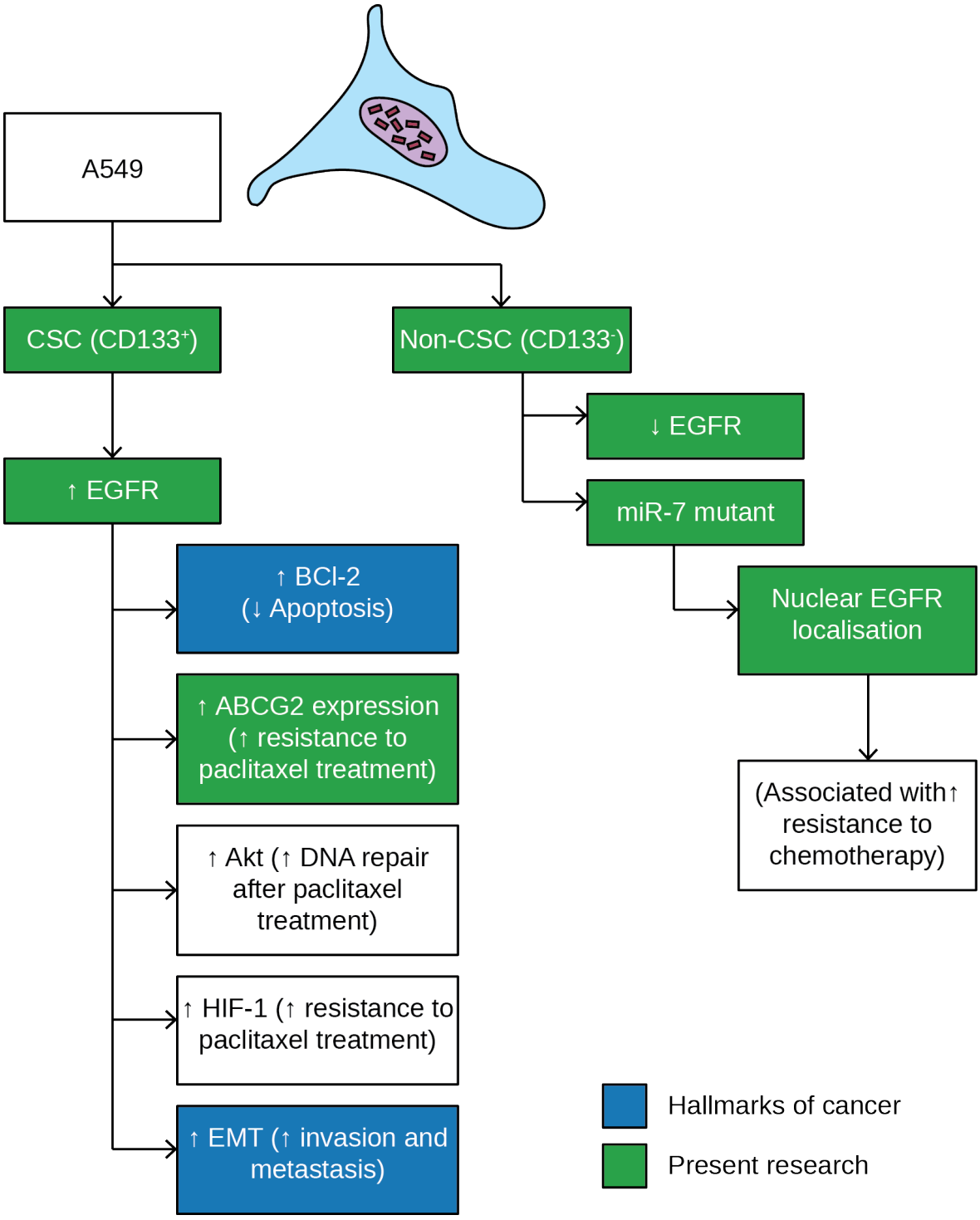


Figure 6.1: Summary of findings of the present study and the relationship of these to previous studies, including selected Hallmarks of Cancer.

6.1 Future work

The present work highlights some interesting comparisons between the tumorigenesis of CSCs and non-CSCs. It also describes the potential role of mi-7 in cancer as well as exploring the function point mutations have in the development of cancer. The work presented could be strengthened in a number of ways. The tumorigenesis of the CSCs and non-CSCs were compared using a Scratch Assay that quantifies motility. The spheroid nature of CSCs might indicate that a MTT or WST-1 assay may be more appropriate for this. Furthermore, measuring chemosensivity with the Annexin V assay would allow relative apoptosis of the CSCs and non-CSCs in response to Paclitaxel to be measured rather than using viability alone (Vermes et al., 1995). Further research with other miRNAs that do not affect migration should be performed. miR-107 has more recently been found to affect MCl-1 expression that in turn affects cellular proliferation (Zhou et al., 2014). Further studies using a scrambled sequence control should be implemented.

Currently, miRNAs are being investigated for their use as potential therapies for CSCs with many miRNAs being shown to increase chemosensitivity of CSCs to conventional treatments (Feng et al., 2015). miRNA-7 is being investigated for its ability to chemosensitise EGFR overexpressing tumours. Furthermore, research shows that mutant miRNAs may be responsible for increased expression of proteins implicated in the development of cancer (Lin and Gregory, 2015).

The research performed here shows that miR-7 mutant did not have the same knockdown ability as seen in miR-7 WT, as identified in previous research (Webster et al., 2009). This shows that the pri-miRNA sequence, and not just the miRNA sequence is important in the ability of miRNAs to knockdown their target mRNAs. Although seminal research has been performed in the importance of pri-miRNA sequences, most of the work has been done using Mfold or on other miRNAs, as reported in the paper by Starega-Roslan et al. (2015). Point mutations at different positions of miRNA-7 should be performed and characterised with Northern blotting for heterogeneity and efficiency of EGFR knockdown. According to Ryan et al. (2010), there is a large variation in pri-miRNA sequences due to SNPs. The research outlined in Chapter 5 shows that a single nucleotide change in the pri-miRNA-7 sequence may result in ineffective knockdown. Despite the ineffective knockdown, a change in the localisation of EGFR was found, which is hypothesised here to be EGFR acting as

a transcription factor to increase its own expression. Nuclear EGFR has also shown to be implicated in chemoresistance (Wang and Hung, 2013). Further research into SNPs present in NSCLC pri-miR-7 sequence would help identify miR-7 mutants, including the mutant clone in Chapter 5, that can be stably transduced and investigated *in vitro* for their effects on EGFR expression, their role in EGFR nuclear localisation and their effect on chemoresistance to conventional chemotherapy in NSCLC CSCs and non-CSCs. This will help identify possible SNPs in NSCLC that show ineffective knockdown of EGFR and may explain the EGFR overexpression in these NSCLC tumours. Furthermore, the role of miR-7 WT delivery, or silencing of mutant miR-7, as potential therapeutic options in these patients can be explored. Strengthening the methodologies for tumourigenesis would improve the robustness of the results. Relative motility of the CSCs and non-CSCs could be done using the WST-1 assay, as CSCs do not grow in a linear pattern and this analysis may have limited the ability to determine motility in CSCs.

References

Alamgeer, M., Ganju, V., and Watkins, D. N. (2013a). Novel therapeutic targets in non-small cell lung cancer. *Current Opinion in Pharmacology*, 13(3):394–401.

Alamgeer, M., Peacock, C. D., Matsui, W., Ganju, V., and Watkins, D. N. (2013b). Cancer stem cells in lung cancer: evidence and controversies. *Respirology*, 18(5):757–764.

Appert-Collin, A., Hubert, P., Crémel, G., and Bennasroune, A. (2015). Role of ErbB Receptors in Cancer Cell Migration and Invasion. *Frontiers in Pharmacology*, 6.

Banerji, A., Majumder, A., and Chatterjee, A. (2015). Stem Cells and Cancer: the Cancer Stem Cell (CSC) Model. *Journal of Tumor*, 3(3):349–355.

Barash, O., Peled, N., Tisch, U., Bunn, P. A., Hirsch, F. R., and Haick, H. (2012). Classification of lung cancer histology by gold nanoparticle sensors. *Nanomedicine: Nanotechnology, Biology and Medicine*, 8(5):580–589.

Barger, J. F. and Nana-Sinkam, S. P. (2015). MicroRNA as tools and therapeutics in lung cancer. *Respiratory Medicine*.

Beier, D., Hau, P., Proescholdt, M., Lohmeier, A., Wischhusen, J., Oefner, P. J., Aigner, L., Brawanski, A., Bogdahn, U., and Beier, C. P. (2007). CD133+ and CD133- glioblastoma-derived cancer stem cells show differential growth characteristics and molecular profiles. *Cancer Research*, 67(9):4010–4015.

Bertrand, G., Maalouf, M., Boivin, A., Battiston-Montagne, P., Beuve, M., Levy, A., Jalade, P., Fournier, C., Ardail, D., Magné, N., et al. (2014). Targeting head and neck cancer stem

cells to overcome resistance to photon and carbon ion radiation. *Stem Cell Reviews and Reports*, 10(1):114–126.

Bielewicz, D., Kalak, M., Kalyna, M., Windels, D., Barta, A., Vazquez, F., Szweykowska-Kulinska, Z., and Jarmolowski, A. (2013). Introns of plant pri-miRNAs enhance miRNA biogenesis. *EMBO Reports*, 14(7):622–628.

Buccheri, G., Ferrigno, D., and Tamburini, M. (1996). Karnofsky and ECOG performance status scoring in lung cancer: a prospective, longitudinal study of 536 patients from a single institution. *European Journal of Cancer*, 32(7):1135–1141.

Bustin, S. A., Benes, V., Garson, J. A., Hellemans, J., Huggett, J., Kubista, M., Mueller, R., Nolan, T., Pfaffl, M. W., Shipley, G. L., et al. (2009). The MIQE guidelines: minimum information for publication of quantitative real-time PCR experiments. *Clinical Chemistry*, 55(4):611–622.

Chen, G., Gharib, T. G., Huang, C.-C., Taylor, J. M., Misek, D. E., Kardia, S. L., Giordano, T. J., Iannettoni, M. D., Orringer, M. B., Hanash, S. M., et al. (2002). Discordant protein and mRNA expression in lung adenocarcinomas. *Molecular & Cellular Proteomics*, 1(4):304–313.

Chin, L., Andersen, J. N., and Futreal, P. A. (2011). Cancer genomics: from discovery science to personalized medicine. *Nature Medicine*, 17(3):297–303.

Croce, C. M. (2009). Causes and consequences of microRNA dysregulation in cancer. *Nature Reviews Genetics*, 10(10):704–714.

Diaz, A. and Leon, K. (2011). Therapeutic approaches to target cancer stem cells. *Cancers*, 3(3):3331–3352.

Ding, S., Li, C., Cheng, N., Cui, X., Xu, X., and Zhou, G. (2015). Redox Regulation in Cancer Stem Cells. *Oxidative Medicine and Cellular Longevity*.

Downward, J., Parker, P., and Waterfield, M. (1984). Autophosphorylation sites on the epidermal growth factor receptor. *Nature*, 311(5985):483–485.

Eyler, C. E., Foo, W.-C., LaFiura, K. M., McLendon, R. E., Hjelmeland, A. B., and Rich, J. N. (2008). Brain cancer stem cells display preferential sensitivity to Akt inhibition. *Stem Cells*, 26(12):3027–3036.

Feng, B., Zhang, K., Wang, R., and Chen, L. (2015). Non-small-cell lung cancer and miRNAs: novel biomarkers and promising tools for treatment. *Clinical Science*, 128(10):619–634.

Früh, M., De Ruysscher, D., Popat, S., Crinò, L., Peters, S., Felip, E., Group, E. G. W., et al. (2013). Small-cell lung cancer (SCLC): ESMO Clinical Practice Guidelines for diagnosis, treatment and follow-up. *Annals of Oncology*, page mdt178.

Gaber, R., Watermann, I., Kugler, C., Reinmuth, N., Huber, R. M., Schnabel, P. A., Vollmer, E., Reck, M., and Goldmann, T. (2014). Correlation of EGFR expression, gene copy number and clinicopathological status in NSCLC. *Diagnostic Pathology*, 9(1):1–15.

Garzon, R., Marcucci, G., and Croce, C. M. (2010). Targeting microRNAs in cancer: rationale, strategies and challenges. *Nature Reviews Drug Discovery*, 9(10):775–789.

Giard, D. J., Aaronson, S. A., Todaro, G. J., Arnstein, P., Kersey, J. H., Dosik, H., and Parks, W. P. (1973). In vitro cultivation of human tumors: establishment of cell lines derived from a series of solid tumors. *Journal of the National Cancer Institute*, 51(5):1417–1423.

Goodell, M. A., Brose, K., Paradis, G., Conner, A. S., and Mulligan, R. C. (1996). Isolation and functional properties of murine hematopoietic stem cells that are replicating in vivo. *The Journal of Experimental Medicine*, 183(4):1797–1806.

Gottschling, S., Schnabel, P. A., Herth, F. J., and Herpel, E. (2012). Are we Missing the Target?–Cancer Stem Cells and Drug Resistance in Non-small Cell Lung Cancer. *Cancer Genomics-Proteomics*, 9(5):275–286.

Hanahan, D. and Weinberg, R. A. (2011). Hallmarks of cancer: the next generation. *Cell*, 144(5):646–674.

Harper, L. J., Costea, D. E., Gammon, L., Fazil, B., Biddle, A., and Mackenzie, I. C. (2010). Normal and malignant epithelial cells with stem-like properties have an extended G2 cell cycle phase that is associated with apoptotic resistance. *BMC Cancer*, 10(1):166.

Hellemans, J., Mortier, G., De Paepe, A., Speleman, F., and Vandesompele, J. (2007). qBase relative quantification framework and software for management and automated analysis of real-time quantitative PCR data. *Genome Biology*, 8(2):R19.

Hilbe, W., Dirnhofer, S., Oberwasserlechner, F., Schmid, T., Gunsilius, E., Hilbe, G., Wöll, E., and Kähler, C. (2004). CD133 positive endothelial progenitor cells contribute to the tumour vasculature in non-small cell lung cancer. *Journal of Clinical Pathology*, 57(9):965–969.

Hirsch, F., Varella-Garcia, M., and Cappuzzo, F. (2009). Predictive value of EGFR and HER2 overexpression in advanced non-small-cell lung cancer. *Oncogene*, 28:S32–S37.

Ho, M. M., Ng, A. V., Lam, S., and Hung, J. Y. (2007). Side population in human lung cancer cell lines and tumors is enriched with stem-like cancer cells. *Cancer Research*, 67(10):4827–4833.

Horst, D., Kriegl, L., Engel, J., Kirchner, T., and Jung, A. (2008). CD133 expression is an independent prognostic marker for low survival in colorectal cancer. *British Journal of Cancer*, 99(8):1285–1289.

Hu, B., Emdad, L., Bacolod, M. D., Kegelman, T. P., Shen, X.-N., Alzubi, M. A., Das, S. K., Sarkar, D., and Fisher, P. B. (2014). Astrocyte Elevated Gene-1 Interacts with Akt Isoform 2 to Control Glioma Growth, Survival, and Pathogenesis. *Cancer Research*, 74(24):7321–7332.

Jemal, A., Siegel, R., Ward, E., Hao, Y., Xu, J., and Thun, M. J. (2009). Cancer statistics, 2009. *CA: a cancer journal for clinicians*, 59(4):225–249.

Johnson, M. L., Sima, C. S., Chaft, J., Paik, P. K., Pao, W., Kris, M. G., Ladanyi, M., and Riely, G. J. (2013). Association of KRAS and EGFR mutations with survival in patients with advanced lung adenocarcinomas. *Cancer*, 119(2):356–362.

Johnston, J. B., Navaratnam, S., Pitz, M. W., Maniate, J. M., Wiechec, E., Baust, H., Gingerich, J., Skliris, G. P., Murphy, L. C., and Los, M. (2006). Targeting the EGFR pathway for cancer therapy. *Current Medicinal Chemistry*, 13(29):3483–3492.

Kerr, K., Bubendorf, L., Edelman, M., Marchetti, A., Mok, T., Novello, S., O'Byrne, K., Stahel, R., Peters, S., Felip, E., et al. (2014). Second ESMO consensus conference on lung cancer: pathology and molecular biomarkers for non-small-cell lung cancer. *Annals of Oncology*, 25(9):1681–1690.

Khan, I. S. and Ehtesham, M. (2015). Emerging Strategies for the Treatment of Tumor Stem Cells in Central Nervous System Malignancies. In *Stem Cell Biology in Neoplasms of the Central Nervous System*, pages 167–187. Springer.

Kim, E.-H., Min, H.-Y., Chung, H.-J., Song, J., Park, H.-J., Kim, S., and Lee, S. K. (2012a). Anti-proliferative activity and suppression of P-glycoprotein by (-)-antofine, a natural

phenanthroindolizidine alkaloid, in paclitaxel-resistant human lung cancer cells. *Food and Chemical Toxicology*, 50(3):1060–1065.

Kim, J., Jung, J., Lee, S.-J., Lee, J.-S., and Park, M.-J. (2012b). Cancer stem-like cells persist in established cell lines through autocrine activation of EGFR signaling. *Oncology Letters*, 3(3):607–612.

Kobayashi, C. I. and Suda, T. (2012). Regulation of reactive oxygen species in stem cells and cancer stem cells. *Journal of Cellular Physiology*, 227(2):421–430.

Kris, M. G., Johnson, B. E., Berry, L. D., Kwiatkowski, D. J., Iafrate, A. J., Wistuba, I. I., Varella-Garcia, M., Franklin, W. A., Aronson, S. L., Su, P.-F., et al. (2014). Using multiplexed assays of oncogenic drivers in lung cancers to select targeted drugs. *JAMA*, 311(19):1998–2006.

Lai, E. C. (2015). Two decades of miRNA biology: lessons and challenges. *RNA*, 21(4):675–677.

Landgraf, P., Rusu, M., Sheridan, R., Sewer, A., Iovino, N., Aravin, A., Pfeffer, S., Rice, A., Kamphorst, A. O., Landthaler, M., et al. (2007). A mammalian microRNA expression atlas based on small RNA library sequencing. *Cell*, 129(7):1401–1414.

Langer, C., Hirsh, V., Okamoto, I., Lin, F., Wan, Y., Whiting, S., Ong, T., Renschler, M., and Botteman, M. (2015). Survival, quality-adjusted survival, and other clinical end points in older advanced non-small-cell lung cancer patients treated with albumin-bound paclitaxel. *British Journal of Cancer*, 113(1):20–29.

Lee, K. M., Choi, E. J., and Kim, I. A. (2011). microRNA-7 increases radiosensitivity of human cancer cells with activated EGFR-associated signaling. *Radiotherapy and Oncology*, 101(1):171–176.

Lee, R. C., Feinbaum, R. L., and Ambros, V. (1993). The C. elegans heterochronic gene lin-4 encodes small RNAs with antisense complementarity to lin-14. *Cell*, 75(5):843–854.

Lee, Y., Kim, M., Han, J., Yeom, K.-H., Lee, S., Baek, S. H., and Kim, V. N. (2004). MicroRNA genes are transcribed by RNA polymerase II. *The EMBO Journal*, 23(20):4051–4060.

Lewis, B. P., Shih, I.-h., Jones-Rhoades, M. W., Bartel, D. P., and Burge, C. B. (2003). Prediction of mammalian microRNA targets. *Cell*, 115(7):787–798.

Li, Z., Wang, H., Eyler, C. E., Hjelmeland, A. B., and Rich, J. N. (2009). Turning cancer stem cells inside out: an exploration of glioma stem cell signaling pathways. *Journal of Biological Chemistry*, 284(25):16705–16709.

Lim, L. P., Glasner, M. E., Yekta, S., Burge, C. B., and Bartel, D. P. (2003). Vertebrate microRNA genes. *Science*, 299(5612):1540–1540.

Lin, S. and Gregory, R. I. (2015). MicroRNA biogenesis pathways in cancer. *Nature Reviews Cancer*, 15(6):321–333.

Liu, R., Liu, X., Zheng, Y., Gu, J., Xiong, S., Jiang, P., Jiang, X., Huang, E., Yang, Y., Ge, D., et al. (2014). MicroRNA-7 sensitizes non-small cell lung cancer cells to paclitaxel. *Oncology Letters*, 8(5):2193–2200.

Liu, X.-J., Wu, W.-T., Wu, W.-H., Yin, F., Ma, S.-H., Qin, J.-Z., Liu, X.-X., Liu, Y.-N., Zhang, X.-Y., Li, P., et al. (2013). A Minority Subpopulation of CD133+/EGFRvIII+/EGFR- Cells Acquires Stemness and Contributes to Gefitinib Resistance. *CNS Neuroscience and Therapeutics*, 19(7):494–502.

Mallini, P., Lennard, T., Kirby, J., and Meeson, A. (2014). Epithelial-to-mesenchymal transition: what is the impact on breast cancer stem cells and drug resistance. *Cancer Treatment Reviews*, 40(3):341–348.

Mehra, A., Lee, K. H., and Hatzimanikatis, V. (2003). Insights into the relation between mRNA and protein expression patterns: I. Theoretical considerations. *Biotechnology and Bioengineering*, 84(7):822–833.

Meng, X., Li, M., Wang, X., Wang, Y., and Ma, D. (2009). Both CD133+ and CD133- subpopulations of A549 and H446 cells contain cancer-initiating cells. *Cancer Science*, 100(6):1040–1046.

Miller, Y. E. (2005). Pathogenesis of lung cancer: 100 year report. *American Journal of Respiratory Cell and Molecular Biology*, 33(3):216.

Miqueli, A. D., Rolff, J., Lemm, M., Fichtner, I., Perez, R., and Montero, E. (2009). Radiosensitisation of U87MG brain tumours by anti-epidermal growth factor receptor monoclonal antibodies. *British Journal of Cancer*, 100(6):950–958.

Morin, R. D., O'Connor, M. D., Griffith, M., Kuchenbauer, F., Delaney, A., Prabhu, A.-L., Zhao, Y., McDonald, H., Zeng, T., Hirst, M., et al. (2008). Application of massively parallel

sequencing to microRNA profiling and discovery in human embryonic stem cells. *Genome Research*, 18(4):610–621.

Morrison, R., Schleicher, S. M., Sun, Y., Niermann, K. J., Kim, S., Spratt, D. E., Chung, C. H., and Lu, B. (2010). Targeting the mechanisms of resistance to chemotherapy and radiotherapy with the cancer stem cell hypothesis. *Journal of Oncology*, 2011.

Nakada, M., Kita, D., Teng, L., Pyko, I. V., Watanabe, T., Hayashi, Y., and Hamada, J.-i. (2013). Receptor tyrosine kinases: principles and functions in glioma invasion. In *Glioma Signaling*, pages 143–170. Springer Netherlands.

Nguyen, L. V., Vanner, R., Dirks, P., and Eaves, C. J. (2012). Cancer stem cells: an evolving concept. *Nature Reviews Cancer*, 12(2):133–143.

O'Byrne, K. J., Gatzemeier, U., Bondarenko, I., Barrios, C., Eschbach, C., Martens, U. M., Hotko, Y., Kortsik, C., Paz-Ares, L., Pereira, J. R., et al. (2011). Molecular biomarkers in non-small-cell lung cancer: a retrospective analysis of data from the phase 3 FLEX study. *The Lancet Oncology*, 12(8):795–805.

Oda, K., Matsuoka, Y., Funahashi, A., and Kitano, H. (2005). A comprehensive pathway map of epidermal growth factor receptor signaling. *Molecular Systems Biology*, 1(1).

Pao, W. and Girard, N. (2011). New driver mutations in non-small-cell lung cancer. *The Lancet Oncology*, 12(2):175–180.

Pastò, A., Amadori, A., and Indraccolo, S. (2012). Signaling Pathways in Cancer Stem Cells: Therapeutic Implications. In *Stem Cells and Cancer Stem Cells, Volume 5*, pages 3–11. Springer.

Peichev, M., Naiyer, A. J., Pereira, D., Zhu, Z., Lane, W. J., Williams, M., Oz, M. C., Hicklin, D. J., Witte, L., Moore, M. A., et al. (2000). Expression of VEGFR-2 and AC133 by circulating human CD34+ cells identifies a population of functional endothelial precursors. *Blood*, 95(3):952–958.

Pinto, P. A., Henriques, T., Freitas, M. O., Martins, T., Domingues, R. G., Wyrzykowska, P. S., Coelho, P. A., Carmo, A. M., Sunkel, C. E., Proudfoot, N. J., et al. (2011). RNA polymerase II kinetics in polo polyadenylation signal selection. *The EMBO Journal*, 30(12):2431–2444.

Qu, H., Li, R., Liu, Z., Zhang, J., and Luo, R. (2013). Prognostic value of cancer stem cell marker CD133 expression in non-small cell lung cancer: a systematic review. *International Journal of Clinical and Experimental Pathology*, 6(11):2644.

Rami-Porta, R., Bolejack, V., Crowley, J., Ball, D., Kim, J., Lyons, G., Rice, T., Suzuki, K., Thomas, C. F., Travis, W. D., et al. (2015). The IASLC Lung Cancer Staging Project: proposals for the revisions of the T descriptors in the forthcoming eighth edition of the TNM Classification for Lung Cancer. *Journal of Thoracic Oncology*, 10(7):990–1003.

Richardson, G. D., Robson, C. N., Lang, S. H., Neal, D. E., Maitland, N. J., and Collins, A. T. (2004). CD133, a novel marker for human prostatic epithelial stem cells. *Journal of Cell Science*, 117(16):3539–3545.

Ryan, B. M., Robles, A. I., and Harris, C. C. (2010). Genetic variation in microRNA networks: the implications for cancer research. *Nature Reviews Cancer*, 10(6):389–402.

Salcido, C., Larochelle, A., Taylor, B., Dunbar, C., and Varticovski, L. (2010). Molecular characterisation of side population cells with cancer stem cell-like characteristics in small-cell lung cancer. *British Journal of Cancer*, 102(11):1636–1644.

Salnikov, A. V., Gladkich, J., Moldenhauer, G., Volm, M., Mattern, J., and Herr, I. (2010). CD133 is indicative for a resistance phenotype but does not represent a prognostic marker for survival of non-small cell lung cancer patients. *International Journal of Cancer*, 126(4):950–958.

Sarkadi, B., Özvegy-Laczka, C., Német, K., and Váradi, A. (2004). ABCG2–a transporter for all seasons. *FEBS Letters*, 567(1):116–120.

Shi, Y., Au, J. S.-K., Thongprasert, S., Srinivasan, S., Tsai, C.-M., Khoa, M. T., Heeroma, K., Itoh, Y., Cornelio, G., and Yang, P.-C. (2014). A prospective, molecular epidemiology study of EGFR mutations in Asian patients with advanced non–small-cell lung cancer of adenocarcinoma histology (PIONEER). *Journal of Thoracic Oncology*, 9(2):154.

Shimono, Y., Mukohyama, J., Nakamura, S.-i., and Minami, H. (2015). MicroRNA Regulation of Human Breast Cancer Stem Cells. *Journal of Clinical Medicine*, 5(1):2.

Siegel, R. L., Miller, K. D., and Jemal, A. (2015). Cancer statistics, 2015. *CA: a Cancer Journal for Clinicians*, 65(1):5–29.

Silvestri, G. A., Tanoue, L. T., Margolis, M. L., Barker, J., and Detterbeck, F. (2003). The noninvasive staging of non-small cell lung cancer: the guidelines. *CHEST Journal*, 123(1_suppl):147S–156S.

Singh, S., Trevino, J., Bora-Singhal, N., Coppola, D., Haura, E., Altiok, S., and Chellappan, S. P. (2012). EGFR/Src/Akt signaling modulates Sox2 expression and self-renewal of stem-like side-population cells in non-small cell lung cancer. *Molecular Cancer*, 11(1):73.

Singh, S. K., Hawkins, C., Clarke, I. D., Squire, J. A., Bayani, J., Hide, T., Henkelman, R. M., Cusimano, M. D., and Dirks, P. B. (2004). Identification of human brain tumour initiating cells. *Nature*, 432(7015):396–401.

Soeda, A., Inagaki, A., Oka, N., Ikegame, Y., Aoki, H., Yoshimura, S.-i., Nakashima, S., Kunisada, T., and Iwama, T. (2008). Epidermal growth factor plays a crucial role in mitogenic regulation of human brain tumor stem cells. *Journal of Biological Chemistry*, 283(16):10958–10966.

Sorkin, A. and Duex, J. E. (2010). Quantitative analysis of endocytosis and turnover of epidermal growth factor (EGF) and EGF receptor. *Current Protocols in Cell Biology*, pages 15–14.

Starega-Roslan, J., Galka-Marciniak, P., and Krzyzosiak, W. J. (2015). Nucleotide sequence of miRNA precursor contributes to cleavage site selection by Dicer. *Nucleic Acids Research*, 43(22):10939–10951.

Starega-Roslan, J., Koscianska, E., Kozlowski, P., and Krzyzosiak, W. J. (2011a). The role of the precursor structure in the biogenesis of microRNA. *Cellular and Molecular Life Sciences*, 68(17):2859–2871.

Starega-Roslan, J., Krol, J., Koscianska, E., Kozlowski, P., Szlachcic, W. J., Sobczak, K., and Krzyzosiak, W. J. (2011b). Structural basis of microRNA length variety. *Nucleic Acids Research*, 39(1):257–268.

Steinmetz, N. F., Maurer, J., Sheng, H., Bensussan, A., Maricic, I., Kumar, V., and Braciak, T. A. (2011). Two domains of vimentin Are expressed on the surface of lymph node, bone and brain metastatic prostate cancer lines along with the putative stem cell marker proteins CD44 and CD133. *Cancers*, 3(3):2870–2885.

Stoltz, K., Sinyuk, M., Hale, J. S., Wu, Q., Otvos, B., Walker, K., Vasanji, A., Rich, J. N., Hjelmeland, A. B., and Lathia, J. D. (2015). Development of a Sox2 reporter system modeling cellular heterogeneity in glioma. *Neuro-oncology*, 17(3):361–371.

Su, Z., Yin, J., Zhao, L., Li, R., Liang, H., Zhang, J., and Wang, K. (2014). Lentiviral vector-mediated RBM5 overexpression downregulates EGFR expression in human non-small cell lung cancer cells. *World Journal of Surgical Oncology*, 12(1):1–9.

Templeton, A. K., Miyamoto, S., Babu, A., Munshi, A., and Ramesh, R. (2014). Cancer stem cells: progress and challenges in lung cancer. *Stem Cell Investigation*, 1:9.

ter Brake, O., Liu, Y. P., Centlivre, M., von Eije, K. J., Berkhout, B., et al. (2008). Lentiviral vector design for multiple shRNA expression and durable HIV-1 inhibition. *Molecular Therapy*, 16(3):557–564.

Tirino, V., Camerlingo, R., Franco, R., Malanga, D., La Rocca, A., Viglietto, G., Rocco, G., and Pirozzi, G. (2009). The role of CD133 in the identification and characterisation of tumour-initiating cells in non-small-cell lung cancer. *European Journal of Cardio-Thoracic Surgery*, 36(3):446–453.

Veldhoen, R., Banman, S., Hemmerling, D., Odsen, R., Simmen, T., Simmonds, A., Underhill, D., and Goping, I. (2013). The chemotherapeutic agent paclitaxel inhibits autophagy through two distinct mechanisms that regulate apoptosis. *Oncogene*, 32(6):736–746.

Vermes, I., Haanen, C., Steffens-Nakken, H., and Reutellingsperger, C. (1995). A novel assay for apoptosis flow cytometric detection of phosphatidylserine expression on early apoptotic cells using fluorescein labelled annexin V. *Journal of immunological methods*, 184(1):39–51.

Wang, Y.-N. and Hung, M.-C. (2013). Nuclear localization of receptor tyrosine kinases in cancers. *Biohelikon Cancer and Clinical Research*, 1.

Webster, R. J., Giles, K. M., Price, K. J., Zhang, P. M., Mattick, J. S., and Leedman, P. J. (2009). Regulation of epidermal growth factor receptor signaling in human cancer cells by microRNA-7. *Journal of Biological Chemistry*, 284(9):5731–5741.

Welm, B. E., Dijkgraaf, G. J., Bledau, A. S., Welm, A. L., and Werb, Z. (2008). Lentiviral transduction of mammary stem cells for analysis of gene function during development and cancer. *Cell Stem Cell*, 2(1):90–102.

West, C., Joseph, L., and Bhana, S. (2008). Epidermal growth factor receptor-targeted therapy. *The British Journal of Radiology*, 81:S36–S44.

Wicha, M. S., Liu, S., and Dontu, G. (2006). Cancer stem cells: an old idea - a paradigm shift. *Cancer Research*, 66(4):1883–1890.

Yang, J., Liao, D., Chen, C., Liu, Y., Chuang, T.-H., Xiang, R., Markowitz, D., Reisfeld, R. A., and Luo, Y. (2013). Tumor-Associated Macrophages Regulate Murine Breast Cancer Stem Cells Through a Novel Paracrine EGFR/Stat3/Sox-2 Signaling Pathway. *Stem Cells*, 31(2):248–258.

Yang, M.-H. and Wu, K.-J. (2008). TWIST activation by hypoxia inducible factor-1 (HIF-1). *Cell Cycle*, 7(14):2090–2096.

Yang, N. (2015). An overview of viral and nonviral delivery systems for microRNA. *International Journal of Pharmaceutical Investigation*, 5(4):179.

Zhou, C., Li, G., Zhou, J., Han, N., Liu, Z., and Yin, J. (2014). miR-107 activates ATR/Chk1 pathway and suppress cervical cancer invasion by targeting MCL1. *PloS one*, 9(11):e111860.

Zhou, S., Schuetz, J. D., Bunting, K. D., Colapietro, A.-M., Sampath, J., Morris, J. J., Lagutina, I., Grosveld, G. C., Osawa, M., Nakauchi, H., et al. (2001). The ABC transporter Bcrp1/ABCG2 is expressed in a wide variety of stem cells and is a molecular determinant of the side-population phenotype. *Nature Medicine*, 7(9):1028–1034.

Zuker, M. (2003). Mfold web server for nucleic acid folding and hybridization prediction. *Nucleic Acids Research*, 31(13):3406–3415.

APPENDIX A

Solutions

A.1 Cell culture

A.1.1 Phosphate buffered saline

Dissolve 1 Sigma-Aldrich PBS tablet in 200ml dH_2O and autoclave.

Storage: at 4°C for one month.

A.1.2 CD133 $^-$ CCM

5ml FBS (Sigma-Aldrich)

45ml DMEM F-12 (3:1) (Lonza)

100 µl Ampicillin (Sigma-Aldrich)

A.1.3 CD133$^+$ Stempro CCM

45ml Stempro medium (Thermo Fisher Scientific)

100 µl Ampicillin (Sigma-Aldrich)

A.2 CD133$^+$ cell isolation and characterisation

A.2.1 0.5% BSA PBS

0.250g BSA (Sigma Aldrich)

Fill up to 50ml with PBS and filter sterilise

Storage: RT, use within 12 hours.

A.2.2 HBSS+

0.2ml FBS (Sigma Aldrich)

10mM HEPES (Sigma Aldrich)

Fill up to 10ml with PBS

Storage: 4°C for up to a month

A.3 Lentivirus synthesis and NSCLC transduction

A.3.1 Transformation buffer

15ml 100% glycerol (Sigma Aldrich)

1.47g $CaCl_2.2H_2O$ (Sigma Aldrich)

3.02mg PIPES.HCl

Adjust pH to 7 with NaOH

Make up to 100ml with dH_2O

Storage: autoclave and store at -20°C

A.3.2 1000× Ampicillin stock

5g Ampicillin (Sigma Aldrich)

25 ml 100% ethanol

25 ml dH_2O

Dissolve the Ampicillin in the ethanol and then add the dH_2O.

Final concentration: $100\,\mathrm{mg\,ml^{-1}}$

Storage: at -20°C for up to 6 months

A.3.3 Ampicillin agar broth

5g NaCl (Merck)

5g Tryptone (Sigma Aldrich)

2.5g Yeast extract (Sigma Aldrich)

Make up to 500ml with dH_2O

Autoclave for 30 minutes and add 500 µl of a 1000X Ampicillin stock (Appendix A.3.2) when mixture has cooled to 55°C

Storage: store at 4° for 1 month

A.3.4 0.5M EDTA pH 8.0

93.05g Na2.EDTA (Merck)

10.14g NaOH

500ml H_2O

Storage: RT for a number of years

A.3.5 TAE buffer

242g Tris-base (Sigma Aldrich)

57.1g Acetate (Sigma Aldrich)

100 ml 0.5M EDTA (Appendix A.3.4)

Make up to 1 l with dH_2O

A.3.6 1% TAE agarose gel

1g agarose (Sigma Aldrich)

100ml 1× TAE buffer (Appendix A.3.5)

5 µl Ethidium Bromide (Thermo Fisher Scientific)

Add the agarose to the 100ml TAE buffer. Microwave for 3 minutes, swirling the solution at 30 second intervals. Once cooled to 55°C, add the Ethidium Bromide, swirl the solution and then pour into a casting tray and leave to set.

Safety: Ethidium Bromide is a known carcinogen and should be handled with care. Gloves should be worn and aliquoting should be done under a fume hood.

A.4 miR-7 EGFR knockdown efficiency

A.4.1 3% formaldehyde PBS solution

1.5ml formaldehyde (Merck)

48.5ml autoclaved PBS prewarmed to 37°C

Use within 12 hours of preparation

A.4.2 RIPA buffer

25ml 100mM Tris-HCl (pH 7.4) (Sigma Aldrich)

0.87g NaCl (Merck)

1ml NP-40 (Bio-rad)

1g Sodium deoxycholate (Sigma Aldrich)

Make up to 100ml with dH_2O

Storage: filter sterilise and store at 4°C

A.4.3 20% Ammonium persulfate (AP)

0.1g AP

Make up to 500 µl in dH_2O

A.4.4 40% Acrylamide/Bis

38.68g Acrylamide (Bio-rad)

1.32g Bis-Acrylamide (Bio-rad)

Make up to 100 ml in dH_2O

Store in foil at 4°C

A.4.5 8% Resolving gel

2.4ml 40% Acrylamide (Bio-rad)

1.5ml 8× Resolving buffer

8.1ml dH_2O

60 µl 20% SDS (Bio-rad)

6 µl TEMED (Thermo Fisher Scientific)

30 µl 20% AP (made fresh) (Merck)

A.4.6 8× Resolving buffer

36.3g Tris-base (Sigma Aldrich)

Make up to 100 ml with dH_2O

Adjust pH to 8.8 with HCl

Store at 4°C for up to 6 months

A.4.7 Stacking gel

1ml 40% Acrylamide (Bio-rad)

2ml 4× Stacking buffer

5ml dH_2O

60 µl 20% SDS (Bio-rad)

8.3 µl TEMED (Thermo Fisher Scientific)

21.6 µl 20% AP (made fresh) (Merck)

A.4.8 4× Stacking buffer

6.05g Tris-base (Sigma Aldrich)

Make up to 100 ml with dH_2O

Adjust pH to 8.8 with HCl

Store at 4°C for up to 6 months

A.4.9 1× Tank buffer

3.03g Tris-base (Sigma Aldrich)

14.4g Glycine (Sigma Aldrich)

1g SDS (Bio-rad)

Make up to 1 l with dH_2O

Store at RT

A.4.10 1× Transfer buffer

12.12g Tris-base (Sigma Aldrich)

57.6g Glycine (Sigma Aldrich)

400ml Methanol (Sigma Aldrich)

Make up to 2 l with dH_2O

Store at 4°C

A.4.11 Blocking buffer

5g skim milk powder (Elite)

Make up to 50 ml in 0.05% Tween-20 solution (Wash buffer)

Make fresh

A.4.12 Wash buffer

250 µl Tween-20 (Thermo Fisher Scientific)

Make up to 500 ml with PBS

Store at RT

APPENDIX B

Protocols

B.1 Lentivirus synthesis and NSCLC transduction

B.1.1 Competent bacteria

1. Thaw transformation buffer on ice
2. Inoculate 8ml of LB broth with an aliquot of *E. coli* DH5-α and grow overnight at 37°C at 200 RPM
3. Transfer 8ml of culture into 42ml fresh LB. Incubate for 2-3 hours at 37°C at 200rpm until OD_{600} 0.3-0.5 indicative of exponential growth phase
4. Culture should be placed on ice once exponential growth phase is reached
5. Centrifugation of culture at at 1500 RPM for 15 minutes. Pour off supernatant
6. Gently resuspend pellet in 1ml of ice cold transformation buffer (A.3.1). Add another 3ml to the suspension
7. Gently place the cells on ice for 30 minutes
8. Centrifugation of cells at 1500 RPM at 4°C. Pour off supernatant
9. Gently resuspend pellet in 1ml of transformation buffer
10. Aliquot 100 µl of suspension into 1.5ml Eppendorf tubes and store at -4°C

B.1.2 Ampicillin agar bacterial plates

1. Add the following to an Erlenmeyer flask:

   5g NaCl

   5g Tryptone

   2.5g Yeast extract

   7.5g Agar

2. Make up to 500ml with dH_2O
3. Autoclave for 30 minutes
4. Add 500 µl of a 1000× Ampicillin stock when mixture has cooled to 55°C
5. Pour agar plates at a sterile bench and store at 4°C until use

B.1.3 Ligation

1. Calculate the insert mass needed with the following formula using a 30 ng vector mass:

$$\text{Insert mass} = 6 \times \frac{\text{Insert length (bp)}}{\text{Vector length (bp)}} \times \text{Vector mass} \tag{B.1}$$

2. Add dH_2O into a sterile 1.5 µl Eppendorf tube for a final volume of 20 µl by subtracting the calculated vector and insert volume
3. Add 2 µl 10× ligation buffer
4. Add volume of insert to allow for mass calculated in Equation B.1 above
5. Add 30 ng vector
6. Add 1 µl DNA ligase
7. Incubate the ligation mixture at 22.5°C for 1 hour or overnight
8. Use 2 µl of reaction to transform electrocompetent bacteria

Note: Always perform a control ligation reaction with the same mass of the vector and dH_2O in place of the insert

APPENDIX C

Supplementary data

C.1 Lentivirus synthesis and NSCLC transduction

C.1.1 Molecular cloning

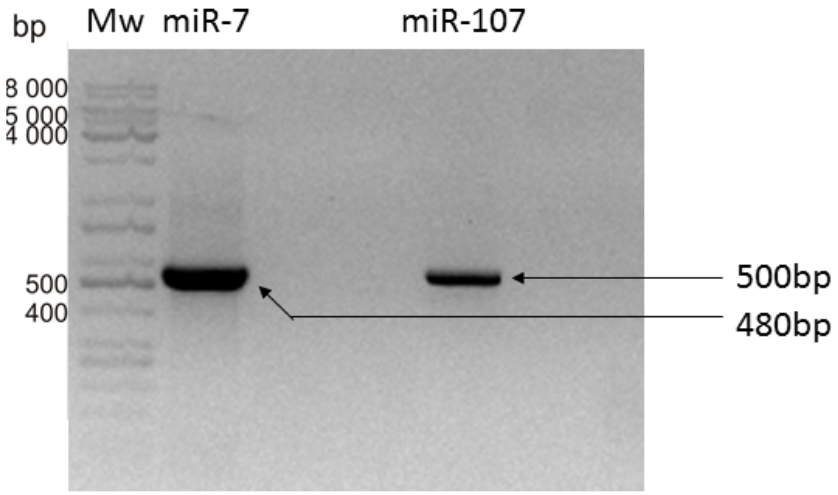


Figure C.1: Gel electrophoresis to confirm successful PCR amplification of hsa-pri-miR-7 and hsa-pri-miR-107 from the A549 genome. hsa-pri-miR-7 and hsa-pri-miR-107 products with flanking BsmBI restriction sites are 480bp and 500bp, respectively

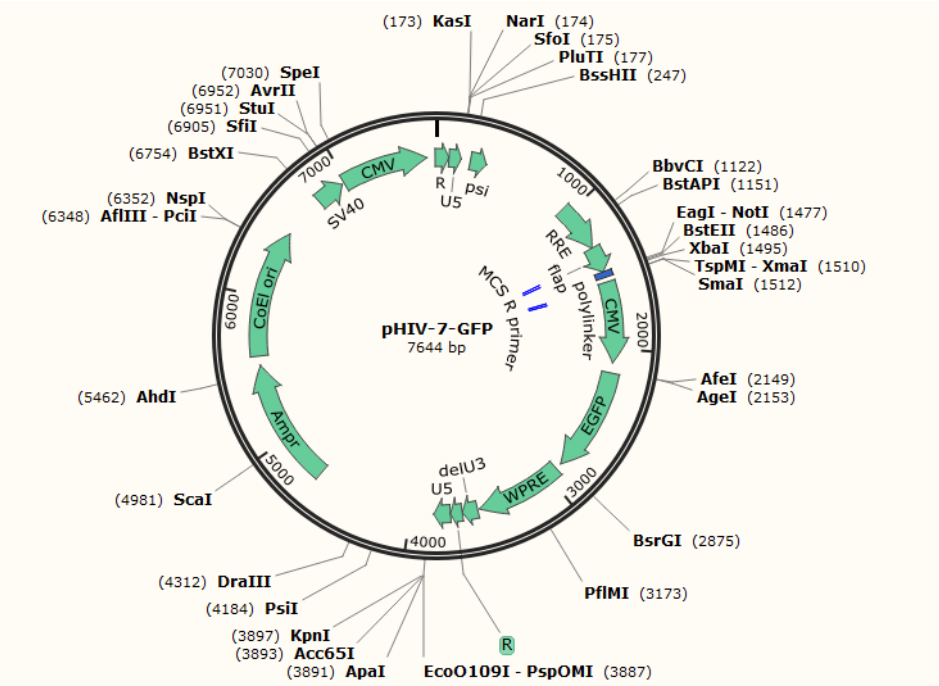


Figure C.2: pHIV-7-GFP vector map

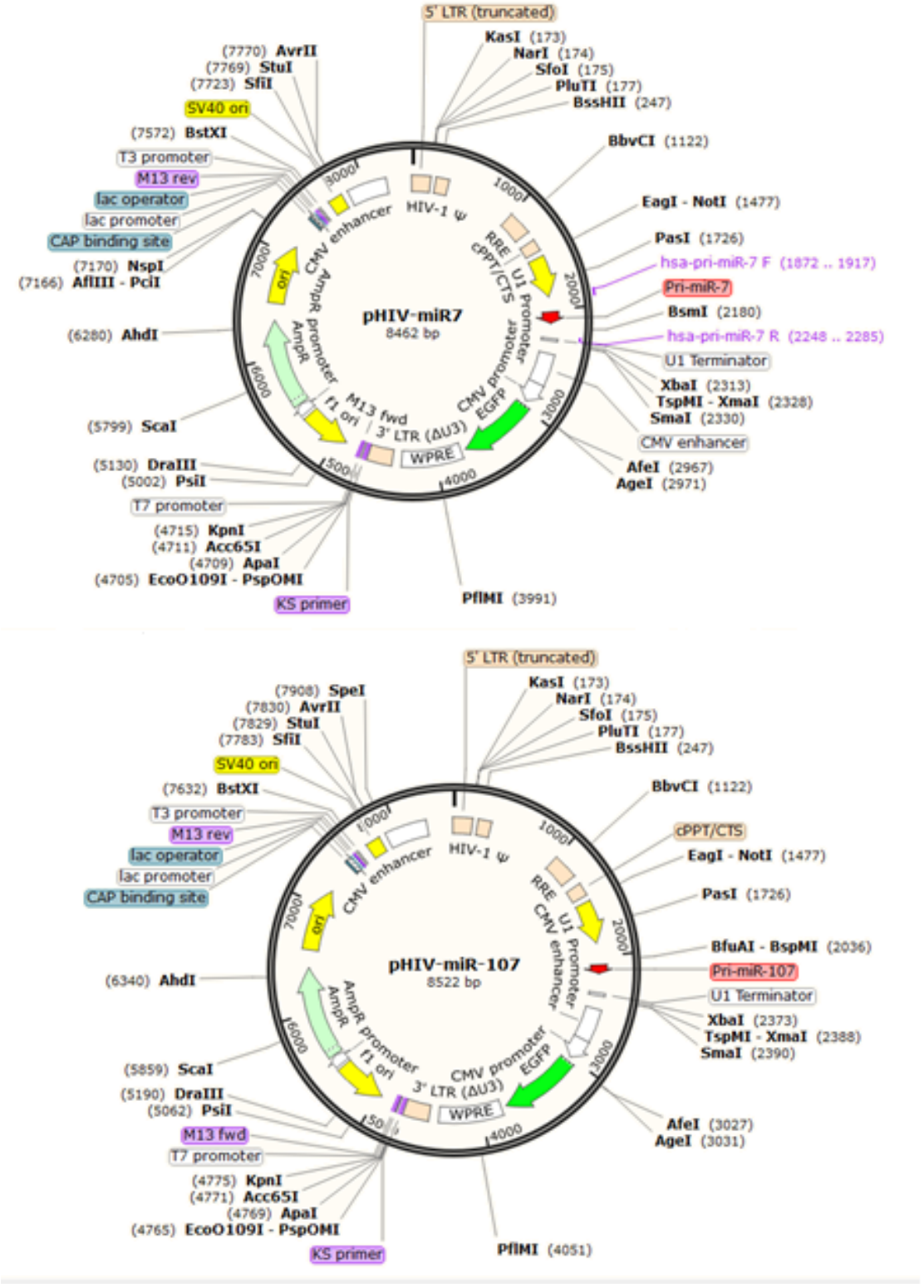


Figure C.3: Vector maps of pHIV-7-pri-miR-7 (top) and pHIV-7-pri-miR-107 control (bottom). Vector maps were constructed on SnapGene, based on the pHIV-7 sequence kindly donated by Marc Weinberg.

C.1.2 Sequencing results

C.1.3 hsa-pri-miR-7 sequence and the U1 promoter

hsa-miR-7 sequence with polIII termination sequence in bold:

5'-UUGGAUGUUGGCCUAGUUCUGUGUGGAAGACUAGUGA**UUUU**GUUGUUUUUA
GAUAACUAAAUCGACAACAAAUCACAGUCUGCCAUAUGGCACAGGCCAUGCCU
CUACAG-3'

Sequence sourced from Landgraf et al. (2007)